STUDIES OF MAGNETISM USING NUCLEAR ORIENTATION AND RELATED NMR TECHNIQUES

By

James Pond

DEUG, Licence, Maîtrise, DEA, Université de Paris XI, Orsay, 1991-1996

Magistère Interuniversitaire de Physique, Ecole Normale Supérieure, 1996

A THESIS SUBMITTED IN PARTIAL FULFILLMENT OF

THE REQUIREMENTS FOR THE DEGREE OF

DOCTOR OF PHILOSOPHY

in

THE FACULTY OF GRADUATE STUDIES

DEPARTMENT OF PHYSICS AND ASTRONOMY

We accept this thesis as conforming

to the required standard

THE UNIVERSITY OF BRITISH COLUMBIA

2000

In presenting this thesis in partial fulfilment of the requirements for an advanced degree at the University of British Columbia, I agree that the Library shall make it freely available for reference and study. I further agree that permission for extensive copying of this thesis for scholarly purposes may be granted by the head of my department or by his or her representatives. It is understood that copying or publication of this thesis for financial gain shall not be allowed without my written permission.

Department of Physics and Astronomy
The University of British Columbia
6224 Agricultural Road
Vancouver, B.C., Canada
V6T 1Z1

Date: Dec. 5 / 2000

Abstract

Nuclear Orientation and related NMR techniques have been used to study three magnetic insulators: $Mn(COOCH_3)_2 \cdot 4H_2O$, $MnCl_2 \cdot 4H_2O$ and $CoCl_2 \cdot 6H_2O$.

Continuous wave NMR thermally detected by Nuclear Orientation has been used to investigate the magnetic properties and spin dynamics of the quasi-2-dimensional ferromagnet ^{54}Mn-$Mn(COOCH_3)_2 \cdot 4H_2O$. The system exhibits a frequency pulling effect due to the indirect Suhl-Nakamura interaction between nuclear spins and the electronic spin excitation spectrum is related to the coupling strength of the nuclear spins. The temperature dependence of the frequency pulling effect was measured for the two crystalline sublattices Mn1 and Mn2 in low magnetic field. The spectra show a structure not predicted theoretically. The current theory is valid only for $I = 1/2$ with uniaxial crystalline anisotropy fields. The theory of frequency pulling has been extended here to the case of $I \geq 1/2$ and non-uniaxial crystalline anisotropy fields and the resonant frequencies and linewidths have been calculated as a function of temperature. The new theory and data agree well in terms of the magnitude and temperature dependence of the frequency pulling. Discrepancies are likely due to simplifying assumptions when calculating the electronic magnon spectrum. Classical and quantum numerical simulations confirm qualitatively the predictions of the model.

The first Low Temperature Nuclear Orientation experiments on isotopes implanted into insulators is reported. Radioactive ^{56}Mn ions have been implanted into insulating, antiferromagnetic crystals of $MnCl_2 \cdot 4H_2O$ and $CoCl_2 \cdot 6H_2O$. In $MnCl_2 \cdot 4H_2O$, comparison of the γ-ray anisotropy of the ^{56}Mn nuclei with that of ^{54}Mn, doped into the sample during growth, showed that both the ^{56}Mn and ^{54}Mn spins felt a very similar hyperfine field.

The site occupancy factor in a simple, two site model was deduced to be $0.96^{+0.04}_{-0.07}$. In $CoCl_2 \cdot 6H_2O$, the average hyperfine field for the implanted ^{56}Mn was significantly less than that for ^{54}Mn and corresponded to $f = 0.53 \pm 0.10$.

Radioactive and stable Co impurities, doped into $MnCl_2 \cdot 4H_2O$ during growth, have been studied by Nuclear Orientation and NMR. The hyperfine fields of ^{57}Co and ^{60}Co, measured by Nuclear Orientation, were found to be significantly different. The NMR resonance of the Co impurities was not found, probably because the spin-lattice relaxation time is too short for the resonance to be observed with the radiofrequency modulation used. The effects of 3.96% stable Co on the host Mn spins were studied by NMR. The presence of the impurities broadens the NMR resonance and reduces the spin-lattice relaxation time by an order of magnitude.

New aspects of the design of radiofrequency coils for use in continuous wave NMRON are reported, and the important effects of transmission lines are presented.

Table of Contents

List of Tables

List of Figures

Acknowledgements

I'd like to thank Brian Turrell for his excellent supervision throughout the thesis. He was always available to discuss problems which arose, but allowed me to work independently. He also understands that there is more to life than physics! I'd like to thank Andrzej Kotlicki for his help and supervision, particularly at the start of my thesis. Both Brian and Andrzej have become good friends.

I'd like to thank my PhD committee for all their help with various problems, not only in physics. Of course, I'd like to thank all the technicians, particularly Doug Wong for helping me to clean so many pumps and cold traps! I'd also like to thank all the other students who worked with me at various times throughout my thesis. It was also very helpful to work with Girgl Eska, from whom I learned a great deal in a short time.

I'd like to thank my family for all their support, particularly my sister, Ellen, who has helped me tremendously throughout my thesis. I'd like to thank all my friends for putting up with me, particularly Michelle, Drew, Adam, Jane, Kaspar, Anna, Jenn, Nicolas and Nicola. Finally, I'd like to thank Martin who inspired me to do this thesis in the first place, and Gabriela who gave me the support and motivation to finish it.

The financial support of NSERC and UBC is gratefully acknowledged.

Chapter 1

Introduction

Nuclear spins can be oriented at sufficiently low temperatures when acted on by a magnetic field or electric field gradient. For orientation by a magnetic field the spin must satisfy $I \geq 1/2$, whereas for orientation by an electric field gradient $I \geq 1$. Low Temperature Nuclear Orientation (NO) involves measuring the resulting degree of order in the nuclear spin system. At $T = \infty$, the nuclear moments are completely disordered, whereas at $T = 0$ the moments are fully oriented. At finite temperature, the degree of alignment depends on the temperature of the ensemble, the intensity of the magnetic field or electric field gradient, the spin of the nucleus and its appropriate moment.

The nuclear orientation can be measured through the decay products of radioactive nuclei. An ensemble of radioactive nuclei can emit radiation anisotropically and the probability of emission in a given direction depends on the direction of the spins of the initial nuclei. Therefore, if an ensemble of spins is, on average, oriented in a given direction the radiation field can be anisotropic. The intensity of radiation can be measured in one or more directions and compared to the high temperature value to determine the directional anisotropy of the radiation. We can define $N(\theta, T)$ to be the number of counts, or intensity, of the decay products (γ, β or α particles) measured at an angle θ to the applied field at a temperature T. The angular distribution of decay products is defined as:

$$W(\theta) = \frac{N(\theta, T)}{N(\theta, T = \infty)} \tag{1.1}$$

$W(\theta)$ can be measured and used to study many properties of the nuclear ensemble

and its electronic environment which produces the hyperfine interaction acting on the nuclei.

NO can be combined with Nuclear Magnetic Resonance (NMR) by applying a magnetic field oscillating at the resonant frequency of the nuclei in the ordering field. In pulsed NMR, a strong oscillating field is applied for a fixed time so that the magnetization precesses through a determined angle (usually 90° or 180°). In continuous wave (CW) NMR, a small oscillating field is applied continuously to perturb the nuclear magnetization. After the nuclear spin ensemble has been perturbed, its relaxation back to the thermal equilibrium is characterized by the time T_1 which provides information on how the nuclei are dynamically coupled to their environment (the lattice). This dynamic coupling between the nuclei and the lattice is called the spin-lattice interaction. The advantage of combining the methods is that NMR of Oriented Nuclei (NMRON) is many orders of magnitude more sensitive than conventional NMR. It is therefore possible to study a very small number of nuclei, for example in very small or very dilute systems.

It is also possible to use radioactive nuclei embedded in a host lattice as a temperature probe. At the temperatures of interest for NO (1-500 mK), the magnetic moments of the abundant, stable nuclei generally account for most of the specific heat of a magnetic crystal. If NMR is performed on the stable nuclei in a crystal, the effect of the absorbed power is to increase the temperature of the lattice via the spin-lattice interaction. This increase in temperature can be measured by the NO of the dilute radioisotope in the crystal. The technique is called NMR Thermally Detected by NO (NMR-TDNO) [1].

A more quantitative description of NO and its NMR related techniques is given in Chapter 2. The NO parameters are calculated for the radioactive isotopes used in the experiments reported in subsequent chapters. NMR is discussed in the classical and quantum cases. Spin-lattice relaxation is considered in the case of very dilute spins, as is often the case in NO. Finally, the enhancement effect, whereby the amplitude of the

oscillating magnetic field is magnified, is discussed.

In Chapter 3, the details of radiofrequency (RF) coil design are discussed. A very general technique of calculating the RF field produced by a given coil, circuit and transmission lines is developed and applied to two coil designs developed for the NMR experiments presented here. One of these circuits is currently installed at TRIUMF in the LTNO dilution refrigerator.

In Chapter 4, an experiment combining NMRON and NMR-TDNO on a quasi-2-dimensional system, manganese acetate tetrahydrate ($Mn(COOCH_3)_2{\cdot}4H_2O$ or MnAc) is described. The "frequency pulling" of the NMR resonance is measured as a function of temperature. The theoretical predictions previously developed [2, 3, 4] apply only to the case of $I = 1/2$ in a crystal with uniaxial anisotropy fields and are clearly insufficient to describe the MnAc crystal where $I = 5/2$ and there are non-uniaxial anisotropy fields. Furthermore, MnAc has a triplet of spins at each lattice position.

A new theoretical model is developed in Chapter 5 for the general case of $I \geq 1/2$ with anisotropy fields and a basis of spins. The results of the model are compared to the MnAc experiment, and found to agree well in terms of the magnitude and temperature dependence of the frequency pulling. The strength of the frequency pulling is found to depend strongly on the anisotropy fields. The failure of the model to describe the splitting of one of the resonant lines in MnAc, and the absorption of another, is most probably due to simplifying assumptions when calculating the electronic magnon spectrum.

The results of the first NO measurements of implanted ions into insulators is described in Chapter 6. ^{56}Mn was implanted into $MnCl_2{\cdot}4H_2O$ doped with ^{54}Mn, and $CoCl_2{\cdot}6H_2O$ doped with ^{54}Mn and ^{60}Co. The NO results of the implanted ^{56}Mn are compared with the doped ^{54}Mn to determine the implantation fraction. It is found that the implantation fraction is consistent with unity when the ^{56}Mn is implanted into $MnCl_2{\cdot}4H_2O$ but not when it is implanted into $CoCl_2{\cdot}6H_2O$.

The implantation results lead to questions about the lattice positions and the effects of impurities in magnetic insulators. Chapter 7 describes a series of NO and NMRON experiments to investigate the effects of impurities in an insulating system. ^{57}Co, ^{59}Co, ^{60}Co and ^{54}Mn were doped into crystals of $MnCl_2 \cdot 4H_2O$. Surprisingly, the NO results indicate different hyperfine fields for ^{57}Co and ^{60}Co. The NMR resonance for Co was not found, probably because the spin-lattice relaxation time is too short. The presence of $\sim 4\%$ stable ^{59}Co is found to broaden the NMR resonance of the ^{54}Mn significantly, and reduce the spin-lattice relaxation time by an order of magnitude.

1.1 Note on units

All the formulae in this thesis are written in units where $\hbar = 1$. When reporting numerical values, $\hbar$ or h is reintroduced in SI units.

Chapter 2

General introduction to NO and its NMR related techniques

2.1 The NO parameters

If a magnetic field of amplitude B_0 is applied to a nucleus of spin I the degeneracy of the $2I+1$ magnetic substates is lifted, and the energy of the mth substate is

$$E_m = -\gamma_N B_0 m \tag{2.2}$$

where γ_N is the gyromagnetic ratio. If the degeneracy of the magnetic substates is lifted by an electric field gradient, for example in the uniaxial case where $\frac{\partial^2 V}{\partial z^2} = eq$, then

$$E_m = \frac{2e^2Qq}{4I(2I-1)}\left(m^2 - \frac{1}{3}I(I+1)\right) \tag{2.3}$$

where Q is the quadrupole moment of the nucleus [5]. If an ensemble of nuclei is in thermal equilibrium with the lattice at temperature T, then the population of the mth nuclear sublevel is given by the Boltzmann factor

$$p_m = \frac{1}{Z}\exp\left(-\frac{E_m}{k_B T}\right) \tag{2.4}$$

where k_B is the Boltzmann constant and Z is the partition function.

In order to achieve significant differences in the level populations, it is necessary to achieve temperatures such that $k_B T \sim E_m - E_{m+1}$, or $B/T \sim 10^4 T/K$ in the case of a magnetic interaction. Fortunately, the hyperfine interaction (HFI) can provide magnetic fields of tens or hundreds of teslas, though it is still necessary to achieve temperatures of 1-100 mK. This temperature range can be reached with a dilution refrigerator.

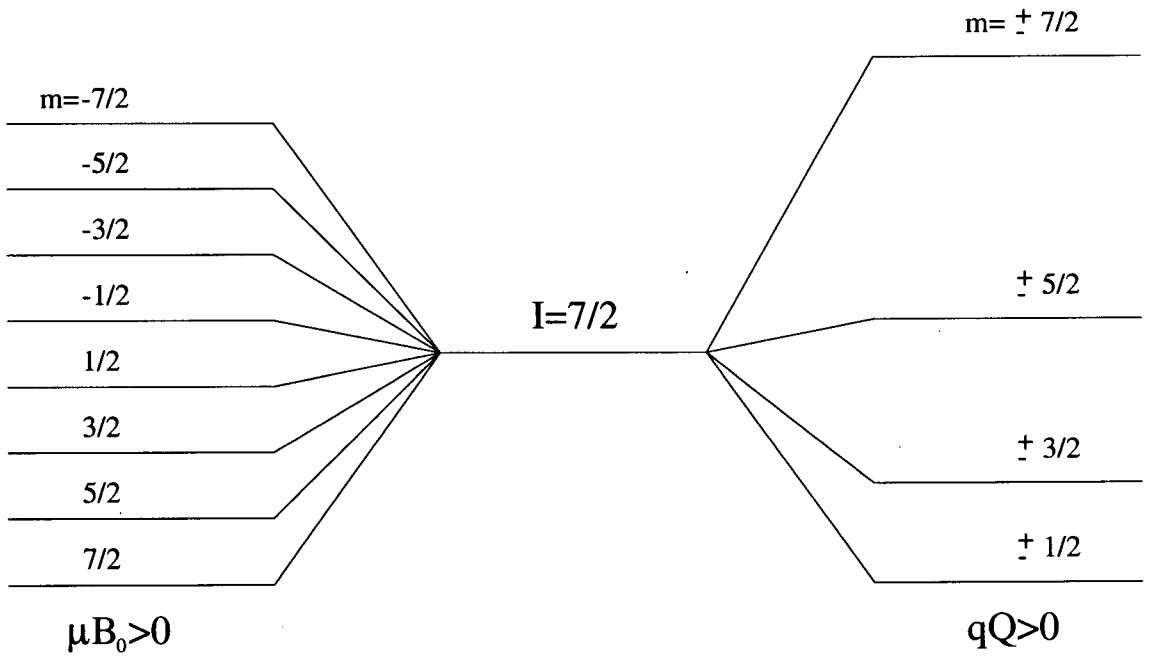

Figure 2.1: The level splittings of an $I = 7/2$ nuclear level for the case of a pure magnetic interaction (left) and a pure electric interaction (right). In the general case, both interactions are present.

When sufficient differences in the level populations are achieved, the directional distribution of emitted radiation is measured. In a typical experiment, the initial nuclear ensemble of spin I_0 decays to a state of spin I_i through one or more unobserved transitions. Finally, it decays to a final state of spin I_f while emitting the observed radiation.

The normalized γ-ray intensity observed at angle θ to the magnetization axis at temperature T, in an axially symmetric state, can be expressed as [5]

$$W(\theta) = \sum_k B_k U_k A_k Q_k P_k(cos\theta) \tag{2.5}$$

The B_k are the nuclear orientation parameters and describe the orientation of the initial state of spin I_0. They are given by

$$B_k(I_0) = \hat{k}\hat{I}_0 \sum_m (-1)^{I_0+m} \begin{pmatrix} I_0 & I_0 & k \\ -m & m & 0 \end{pmatrix} p_m \tag{2.6}$$

where $\begin{pmatrix} I_0 & I_0 & k \\ -m & m & 0 \end{pmatrix}$ is a Wigner 3-j symbol and $\hat{x} = \sqrt{2x+1}$.

The U_k are deorientation coefficients which take into account the transitions $(I_0 \rightarrow I_i)$ preceding the observed radiation. For a pure transition of multipole order L, between states I_1 and I_2, the U_k are given by

$$U_k(I_1 I_2 L) = (-1)^{I_1+I_2+L+k} \hat{I}_1 \hat{I}_2 \begin{Bmatrix} I_1 & I_1 & k \\ I_2 & I_2 & L \end{Bmatrix} \tag{2.7}$$

where $\begin{Bmatrix} I_1 & I_1 & k \\ I_2 & I_2 & L \end{Bmatrix}$ is a Wigner 6-j symbol.

If the path from I_0 to I_i consists of many transitions $(I_0 I_1 I_2 ... I_n I_i)$, then the deorientation coefficients are given by

$$U_k(I_0 I_i) = U_k(I_0 I_1) U_k(I_1 I_2) ... U_k(I_n I_i) \tag{2.8}$$

If there are many branches connecting the states I_0 and I_f then the deorientation coefficient is given by a weighted average of the possible branches. Finally, if the unobserved radiation contains several multipolarities, the deorientation coefficients are weighted by the intensity of each multipole component.

$$U_k(I_1 I_2) = \sum_L U_k(I_1 I_2 L)| < I_2|L|I_1 > |^2 / \sum_L | < I_2|L|I_1 > |^2 \tag{2.9}$$

The A_k are the directional distribution coefficients for the observed radiation and, in the case of a pure decay of multipole order L,

$$A_k(I_f I_i) = F_k(LLI_f I_i) \tag{2.10}$$

where the F-coefficient is given by

$$F_k(LL'I_f I_i) = (-1)^{I_f+I_i+1}\hat{k}\hat{L}\hat{L}'\hat{I}_i \begin{pmatrix} L & L' & k \\ 1 & -1 & 0 \end{pmatrix} \begin{Bmatrix} L & L' & k \\ I_i & I_i & I_f \end{Bmatrix} \tag{2.11}$$

If two multipoles contribute, and the mixing ratio is δ, then

$$A_k(I_f I_i) = \frac{F_k(LLI_f I_i) + 2\delta F_k(LL'I_f I_i) + \delta^2 F_k(L'L'I_f I_i)}{1+\delta^2} \tag{2.12}$$

For γ radiation, $A_k = 0$ if k is odd because the processes involved do not violate parity.

The Q_k are corrections for the solid angle subtended by the detectors and the P_k are the Legendre polynomials.

2.2 NO parameters for the nuclei used

The decay scheme of ^{54}Mn and the simplified decay schemes of ^{56}Mn, ^{57}Co and ^{60}Co are given in figures 2.2-2.5 respectively [6].

The nuclear orientation parameters can be easily calculated, e.g. by Mathematica, and the U_2 and A_2 coefficients are listed in table 2.1 for each observed transition of the isotopes used in the following chapters.

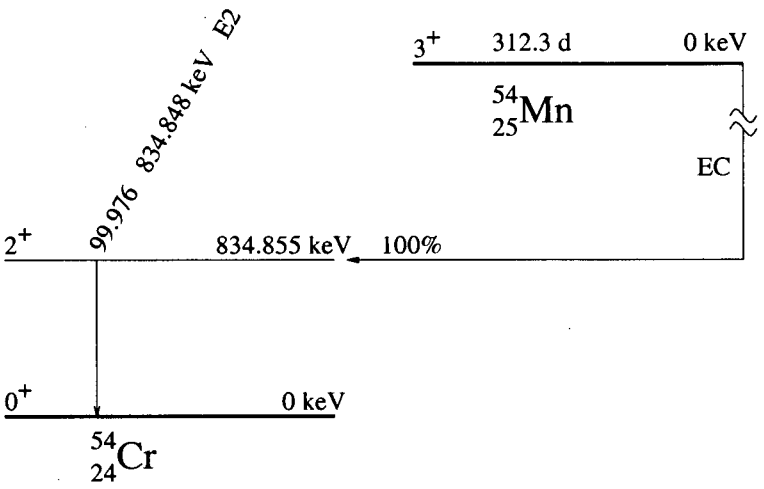

Figure 2.2: The decay scheme of ^{54}Mn. ^{54}Mn has a magnetic moment of $\mu = 3.2819 \pm 0.0013\mu_N$ and a quadrupole moment of $Q = +0.33 \pm 0.03$ b.

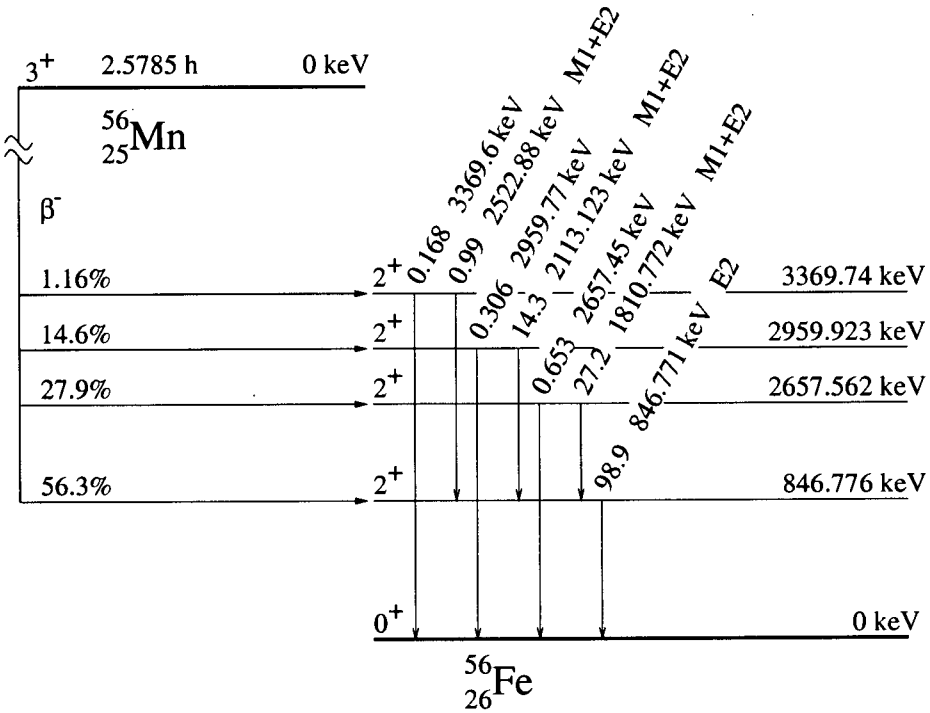

Figure 2.3: The simplified decay scheme of ^{56}Mn. The mixing ratios for the 2523 keV, 2113 keV and 1811 keV transitions are, respectively, $\delta = 0.25 \pm 0.15$, $\delta = 0.27 \pm 0.03$ and $\delta = -0.18 \pm 0.01$. ^{56}Mn has a magnetic moment of $\mu = 3.2266 \pm 0.0002\mu_N$.

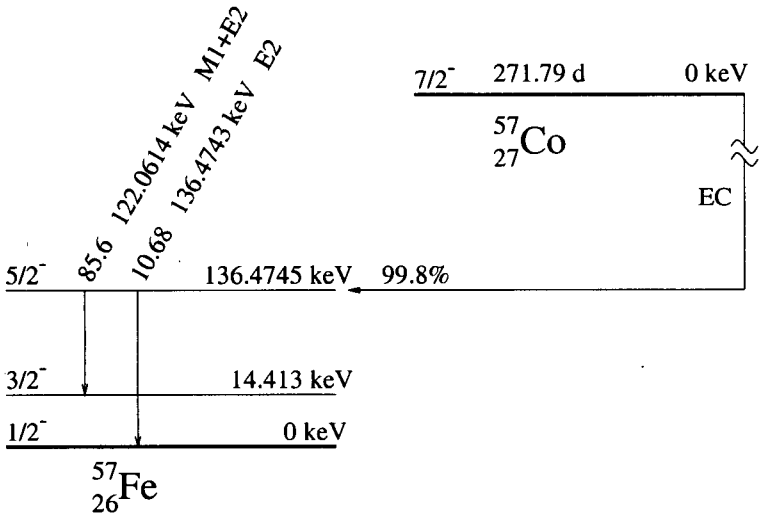

Figure 2.4: The simplified decay scheme of ^{57}Co. The mixing ratio for the 122 keV transition is $\delta = 0.120 \pm 0.001$. ^{57}Co has a magnetic moment of $\mu = 4.720 \pm 0.010 \mu_N$ and a quadrupole moment of $Q = +0.52 \pm 0.09$ b.

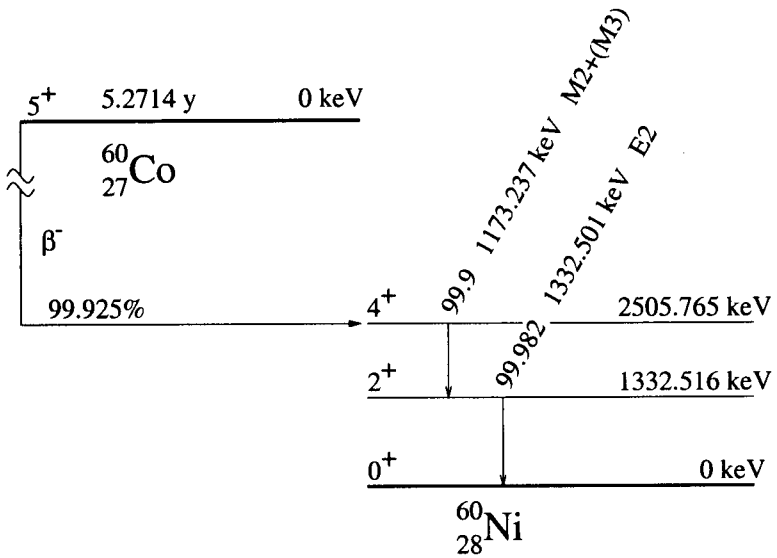

Figure 2.5: The simplified decay scheme of ^{60}Co. ^{60}Co has a magnetic moment of $\mu = 3.799 \pm 0.008 \mu_N$ and a quadrupole moment of $Q = +0.44 \pm 0.05$ b.

Isotope	γ energy (keV)	U_2	A_2	U_4	A_4
^{54}Mn	834.848	0.828079	-0.597614	0.417855	-1.06904
^{56}Mn	846.771	0.638722	-0.597614	0.125907	-1.06904
^{57}Co	122.061	0.874818	0.141692	0.580288	0.01001
	136.474	0.874818	-0.534522	0.580288	-0.61721
^{60}Co	1173.237	0.939374	-0.447702	0.797724	-0.30438
	1332.501	0.703732	-0.597614	0.227128	-1.06904

Table 2.1: The nuclear orientation coefficients U_k and A_k for various isotopes.

The angular distributions can also be expressed as functions of the level populations,

$$W(\theta) = \sum_m a_m(\theta) p_m \tag{2.13}$$

The a_m satisfy $\sum_m a_m(\theta) = 2I_0 + 1$, and, of course, $\sum_m p_m = 1$. This expression of the angular distribution is particularly useful for NMR when different level populations are equalized or inverted. The change in $W(\theta)$ can then be easily calculated.

2.3 Nuclear Magnetic Resonance (NMR)

We shall consider an isolated spin in a magnetic field or electric field gradient along the z-axis. A resonance occurs when there are transitions between an initial and final nuclear substate. The simplest way to induce transitions between magnetic substates is to apply an oscillating magnetic field perpendicular to the applied field, $\vec{B}_0$, or the electric field gradient. The oscillating field has a frequency $\nu = \omega/2\pi$. Energy conservation leads immediately to the resonance condition $\omega = E_f - E_i$.

The case of an applied, constant magnetic field, B_0, will be considered in some detail, although many of the results also apply to an electric field gradient.

The total magnetic field is given by

$$\vec{B} = B_0 \hat{u}_z + b(\cos \omega t \, \hat{u}_x + \sin \omega t \, \hat{u}_y) \tag{2.14}$$

Isotope	I_0	γ energy (keV)	m	$a_m(0°)$	$a_m(90°)$
^{54}Mn	3	834.848	±3	0	5/4
			±2	5/3	5/4
			±1	4/3	3/4
			0	1	1/2
^{56}Mn	3	846.771	±3	0.36296	1.24319
			±2	1.20088	1.07533
			±1	1.30187	0.82395
			0	1.26858	0.71505
^{57}Co	7/2	122.061	$\pm7/2$	1.19398	0.96142
			$\pm5/2$	1.01844	0.99636
			$\pm3/2$	0.91687	1.01654
			$\pm1/2$	0.87071	1.02569
		136.474	$\pm7/2$	0	5/4
			$\pm5/2$	10/7	5/4
			$\pm3/2$	10/7	25/28
			$\pm1/2$	8/7	17/28
^{60}Co	5	1173.237	±5	0	5/4
		and	±4	1	5/4
		1332.501	±3	4/3	13/12
			±2	4/3	7/8
			±1	26/21	5/7
			±0	25/21	55/84

Table 2.2: The $a_m(\theta)$ coefficients for various isotopes for $\theta = 0°, 90°$. Note that both γ decays of ^{60}Co have the same coefficients. Although the U_k and A_k coefficients are different, the product $U_k A_k$ is the same. For pure transitions, the results are exact and are given as fractions. When transitions of mixed multipolarities are involved, the accuracy of the values are limited by the knowledge of the mixing ratio, δ. All terms are calculated assuming that $Q_k = 1$.

If we have an ensemble of spins, with N_i spins in the initial state and N_f in the final state, then

$$\frac{dN_i}{dt} = N_f Q_{fi} - N_i Q_{if} \tag{2.15}$$

where Q_{if} is the transition rate between initial and final states induced by the oscillating magnetic field. The transition rate increases when the magnitude of the oscillating field is increased.

In the case that $Q_{if} = Q_{fi} = Q$ and taking $n = N_i - N_f$ then

$$\frac{dn}{dt} = -2Qn \tag{2.16}$$

and

$$n = n(0)\exp(-2Qt) \tag{2.17}$$

The effect of the transitions is to equalize the spin populations in a time on the order of $1/Q$. Of course, the initial level populations are given by the Boltzmann factor, and relax with a characteristic time T_1, due to spin-lattice relaxation processes. For a spin 1/2 system

$$n = n_0 + A\exp\left(-\frac{t}{T_1}\right) \tag{2.18}$$

where n_0 is the thermal population difference.

The overall rate equation due to resonance and thermal relaxation is

$$\frac{dn}{dt} = -2Qn + \frac{n_0 - n}{T_1} \tag{2.19}$$

In a steady state,

$$n = \frac{n_0}{1 + 2QT_1} \tag{2.20}$$

If $T_1 \ll 1/Q$ then $n \simeq n_0$, but if $T_1 \gg 1/Q$ then $n \to 0$ and the level populations become approximately equal. Therefore, when performing NMRON, systems with long T_1 are desirable (and this is generally the case because the temperature is very low)

because it is easier to equalize the level populations and destroy the γ-ray anisotropy. However, if T_1 is too long, the initial cooling of the nuclear spins is rendered difficult.

The absorbed power is simply

$$P = n(E_f - E_i)Q = n_0(E_f - E_i)\frac{Q}{1 + 2QT_1} \tag{2.21}$$

The maximum absorbed power with respect to Q (when the oscillating magnetic field becomes large) is $n_0(E_f - E_i)/2T_1$. For NMR-TDNO, it should be noted that when $Q \gg 1/T_1$ the system is saturated and the transition rate due to NMR cannot be increased, even if the amplitude of the oscillating magnetic field is increased. Therefore, for this technique to be useful, systems with short T_1 are desirable because the resonance is being used to warm the lattice.

2.3.1 Classical treatment

The rate of change of the angular momentum, $\vec{I}$, is given by the torque

$$\frac{d\vec{I}}{dt} = \vec{\mu} \times \vec{B} \tag{2.22}$$

where $\vec{B}$ is the sum of the static an oscillating magnetic fields, as defined in equation 2.14 and since the magnetic moment is $\vec{\mu} = \gamma_N \vec{I}$, we have

$$\frac{d\vec{\mu}}{dt} = \vec{\mu} \times (\gamma_N \vec{B}) \tag{2.23}$$

We can change coordinates from the fixed reference frame (fix), of unit vectors $\hat{u}_z$, $\hat{u}_x$ and $\hat{u}_y$, to the reference frame rotating at angular velocity $\vec{\omega} = \omega \hat{u}_z$ (rot), of unit vectors $\hat{e}_z = \hat{u}_z$, $\hat{e}_x = \cos\omega t\, \hat{u}_x + \sin\omega t\, \hat{u}_y$, $\hat{e}_y = \cos\omega t\, \hat{u}_y - \sin\omega t\, \hat{u}_x$. Since the time derivative in the rotating reference frame is given by

$$\left.\frac{d}{dt}\right)_{rot} = \left.\frac{d}{dt}\right)_{fix} - \vec{\omega}\times \tag{2.24}$$

then

$$\left.\frac{d\vec{\mu}}{dt}\right)_{rot} = \vec{\mu} \times (\gamma_N \vec{B} + \vec{\omega}) = \gamma_N \vec{\mu} \times \vec{B}_{eff} \tag{2.25}$$

where $\vec{B}_{eff} = (B_0 + \omega/\gamma_N)\hat{u}_z + b\hat{e}_x$. If we choose $\vec{\omega} = -\gamma_N \vec{B}_0$ then

$$\left.\frac{d\vec{\mu}}{dt}\right)_{rot} = \vec{\mu} \times (b\hat{e}_x) \tag{2.26}$$

The solution for the z component of the magnetic moment is $\mu_z = \mu \cos(\gamma_N b t)$.

Therefore, in the rotating reference frame, the magnetic moment precesses in the y-z plane when the resonance condition $\vec{\omega} = -\gamma_N \vec{B}_0$ is achieved. The z-component of the magnetic moment oscillates between $\pm\mu$ with frequency $\gamma_N b/2\pi$.

2.3.2 Quantum mechanical treatment

The Hamiltonian for the system is

$$H = -\Omega_0 I^z + -\frac{\gamma_N}{2}(I^+ b^-(t) + I^- b^+(t)) \tag{2.27}$$

where $I^\pm = I^x \pm iI^y$, $b^\pm(t) = b_x(t) \pm ib_y(t) = b\exp(\pm i\omega t)$ and $\Omega_0 = \gamma_N B_0$. We can transform to the rotating reference frame with the rotation operator

$$R = \exp(i\omega t I^z) \tag{2.28}$$

If $\tilde{H} = RHR^\dagger$ and $|\tilde{\Psi}> = R|\Psi>$ then Schrodinger's equation can be written as

$$i\frac{d|\tilde{\Psi}>}{dt} = (\tilde{H} - iR\dot{R}^\dagger)|\tilde{\Psi}> \tag{2.29}$$

and, since $iR\dot{R}^\dagger = \omega I^z$,

$$\begin{aligned} i\frac{d|\tilde{\Psi}>}{dt} &= -\left((\Omega_0 + \omega)I^z + \frac{\gamma_N}{2}(b^+ e^{-i\omega t} I^- + b^- e^{i\omega t} I^+)\right)|\tilde{\Psi}> \\ &= -\left((\Omega_0 + \omega)I^z + \gamma_N b I^x\right)|\tilde{\Psi}> \\ &= -\vec{\Omega} \cdot \vec{I}|\tilde{\Psi}> \\ &= -\gamma_N \vec{B}_{eff} \cdot \vec{I}|\tilde{\Psi}> \end{aligned} \tag{2.30}$$

where $\vec{\Omega} = (\Omega_0 + \omega)\hat{u}_z + \gamma_N b\hat{u}_x = \gamma_N \vec{B}_{eff}$. This is exactly the same effective field as found in the classical treatment.

Clearly, the eigenvalues of this system are given by

$$E_m = |\vec{\Omega}|m \tag{2.31}$$

and the eigenvectors are the usual eigenvectors of I^z, but rotated an angle θ, given by $\tan(\theta) = \frac{\gamma_N b}{\Omega_0+\omega}$ towards the x-axis. In other words, the eigenvectors are given by

$$|\tilde{\Psi}_m >= e^{-i\theta I^y}|m > \tag{2.32}$$

For NMR, we are interested in the rate of transitions between different eigenstates of the unperturbed Hamiltonian, under the influence of the oscillating magnetic field. If, at time $t = 0$, the system is in a state $|\Psi > (0) = |\tilde{\Psi} > (0) = |m >$, then

$$\begin{aligned} |\Psi > (t) &= R^\dagger |\tilde{\Psi} > (t) \\ &= R^\dagger \exp\left(-i\vec{\Omega}\cdot\vec{I}t\right)|m > \end{aligned} \tag{2.33}$$

We can calculate $< \mu_z >= \gamma_N < I^z >$ when $\omega = -\Omega_0$ and find

$$< \mu_z >= \gamma_N < m|e^{i\gamma_N bI^x t} I^z e^{-i\gamma_N bI^x t}|m > \tag{2.34}$$

Since $< m|I^y|m >= 0$, and using

$$e^{i\gamma_N bI^x t} I^z e^{-i\gamma_N bI^x t} = I^y \sin(\gamma_N bt) + I^z \cos(\gamma_N bt) \tag{2.35}$$

Then, if $m = I$, we have

$$< \mu_z >= \gamma_N I \cos(\gamma_N bt) \tag{2.36}$$

In other words, the magnetic moment precesses between $\pm\gamma_N I = \pm\mu$ at a frequency $\gamma_N b/2\pi$. This is exactly the result of the classical case.

The probability of finding the system in a state $|n>$ at time t is given by

$$\begin{aligned} P(t) &= |<n|\Psi>(t)|^2 \\ &= |<n|R^{\dagger}\exp\left(-i\vec{\Omega}\cdot\vec{I}t\right)|m>|^2 \\ &= |<n|\exp\left(-i\vec{\Omega}\cdot\vec{I}t\right)|m>|^2 \end{aligned} \tag{2.37}$$

In the case $I = 1/2$, $P(t)$ is easy to calculate, although for NO involving γ radiation there is no anisotropy when $I = 1/2$. Using the Pauli matrices, $\vec{\sigma}/2$, as a representation of $\vec{I}$ and

$$\exp\left(i\alpha\vec{u}\cdot\vec{\sigma}\right) = \cos(\alpha) + i\vec{u}\cdot\vec{\sigma}\sin(\alpha) \tag{2.38}$$

we have the probability of transition after a time t, from the $|+>$ state to the $|->$ state, given by

$$P(t) = \frac{\sin^2(|\Omega|t/2)}{|\Omega|^2}|\gamma_N b|^2 \tag{2.39}$$

The approximate solution for general I, needed for NO, is the same, with $|\gamma_N b|^2$ replaced with $4|W_{fi}|^2$ where W_{fi} is the matrix element connecting final and initial states [7].

In pulsed NMR, the pulse time can be calculated to give π or $\pi/2$ rotations of the spin based on equation 2.36 or 2.39. In this case, it is clear that b should be as large as possible.

In CW NMR, in the limit where t is large but $t|\gamma_N b| \ll 1$, we can use the relationship

$$\lim_{\varepsilon\to 0}\frac{\varepsilon}{\pi}\frac{\sin^2(x/\varepsilon)}{x^2} = \delta(x) \tag{2.40}$$

and, with $t = 1/\varepsilon$,

$$P(t) \simeq 2\pi|W_{fi}|^2\delta(\Omega_0 - \omega)t \tag{2.41}$$

The transition rate, $Q_{fi} = dP(t)/dt$, is

$$Q_{fi} \simeq 2\pi|W_{fi}|^2\delta(\Omega_0 - \omega) \tag{2.42}$$

which is exactly the result predicted by Fermi's Golden Rule. Note that $Q_{fi} = Q_{if}$, a condition necessary to show that CW NMR will equalize the populations of two levels.

2.4 Spin-lattice relaxation

We will now consider in more detail the interactions with the lattice which allow the nuclear moments to achieve thermal equilibrium with the lattice. In many cases, the dominant mechanism orienting the nuclear spins is the hyperfine interaction, $H = \vec{I} \cdot \mathbf{A} \cdot \vec{S}$ where $\vec{I}$ is the nuclear spin, $\vec{S}$ is the electron spin and $\mathbf{A}$ is the hyperfine coupling tensor.

The electronic spins have time dependent fluctuations away from their equilibrium values. It is these dynamic fluctuations, equivalent to a fluctuating magnetic field, that provide the mechanism for the nuclear spins to relax to the lattice temperature. In order to calculate the transition rate, it is convenient to write $\vec{S}(t) = \vec{S}_0 + \delta\vec{S}(t)$ where $\vec{S}_0$ is the static electronic spin and $\delta\vec{S}(t)$ is the small time dependent fluctuation of the electronic spin.

We can then write the hyperfine interaction in the form

$$\begin{aligned} H_{HF} &= \vec{I} \cdot \mathbf{A} \cdot \vec{S}(t) \\ &= \vec{I} \cdot \mathbf{A} \cdot \vec{S}_0 + \vec{I} \cdot \mathbf{A} \cdot \delta\vec{S}(t) \\ &= H_{HF}(0) + H'(t) \end{aligned} \tag{2.43}$$

and find the transition rate using time dependent perturbation theory in $H'(t)$.

We define N_m as the number of nuclei with $I^z = m$. For NMRON, the interaction between the radioactive nuclear spins is very weak because they are so dilute. In this case, the relaxation of the nuclear ensemble back to thermal equilibrium is governed by

$$\frac{dN_m}{dt} = N_{m+1}Q_{m+1,m} - N_m(Q_{m,m+1} + Q_{m,m-1}) + N_{m-1}Q_{m-1,m} \tag{2.44}$$

where $Q_{m,n}$ is the transition rate between a level m and n. We have assumed only transitions between adjacent levels because of angular momentum conservation. At equilibrium

with a thermal bath (the lattice) at a temperature T_L, we know that

$$\frac{N_{m+1}}{N_m} = \exp(\frac{-\Delta E}{k_B T_L}) \tag{2.45}$$

where $\Delta E = E_{m+1} - E_m$, and therefore $Q_{m,m+1} = Q_{m+1,m}\exp(\frac{-\Delta E}{k_B T_L})$.

The nuclear spin-lattice relaxation time, T_1, is defined by

$$\begin{aligned} \frac{1}{T_1} &= \frac{Q_{m+1,m} + Q_{m,m+1}}{I(I+1) - m(m+1)} \\ &= \frac{Q_{m,m+1}(1 + \exp(\Delta E/k_B T_L))}{I(I+1) - m(m+1)} \end{aligned} \tag{2.46}$$

and therefore

$$\begin{aligned} Q_{m,m+1} &= \frac{1}{T_1}\frac{I(I+1) - m(m+1)}{1 + \exp(\Delta E/k_B T_L)} \\ Q_{m+1,m} &= \frac{1}{T_1}\frac{I(I+1) - m(m+1)}{1 + \exp(-\Delta E/k_B T_L)} \end{aligned} \tag{2.47}$$

$Q_{m,m+1}$ can also be calculated using Fermi's Golden Rule. If we assume that the electronic spin system has a probability $\exp(-E_n/k_b T_L)/Z_S$ of being in a state n of energy E_n and the nuclear spin is in a state $I^z = m$ of energy E_m. The transition rate is

$$Q_{m,m+1} = 2\pi \sum_{n,n'} | < m+1, n'|H'(t)|m, n > |^2 \delta(E_{n'} + -E_n + \Delta E)\frac{\exp(-E_n/k_b T_L)}{Z_S} \tag{2.48}$$

The only terms of $H'(t)$ that contribute are those involving I^+. Assuming for simplicity that the hyperfine coupling, A, is isotropic then

$$\begin{aligned} Q_{m,m+1} &= \pi A^2 (I(I+1) - m(m+1)) \\ &\times \sum_{n,n'} | < n'|\delta S^-(t)|n > |^2 \delta(E_{n'} - E_n + \Delta E)\frac{\exp(-E_n/k_b T_L)}{Z_S} \end{aligned} \tag{2.49}$$

Since $\delta(E_{n'} - E_n + \Delta E) = \frac{1}{2\pi}\int_{-\infty}^{\infty} dt\, e^{-i(E_{n'} - E_n + \Delta E)t}$, and $\delta S^-(t) = e^{iHt}\delta S^-(0)e^{-iHt}$ we have

$$Q_{m,m+1} = (I(I+1) - m(m+1))\frac{A^2}{2}\int_{-\infty}^{\infty} dt\, e^{-i\Delta E t} < \delta S^+(t)\delta S^-(0) > \tag{2.50}$$

We can calculate $Q_{m+1,m}$ in the same fashion and it can be shown that $Q_{m+1,m} = Q_{m,m+1}\exp(\frac{\Delta E}{k_B T_L})$, as expected. Comparison with equation 2.47 gives a value for $1/T_1$ of

$$\frac{1}{T_1} = \frac{A^2}{2}\int_{-\infty}^{\infty} dt\, e^{-i\Delta E t} < \delta S^+(t)\delta S^-(0) > (1 + \exp(\Delta E/k_B T_L)) \qquad (2.51)$$

where the brackets <> indicate a thermal average, ie $< O >= Tr[e^{-\beta H}O]/Z$. This relates the relaxation time to the Green's function $< \delta S^+(t)\delta S^-(0) >$ and is the same expression given by [8, 9].

For magnetic systems, the relaxation time can, in principle, be calculated at low temperatures using spin wave theory. Since $\vec{S}_0$ from equation 2.43 is simply $S\vec{u}_z$, $\delta S^+ = S^+ \simeq \sqrt{2S}a$ and $\delta S^- = S^- \simeq \sqrt{2S}a^\dagger$, where a and $a^\dagger$ are bosonic annihilation and creation operators. The relaxation time can be calculated if the electronic magnon spectrum is known. In particular, it is clear that the relaxation time will become shorter if the electronic magnon energy gap becomes small. If it is possible to modify the size of the gap, then T_1 can be changed. This effect will be discussed further when dealing with magnon cooling in $MnCl_2{\cdot}4H_2O$.

2.5 RF enhancement

When NMR is performed on a magnetic material, the oscillating field $\vec{b}$ is enhanced. This makes it easier to perform NMR because the strength of the oscillating field at the nucleus can be much larger than the applied oscillating field.

The effective field orienting an electronic spin is given by

$$\vec{B}_{eff} = \vec{B}_A + \vec{B}_0 \qquad (2.52)$$

where $\vec{B}_A$ and $\vec{B}_0$ are the anisotropy and applied fields respectively. When the RF field is applied, in general perpendicular to the orienting field, the total field on the electronic

spin is

$$\vec{B}_{or} = \vec{B}_{eff} + \vec{b} \tag{2.53}$$

If the electronic magnetic moment follows the orienting field adiabatically, the hyperfine field $\vec{B}_{hf} = A\vec{S}/\gamma_N$ also follows the direction of the field $\vec{B}_{or}$. The total magnitude of the field at the nucleus precessing at frequency ω in the x-y plane is given by the sum of $\vec{b}$ and the perpendicular component of $\vec{B}_{hf}$, therefore

$$\begin{aligned} b_{tot} &= b + B_{hf}\frac{b}{B_{or}} \\ &\simeq b\left(1 + \frac{B_{hf}}{B_{eff}}\right) \end{aligned} \tag{2.54}$$

Since it is often the case that $B_{hf}/B_{eff} \gg 1$, there can be significant enhancement of the applied RF field. This effect is shown schematically in figure 2.6.

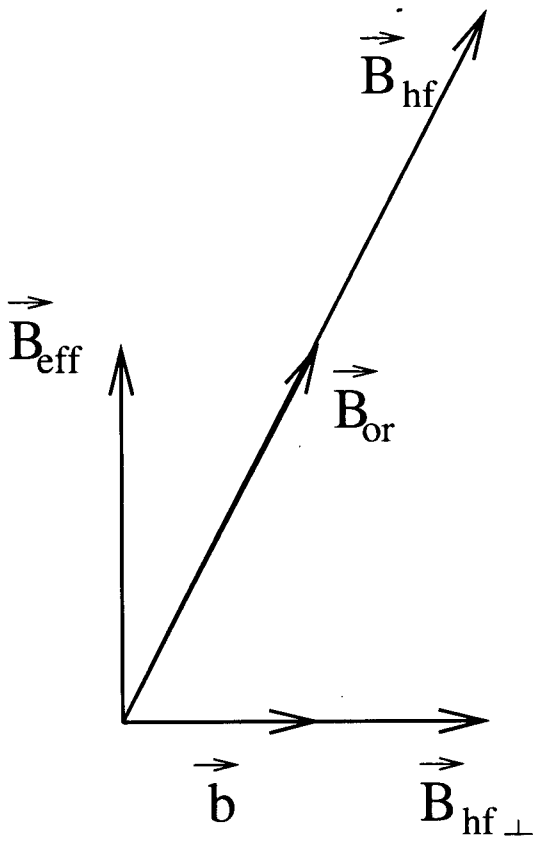

Figure 2.6: A diagram of the enhancement effect. The perpendicular component of B_{hf} is added to the applied RF field b when performing NMR on magnetic materials.

Chapter 3

Radiofrequency Circuits for Nuclear Magnetic Resonance

When performing NMR, the radiofrequency (RF) magnetic field is usually provided by a coil, although in some very high frequency applications a microwave cavity is used to provide high frequency fields. In the experiments considered here, the oscillating magnetic field was provided by a coil because the frequencies used were always less than 1 GHz.

For CW NMR, the strength of the magnetic field is not always the most important consideration. For long relaxation times, applied oscillating fields of 10^{-7} T can be sufficient to saturate the resonance, due to the enhancement of the RF field, so that good impedance matching of the resonant circuit to the transmission line is not always necessary.

The NMR experiments presented here sometimes involved sweeping the frequency of the RF field over ranges greater than 100 MHz. This type of measurement requires an RF coil, tuning circuit and transmission lines that can provide a constant intensity of magnetic field over the entire sweep range. If the intensity of the field changes dramatically, for example due to cable or circuit resonances, it is possible to miss observing resonances due to an insufficient magnetic field at the resonant frequency, or to detect false resonances due to the increased RF heating near a cable or circuit resonance.

In this chapter a quantitative analysis of circuits for NMRON and NMR-TDNO experiments is presented. A model that includes the effects of an arbitrary number of transmission lines and an RF generator is developed to calculate the power spectrum of

the circuits.

3.1 General considerations

3.1.1 Ideal case

An electromagnetic wave travelling down a transmission line terminated by an impedance, Z, is reflected with an amplitude ratio $r = \frac{Z-R_0}{Z+R_0}$, where R_0 is the characteristic impedance of the tranmission line. The voltage and current in the transmission line, for a wave of frequency $\nu = \omega/2\pi$, are given by

$$\begin{aligned} v &= v_0 \left(e^{i(wt-k(x-L))} + re^{i(wt+k(x-L))}\right) \\ i &= \frac{v_0}{R_0}\left(e^{i(wt-k(x-L))} - re^{i(wt+k(x-L))}\right) \end{aligned} \tag{3.55}$$

where L is the length of the cable. The power dissipated by the impedance is given by

$$\begin{aligned} P &= \nu \int_0^{1/\nu} \Re(i)\Re(v) \\ &= \frac{|v_0|^2}{2R_0}\left(1-|r|^2\right) \end{aligned} \tag{3.56}$$

where $\Re(i)$ and $\Re(v)$ are the real parts of i and v respectively.

Since the usual coil set-up is much smaller than the wavelength of the electromagnetic field, we can calculate the magnetic field produced using DC formulae. In our experiments, a single turn coil was used in order to keep the inductance as low as possible. In this case, the field at the centre of the coil is given by

$$B = \frac{\mu_0 i}{2r_c} \tag{3.57}$$

where r_c is the radius of the coil.

For a typical geometry, $r_c \sim 0.5$ cm and oscillating fields of 10^{-7} T can be produced by currents on the order of 1 mA.

3.1.2 A more complete model

At frequencies greater than 100 MHz, the equations for the voltage and current are more complicated because v_0 in equations 3.55 and 5.38 depends not only on the generator voltage, but also on the precise setup of transmission lines between the generator and the circuit. Stray capacitances and mismatched impedances between the different sections of coaxial cable can have important effects. For example, at a frequency of 500 MHz, a capacitance of 1 pF has an impedance of approximately 300 Ω. We shall consider a

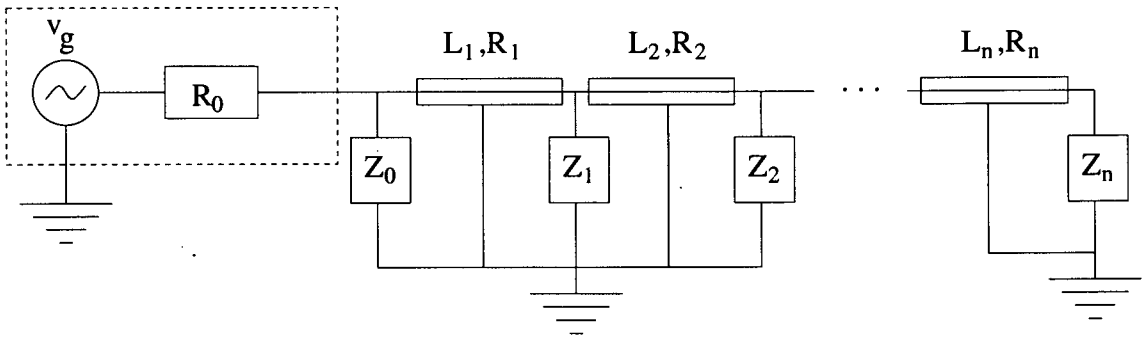

Figure 3.7: The typical configuration for an NMR coil. The frequency generator, of output impedance R_0 drives n lengths of coaxial cable. Each cable, j, has a length L_j and characteristic impedance R_j. At the connection between cable j and $j+1$ is an impedance to ground, Z_j. This impedance is generally due to capacitive coupling in the connectors, and is typically on the order of 1 pF. Z_n is the impedance of the NMR coil.

typical situation (see Fig 3.7) involving a frequency generator of characteristic output impedance R_0, with an impedance Z_0 to ground driving n sections of coaxial cable, each with characteristic impedance R_j, length L_j connected to the next cable $(j+1)$, and an impedance to ground, Z_j. Z_n is the impedance of the coil circuit. The voltage and current in the jth section is given by

$$\begin{aligned} v_j &= v_{0j}\left(e^{i(wt-k(x-l_j))} + r_j e^{i(wt+k(x-l_j))}\right) \\ i_j &= \frac{v_{0j}}{R_j}\left(e^{i(wt-k(x-l_j))} - r_j e^{i(wt+k(x-l_j))}\right) \end{aligned} \tag{3.58}$$

where l_j is position of the end of each section of cable (ie $L_j = l_j - l_{j-1}$). The generator voltage is $v_g = v_{0g}e^{iwt}$.

Applying Kirchoff's laws to each cable connection, we find that

$$\begin{pmatrix} v_{0j-1} \\ v_{0j-1}r_{j-1} \end{pmatrix} = \begin{pmatrix} M_{11} & M_{12} \\ M_{21} & M_{22} \end{pmatrix}_j \begin{pmatrix} v_{0j} \\ v_{0j}r_j \end{pmatrix} = M_j \begin{pmatrix} v_{0j} \\ v_{0j}r_j \end{pmatrix} \tag{3.59}$$

where

$$\begin{aligned} M_{11} &= \frac{1}{2}e^{ik_jL_j}\left(1 + \frac{R_{j-1}}{R_j} + \frac{R_{j-1}}{Z_{j-1}}\right) \\ M_{12} &= \frac{1}{2}e^{-ik_jL_j}\left(1 - \frac{R_{j-1}}{R_j} + \frac{R_{j-1}}{Z_{j-1}}\right) \\ M_{21} &= \frac{1}{2}e^{ik_jL_j}\left(1 - \frac{R_{j-1}}{R_j} - \frac{R_{j-1}}{Z_{j-1}}\right) \\ M_{22} &= \frac{1}{2}e^{-ik_jL_j}\left(1 + \frac{R_{j-1}}{R_j} - \frac{R_{j-1}}{Z_{j-1}}\right) \end{aligned} \tag{3.60}$$

Applying Kirchoff's laws to the generator leads to

$$\begin{pmatrix} v_{0g} \\ \Phi \end{pmatrix} = \begin{pmatrix} M_{11} & M_{12} \\ M_{21} & M_{22} \end{pmatrix}_1 \begin{pmatrix} v_{01} \\ v_{01}r_1 \end{pmatrix} = M_1 \begin{pmatrix} v_{01} \\ v_{01}r_1 \end{pmatrix} \tag{3.61}$$

where M_{11} and M_{12} have the same definitions as in equations 3.60, and Φ is arbitrary and depends on the choice of M_{21} and M_{22}. Since Φ is not needed, M_{21} and M_{22} can be chosen to have the same definitions as in equations 3.60. Finally, we can write

$$\begin{pmatrix} v_{0g} \\ \Phi \end{pmatrix} = M_1M_2...M_n \begin{pmatrix} v_{0n} \\ v_{0n}r_n \end{pmatrix} \tag{3.62}$$

If $G = M_1M_2...M_n$, then

$$v_{0n} = \frac{v_{0g}}{G_{11} + r_nG_{12}} \tag{3.63}$$

Since $r_n = \frac{Z_n - R_n}{Z_n + R_n}$, we can easily calculate the power spectrum,

$$\begin{aligned} P &= \frac{|v_n|^2}{2R_n}\left(1 - |r_n|^2\right) \\ &= \frac{|v_{0g}|^2}{2R_n|G_{11} + r_nG_{12}|^2}\left(1 - |r_n|^2\right) \end{aligned} \tag{3.64}$$

A good coil design is one that provides a frequency response that is relatively insensitive to small changes in the parameters Z_j, R_j and L_j. A coil not satisfying this requirement will present serious experimental difficulties, even if the power spectrum predicted in equation 3.56 appears satisfactory. These considerations are extremely important because of the relatively high RF frequencies used (100 to 700 MHz).

3.2 Tuned LC circuits

We shall first consider several tuned LC circuits and their usefulness in NMR at frequencies of 100 MHz to 1 GHz. The inductance of the coil can be calculated from its dimensions [10]. For a single turn, approximately 1 cm in diameter, of 1 mm thick magnet coil, $L \sim 10^{-8}$ H.

For an inductance of this magnitude, the series configuration (see Figure 3.8) is not desirable because any inductance in the leads of the circuit is of similar magnitude to the inductance of the coil itself. The inductance adds to the inductance of the coil thereby reducing the resonant frequency and making external tuning very difficult.

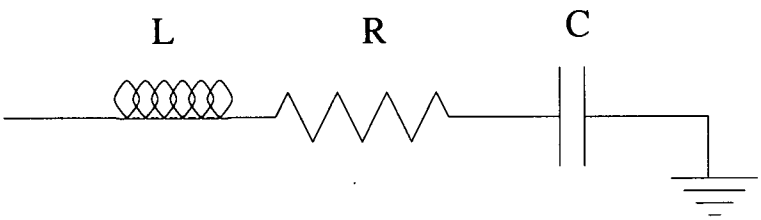

Figure 3.8: The series configuration. The resistor, R, may be only the resistance of the coil itself.

The parallel configuration (see Figure 3.9) allows the coil itself to be isolated. This is useful for measuring the exact inductance of the coil. However, it is not possible to control the quality factor, Q, of the resonance without introducing a resistor.

A useful configuration is a combination of the series and parallel circuits (see Figure

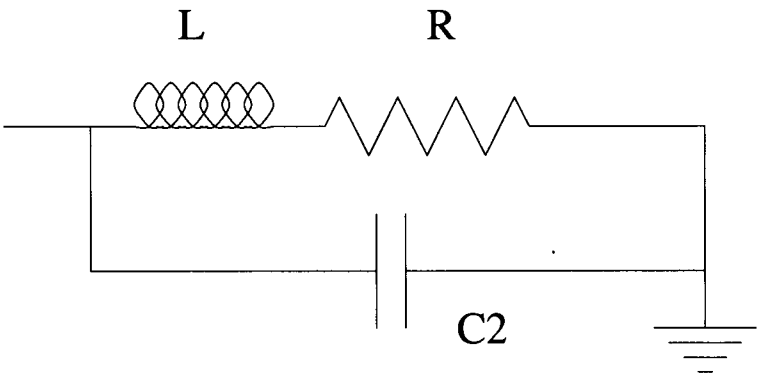

Figure 3.9: The parallel configuration. The resistor, R, may be only the resistance of the coil itself.

3.10). The best use of this circuit is to fix C_2 and allow C_1 to be variable. C_2 should be chosen to give the desired Q of the circuit, then the variable C_1 can be used to tune the resonance to the desired frequency. The final adjustments to the resonant frequency should be made when the coil is mounted. Since the stray capacitance to ground is not negligible at the frequencies of interest ($\sim$ 500 MHz), there will be some shift, normally on the order of 10 MHz or less, when the copper shielding is placed around the sample in the dilution refrigerator. Finally, it is important to take into account the shifts in frequency as the circuit is cooled. Between room temperature and 77 K, the resonant frequency can shift as much as 40 MHz, but below 77 K, there is little change. The coil should, therefore, be tuned to the correct frequency in liquid nitrogen.

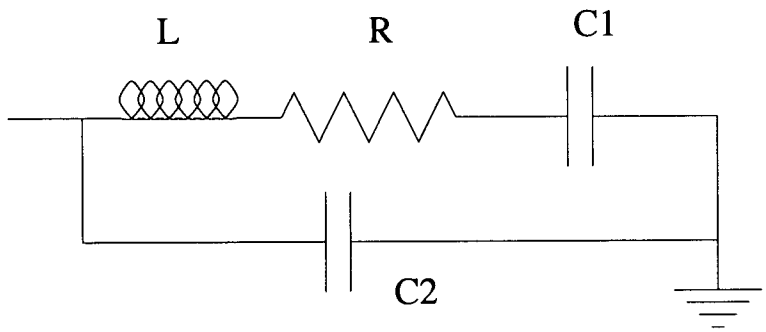

Figure 3.10: Series-parallel configuration

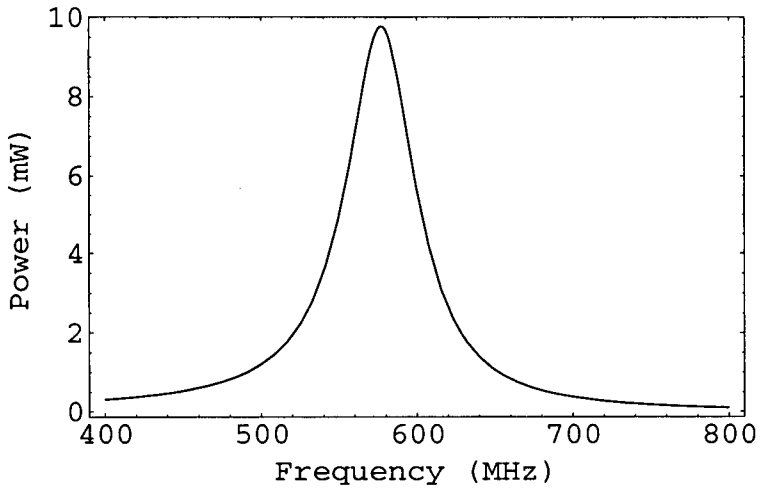

Figure 3.11: The power spectrum for a series-parallel coil connected to an ideal transmission line, calculated from equation 3.56. The coil has $L = 7 \cdot 10^{-9}$ H, $C_2 = 33$ pF, $C_1 = 16$ pF and $R = 1\ \Omega$. The generator voltage is $v_{0g} = 1$ V

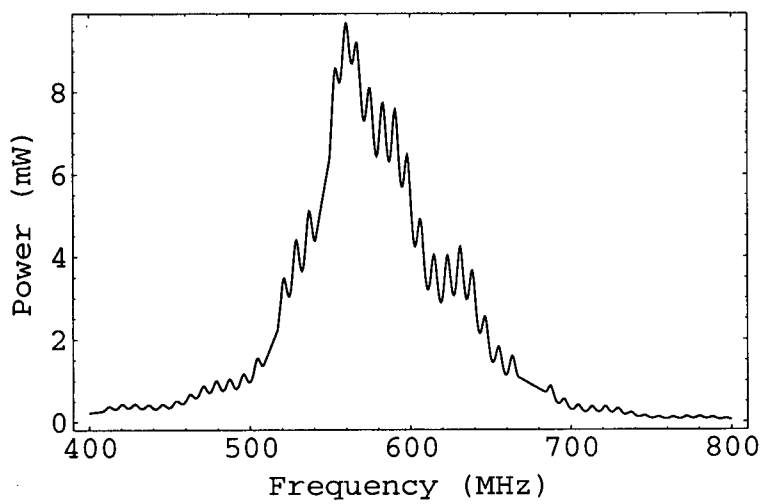

Figure 3.12: The power spectrum (calculated from equation 3.64) for the same coil as figure 3.11, but connected to a generator and a series of 4 transmission lines as in figure 3.7. The parameters are $L_1 = 10$ m, $L_2 = 1.5$ m, $L_3 = 0.10$ m, $L_4 = 0.30$ m, $Z_0 = Z_1 = Z_2 = Z_3 = 1$ pF, $R_0 = R_1 = 50\ \Omega$, $R2 = 53\ \Omega$, $R3 = 55\ \Omega$ and $R_4 = 40\ \Omega$.

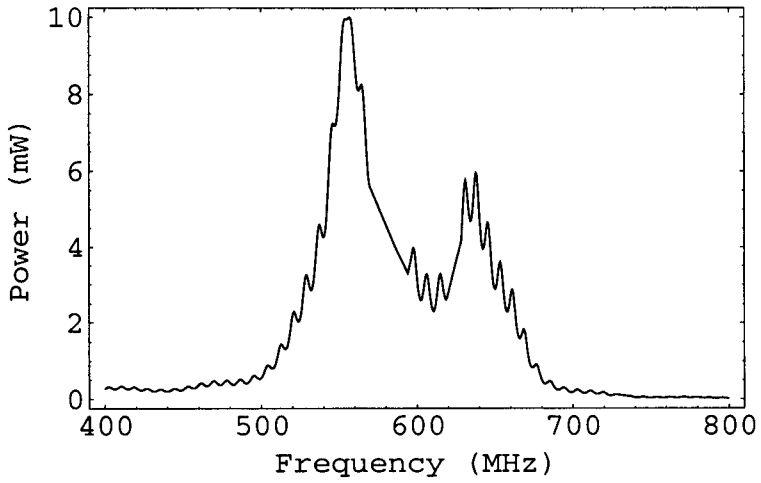

Figure 3.13: The power spectrum for the same coil as figure 3.11, calculated from equation 3.64. The parameters are the same as figure 3.12 except for Z_2. Here, $Z_2 = 5$ pF.

A simulation of a typical power spectrum for the series-parallel configuration is shown in figures 3.11, 3.12 and 3.13. Although no resistor is placed in series with the coil, the resistance of $R = 1\ \Omega$ was used. This value is higher than the DC resistance of the coil (typically less than 0.1 Ω), but the skin effect as well as the losses due to the RF radiation at higher frequencies increase the resistance. The value of 1 Ω is consistent with the observed quality factor, Q. The resistor is the only component of the coil that can dissipate power, and P is proportional to the square of the current through the resistor. The current through the resistor and the inductor (the coil) is the same and proportional to the magnetic field. Therefore, the power dissipated in the coil is proportional to the square of the magnetic field.

It is clear that the transmission lines have a large effect on the power spectrum of the coil. In one possible case (see figure 3.13), the resonance is split into two peaks only because of a 5 pF capacitance to ground between two transmission lines leading to the coil. The series-parallel coil, with $C_1 = 16$ pF and $C_2 = 33$ pF, is a good design because the resonant frequency is not significantly shifted by the presence of the transmission

lines.

When tuning coils at frequencies greater than 100 MHz, it is useful to measure the amplitude of the voltage at the input to the coil. This can be achieved with a fast oscilloscope, or using a detector which converts the high frequency signal to a DC voltage (a Pasternack 8000-50 is a good example of such a detector). Although the DC output voltage of the detector is not precisely a linear function of the input voltage amplitude, it does allow the general shape of the spectrum to be measured and the coil to be accurately tuned. The variation with frequency of the Pasternack 8000-50 is less than 20% from 100 to 600 MHz, for a given input voltage. The use of a sweep generator allows the voltage spectrum to be plotted directly on an oscilloscope. Since the voltage amplitude at the circuit is given by $|v_n| = |v_{0n}(1 + r_n)|$, the voltage spectrum can be compared to simulations of a perfect transmission line being used to drive a series parallel coil (see figure 3.14). The signal actually observed resembles that in figure 3.15, simulated with the same parameters as the power spectrum in figure 3.12.

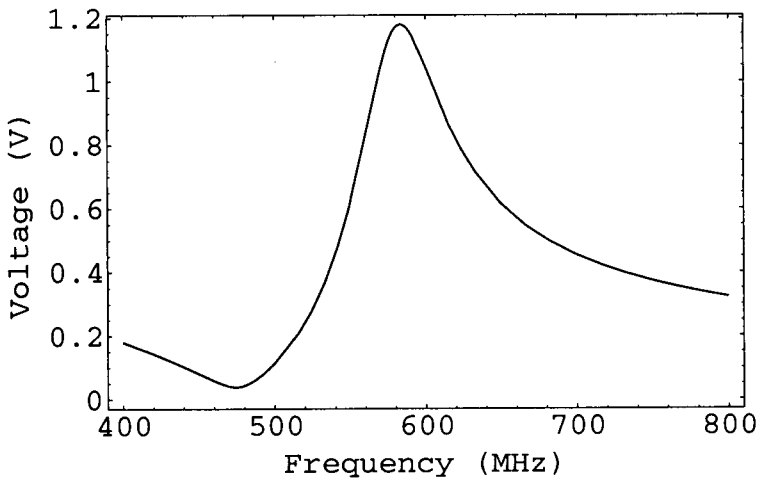

Figure 3.14: The voltage amplitude across the coil as a function of frequency (calculated from equation 3.55) corresponding to the power spectrum in figure 3.11

The tuned LC circuit is useful when the magnitude of the oscillating magnetic field

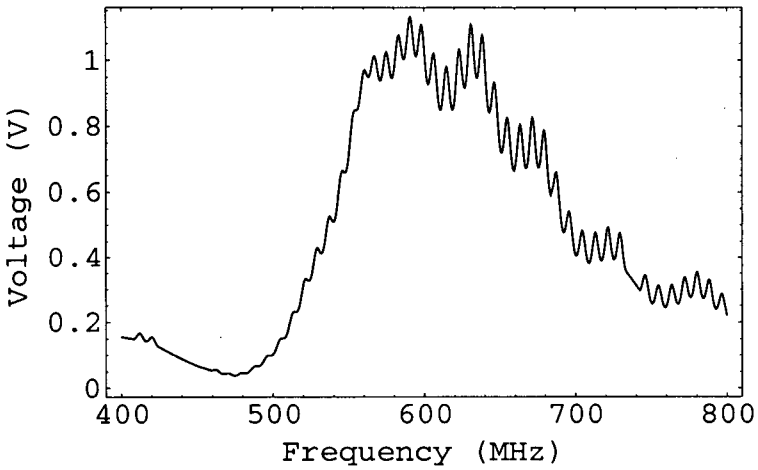

Figure 3.15: The voltage across the coil as a function of frequency (calculated from equation 3.63) corresponding to the power spectrum in figure 3.12

is an important factor. However, it has two disadvantages. Firstly, the amplitude of the magnetic field away from resonance can be too small to perform NMR, thereby reducing the frequency range over which the coil is useful. This is an important factor to consider when searching for resonances. Secondly, the amplitude of the magnetic field varies greatly with frequency near resonance and heating of the the cold finger due to increased RF power can lead to the observation of false NMR resonances. In many cases this problem can be avoided by tuning the coil resonance slightly off the NMR resonant frequency, such that the NMR frequency is situated in a nearly linear part of the coil resonance. The effect of non resonant heating can then be subtracted from the power spectrum. This is possible when the NMR resonances are narrow compared to the the coil resonance. Of course, the coil resonance cannot be infinitely broadened without sacrificing magnetic field intensity. Another solution is to compare NMR sweeps with and without frequency modulation. If the NMR lines are inhomogeneously broadened, the effects of non resonant RF heating on the cold finger can be subtracted.

If the magnetic field strength is an important consideration, the NMR resonances

are homogeneously broadened, and the frequency needs to be swept over large region (comparable or larger than the width of the coil resonance), then the above solutions to non-resonant heating will not work effectively.

One solution is to use feedback stabilization of the RF power. One example of this method uses a resistor on the cold finger that responds to direct heating by RF radiation. If the response time is short compared to the thermal coupling to the cold finger, the RF power can be accurately stabilized by keeping the value of the resistor constant. The method can be unsatisfactory for NMR-TDNO because the resonance is detected thermometrically so that the stabilization based on the temperature of the cold finger can work to negate the effect of the NMR. While this may not be an issue in specific cases, careful consideration of the time constants and relative thermal couplings of the thermometer and the sample are necessary.

Another possibility is to stabilize with feedback from a small pickup coil. In principle, it is possible to maintain a constant magnetic field at all frequencies. In practice, this is only true over a certain region near the resonant frequency. The size of this region depends on the width of the RF coil resonance, the power of the RF generator, and, most importantly, the coupling between the transmission cables of main RF coil and the pick-up coil inside the cryostat. At frequencies far from resonance, the power to the main coil is often sufficiently high that the signal from the pickup coil is due mainly to coupling in the transmission lines and not in the RF coils themselves. With a careful choice of quality factor for our resonance, stable fields over regions larger than 100 MHz have been achieved with this technique. The feedback loop can be seen in figure 3.16. As we shall discuss in Chapter 4, this feedback stabilization technique is the best way of providing the RF field for NMR-TDNO measurements on manganese acetate tetrahydrate (MnAc).

The pick-up coil should be significantly smaller than the main coil to minimize mutual inductance effects on the latter. The circuit diagram for the pick-up coil used is shown

in Figure 3.17. The resistors, R_1' and R_2' were both chosen to be 100 Ω in order that the total impedance would be matched to the transmission lines. The parallel configuration of the two resistors was chosen to remove any effects of the stray capacitance, C', on the circuit. Since $C' < 1$ pF it is necessary that $R2' \ll 1/wC'$ for frequencies less than 1 GHz. The pickup coil has a flat response in the frequency regions of interest (less than 700 MHz) because its resonant frequency is much greater than 1 GHz.

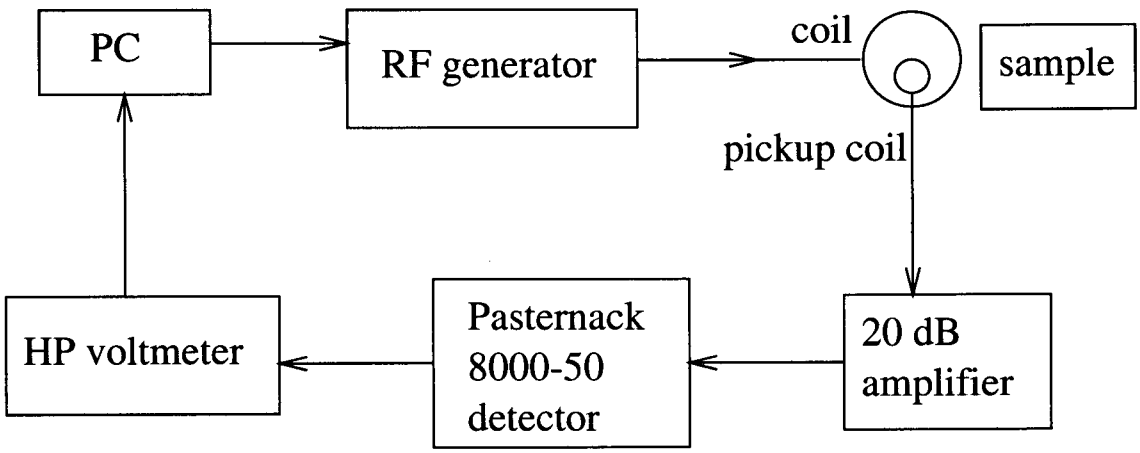

Figure 3.16: The feedback loop which allows the RF power to be stabilized.

The non-linearity of the pick-up circuit with magnetic field intensity is unimportant when sweeping frequency because the feedback loop works to keep its response constant. However, when modifying the RF power, one needs to keep a reference frequency at which the generator voltage can be measured. Then the output of the Pasternack 8000-50 detector can be measured and used as the new setpoint for the feedback loop. In this manner, the pick-up circuit set-point can be related to the magnetic field intensity.

The generator voltage amplitude as a function of frequency during a feedback stabilized frequency sweep is shown in figure 3.18. The circuit is in the series-parallel configuration with component values similar to those used for the simulation in figure 3.11. The frequency is swept through the upper half of the resonance.

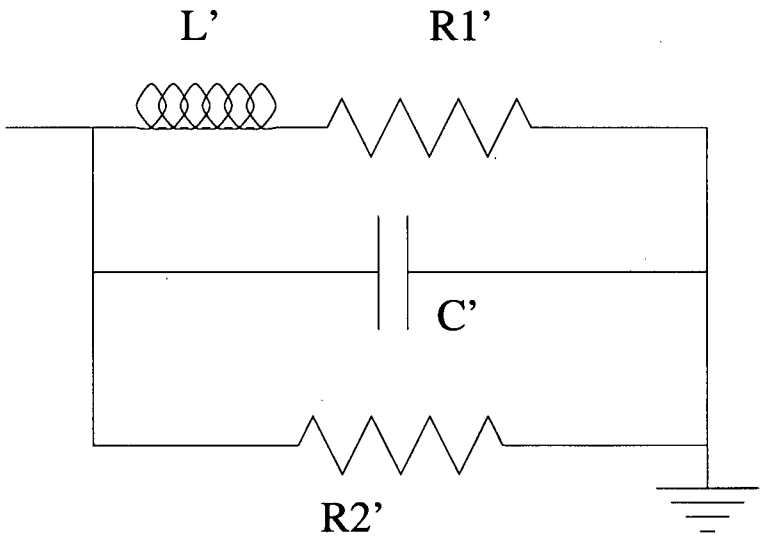

Figure 3.17: The circuit used for the pickup coil. The same circuit, with different component values, is used for the untuned main coil.

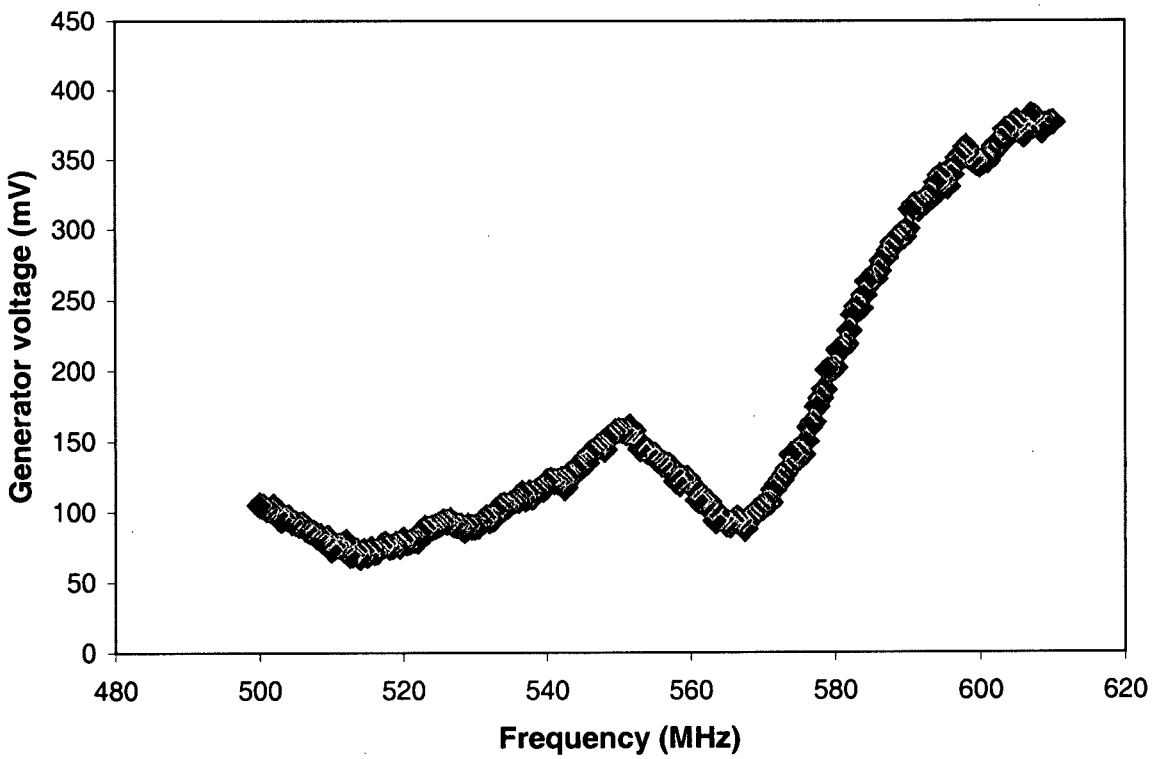

Figure 3.18: The generator voltage, v_g, as a function of frequency for a stabilized sweep near the resonance of a series parallel circuit similar to that of figure 3.10.

3.3 Untuned circuits

When performing CW NMRON to search for resonances of a dilute isotope grown or implanted into a crystal host, it is often necessary to sweep the frequency over large ranges, but the intensity of the field can be as low as 10^{-7} T if the relaxation times are long. In this case, a good solution is to use untuned RF coils. The main coil design is identical to the pickup coil, shown in figure 3.17, except that $R_1' \gg \omega L'$. If $L' \sim 10^{-8}$ H, then $\omega L' \simeq 60\ \Omega$ at a frequency of 1 GHz. If we choose $R1' = 300\ \Omega$, then, $\omega L' \ll R_1'$. We can, therefore, neglect the effect of the coil inductance. R_2' should be chosen such that the total impedance matches the characteristic impedance of the transmission line. If $R_n = 50\ \Omega$, then $R_2' = 60\ \Omega$. Since $C' \sim 1$ pF, $R_2' \ll 1/\omega C'$ for frequencies up to 1 GHz. Our circuit is then approximately the same as two resistors in parallel.

In the ideal case, the resistor R_2' should not be needed. However, as we have seen in the development of the more realistic model, there are reflections off the generator itself as well as the connections between coaxial lines leading down into the dilution refrigerator (DR). It is best, therefore to match impedances to reduce effects of standing waves as much as possible.

Finally, there is the issue of how much power can reasonably be dissipated in the DR. In our setup, the coil was mounted on the 1 K shield. The heat dissipated in the resistors was removed through the 1 K pot. If the voltage at the input has a maximum value of 1 V (peak to peak) then the heat input to the DR is approximately 10 mW. In fact, a generator voltage of 0.4 V was sufficient to saturate the resonance. If the refrigerator is capable of handling a heat load of 1 to 10 mW, then this coil design is extremely practical. At TRIUMF, the LTNO DR has been equipped with an untuned coil design, and a pick up coil to stabilize the power if necessary. In this case, the coil is mounted on the magnet, at 4.2 K, and heat dissipated in the resistors is not a problem.

A simulation of the power spectrum for our circuit is given in figure 3.19 for the ideal case, and figure 3.20 for the more realistic model. The true quantity of interest is the power dissipated in R_1'. This quantity, $P_{tot} - \frac{|v_{0n}(1+r_n)|^2}{2R_2'}$, is proportional to the square of the current in the coil and is shown in figures 3.21 and 3.22. A resistor mounted

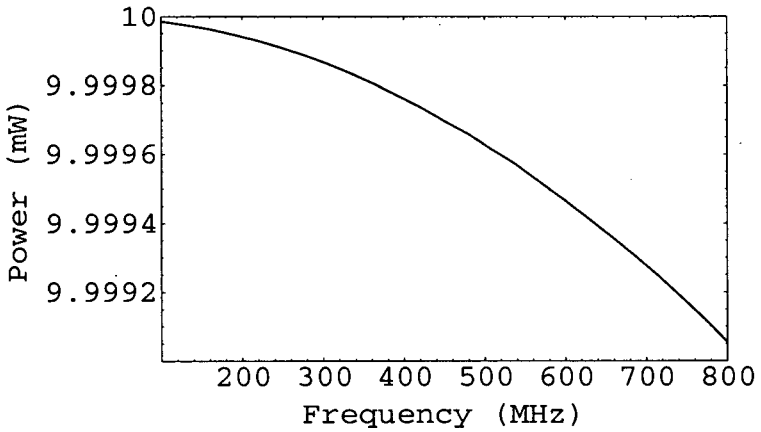

Figure 3.19: The power dissipated in the total circuit (see figure 3.17) as a function of frequency for $L' = 7 \cdot 10^{-9}$ H, $R_1' = 300\ \Omega$, $R_2' = 60\ \Omega$, calculated from equation 3.56. This is the ideal case of a single 50 Ω transmission line leading to the circuit.

on the cold finger was directly heated by the RF field at low temperatures (less than 100 mK). The resistance decreases with increasing temperature and therefore with RF power. A plot of this resistor value is shown in figure 3.23. Although it is difficult to relate the value of the resistor exactly to the RF field, it is possible to see the changes in RF field that are due to standing waves in the coaxial transmission lines in the cryostat. Although it was not necessary for the experiments discussed in this thesis, it would be possible to stabilize an RF coil by keeping the value of this resistor constant. Indeed, the immediate response of this resistor to the RF field make this a promising possibility for feedback stabilization in the future, particularly with tuned RF coils. However, we found that stabilization was unnecessary with our untuned coils because the relative variation in RF power over the frequency ranges of interest was small. There was enough power

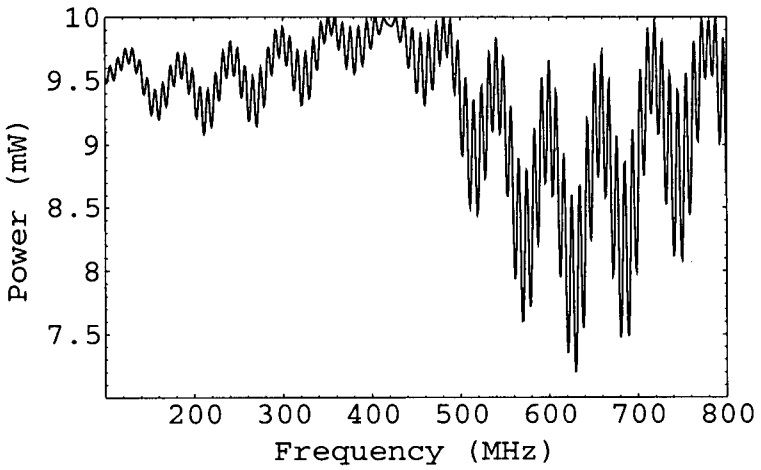

Figure 3.20: The power dissipated in the total circuit as a function of frequency including the effects of the transmission lines and the RF generator, calculated from equation 3.64. The values in the transmission line are the same as in figure 3.12. Note that the most rapid oscillations are due to standing wave resonances in the 10 m line leading to the cryostat. The slower oscillations are due to the 1.5 m line inside the cryostat. The slowest oscillations are due to the 0.3 m line from the 1 K pot to the coil. The oscillations due to the 0.1 m stainless steel line from the 1 K pot to the 4.2 K He bath are not visible in this frequency range.

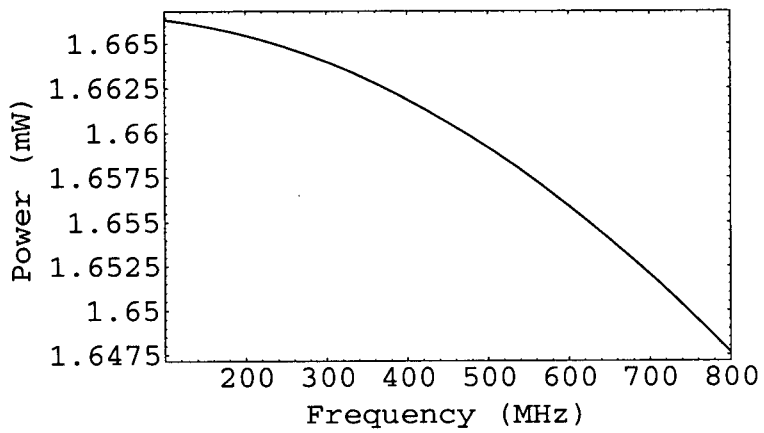

Figure 3.21: The power dissipated in R_1', $P_{tot} - \frac{|v_{0n}(1+r_n)|^2}{2R_2'}$, as a function of frequency. This quantity is proportional to the square of the current in the coil.

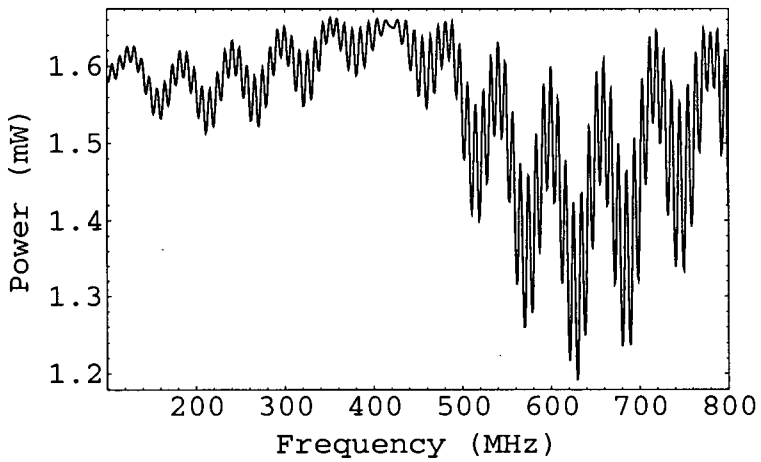

Figure 3.22: The power dissipated in R_1', $P_{tot} - \frac{|v_{0n}(1+r_n)|^2}{2R_2'}$, as a function of frequency including the effects of the transmission lines and the RF generator.

to saturate a resonance, but never so much that RF heating of the cold finger was a problem.

Finally, to illustrate the danger of trusting ideal simulations, figures 3.24 and 3.25, show the results of a simulation of a single coil connected to ground. The resistance of the coil is assumed to be 1 Ω, as before. In the ideal case, it appears that the variation of power (and therefore current and magnetic field) with frequency is small. It would seem possible, therefore, to either stabilize this field, or assume it is a constant over small frequency ranges. However, in the more realistic model, it is clear that there is a large relative variation in power (and magnetic field). Furthermore, this power spectrum is extremely unstable with respect to small changes in the model parameters. In practice, it is very difficult to ensure that enough RF power is reaching the sample, and feedback stabilization is difficult because of the high generator power required relative to the currents produced in the coil.

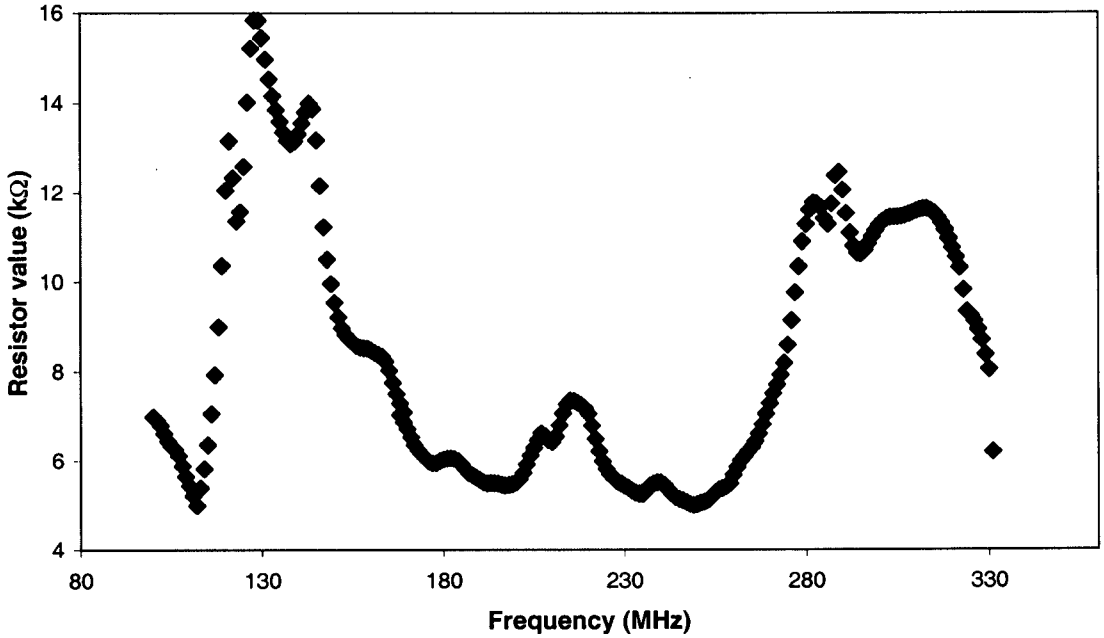

Figure 3.23: The value of a cold finger resistor which responds directly to RF heating as a function of frequency.

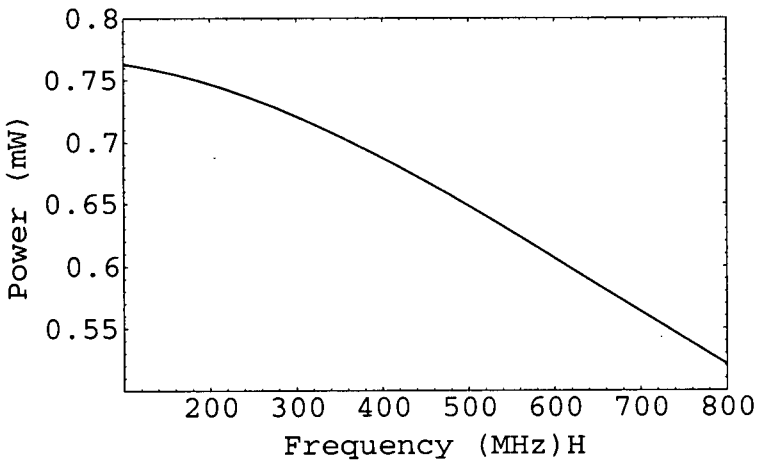

Figure 3.24: The power spectrum of the coil alone in the ideal model ($R_1' = 1\ \Omega$, $R_2' = \infty$), calculated from equation 3.56.

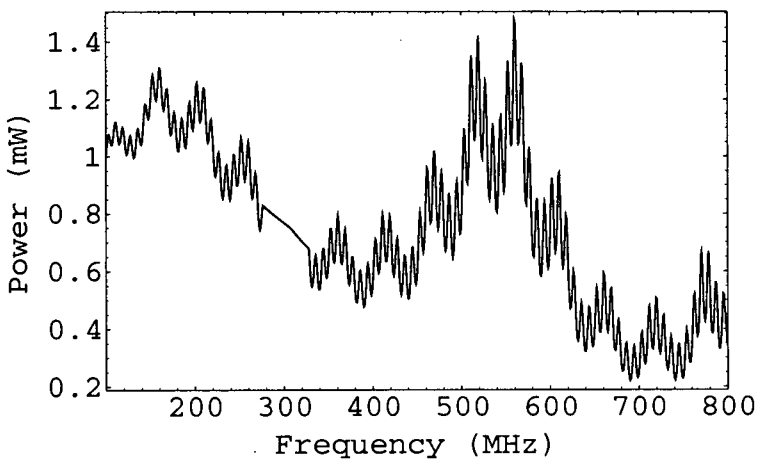

Figure 3.25: The power spectrum of the coil alone including the effects of the transmission lines and the RF generator ($R_1' = 1\ \Omega$, $R_2' = \infty$), calculated from equation 3.64.

Chapter 4

A study of frequency pulling effects in $Mn(COOCH_3)_2 \cdot 4H_2O$

4.1 Introduction

There has been recent interest in the spin dynamics of 2-dimensional spin systems [11] and the study of nuclear spin interactions ("frequency pulling") [12]. In a magnetic system, there is a relatively strong coupling between nuclear spins due to the Suhl-Nakamura interaction that involves the virtual emission and reabsorption of an electronic magnon [13, 14, 3]. At low enough temperatures, the nuclear spins collectively interact with the electron spins causing a shift in the NMR frequency. Also there are excitations of the nuclear spin system (nuclear magnons). We have chosen to investigate these effects in the quasi-2-dimensional ferromagnet manganese acetate tetrahydrate, $Mn(COOCH_3)_2 \cdot 4H_2O$ (MnAc), which exhibits relatively large frequency pulling, by studying the abundant ^{55}Mn nuclear spins and very dilute ^{54}Mn radioactive spins which were doped in the sample during growth. This system has been studied previously by the techniques of NO, NMRON and NMR-TDNO [15] and a preliminary measurement of the frequency pulling showed a relatively large effect.

MnAc has a crystallographic layered (a-b) plane structure [16]. The manganese ions in a given layer occupy two different sites (site 1 and site 2) and are arranged in triplet groups consisting of one Mn1 ion and two Mn2 ions which are internally coupled by 120° oxygen and acetate linkages. Each triplet is coupled to four other triplets within a layer by acetate linkages and there are no strong bonds between layers.

The magnetic properties of MnAc have been studied extensively [16, 17, 18, 19, 20, 21, 22]. Each Mn^{++} ion has $S = 5/2$ and $g \simeq 2.00$ [22, 23]. Magnetically, the oxygen linkages within a triplet provide a strong superexchange that is antiferromagnetic with an exchange constant $J_{AF,tripl} = 48$ K [18]. The superexchange between triplets in a layer is ferromagnetic and much weaker than the intra-triplet antiferromagnetic coupling [17], and the transition to the ordered state occurs at T = 3.19 K. The interlayer coupling ($\sim$ 1 mK) is very weak and antiferromagnetic accounting for the high degree of two dimensionality. The crystal structure and spin orientations of the Mn ions are shown in figure 4.26.

The easy axis is the a-axis, the second easy axis is the c*-axis (perpendicular to the a-b plane) and the hard direction is the b-axis. In order to force the magnetization along the c*-axis (or b-axis) it is necessary to apply a field B_A^c (or B_A^b) along the c*-axis (or b-axis). These fields are called the anisotropy fields and in MnAc they are $B_A^c = 0.135$ T and $B_A^b = 0.86$ T [20]. At very low temperatures, a field $B_0 = 0.6$ mT applied along the easy axis causes a transition from an antiferromagnetic ordering of the ferromagnetic layers to a mixed phase consisting of domains of ferromagnetic and antiferromagnetic ordering of the planes, and at $B_0 = 14$ mT the planes are completely ordered ferromagnetically [15].

The strong antiferromagnetic coupling between the spins in a triplet allows us to treat the latter as an effective single spin with $S = 5/2$, ferromagnetically coupled to its neighbours in the ab-plane. We also ignore the interlayer interaction and treat the system as purely 2-dimensional. With these approximations all triplets are equivalent in terms of their magnetic interactions.

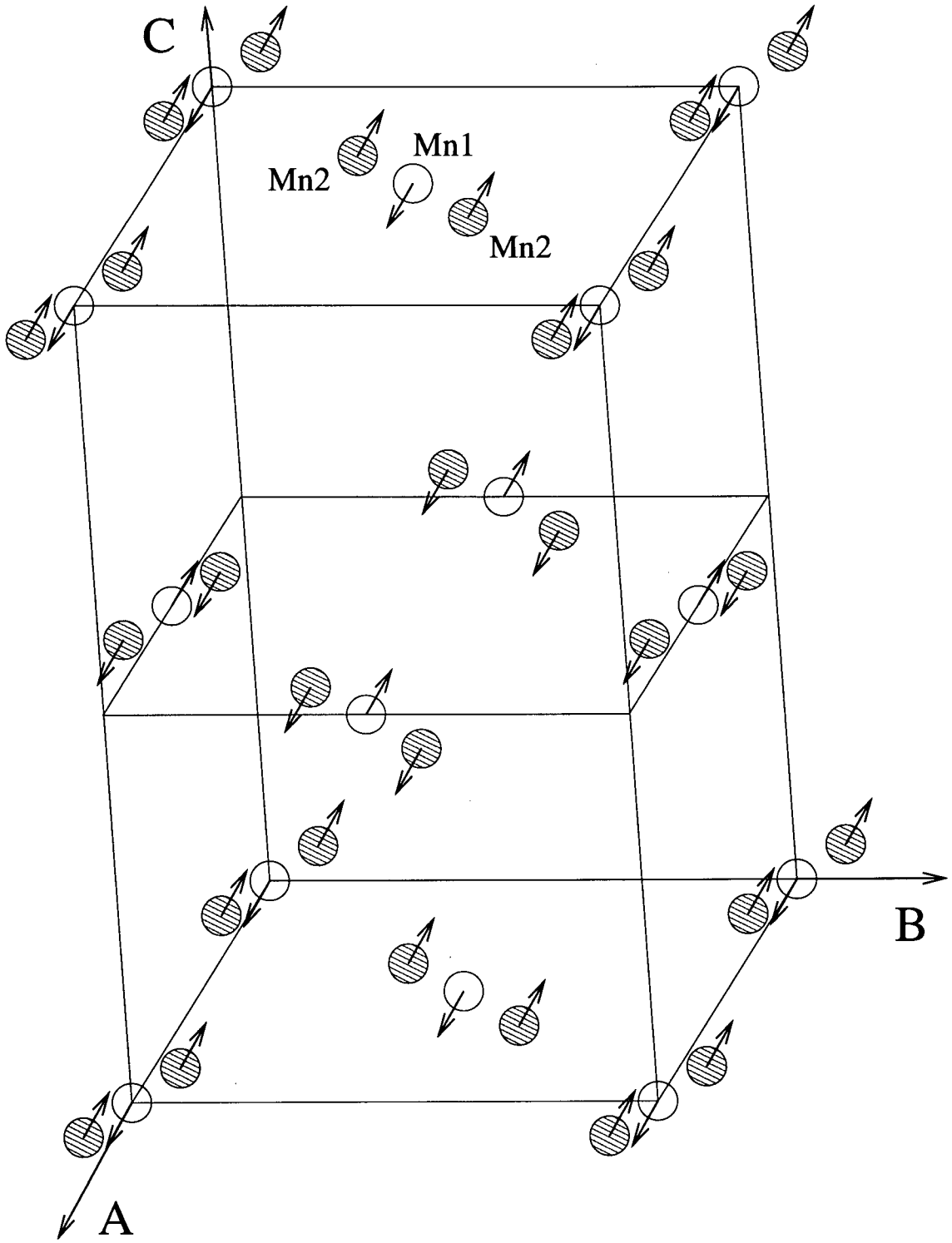

Figure 4.26: The MnAc crystal lattice and magnetization. The easy axis of magnetization is the a-axis.

4.1.1 The ^{54}Mn impurities

A simplified spin Hamiltonian for both the ^{54}Mn1 and ^{54}Mn2 ions in an applied field B_0 is

$$\begin{aligned} H &= H_1 + H_2 && (4.65)\\ H_1 &= g\mu_B(B_E \pm B_0)S^z + D\left[S_z^2 - \frac{1}{3}S(S+1)\right] && (4.66)\\ H_2 &= A\vec{I}\cdot\vec{S} && (4.67) \end{aligned}$$

Here H_1 and H_2 represent the electronic and hyperfine interactions respectively. B_E represents the effective exchange field on a given electronic spin, calculated from mean field theory. The D term represents the crystal field interaction and is related to an anisotropy field by $D = g\mu_B B_A/(2S)$. The term $A\vec{I}\cdot\vec{S}$ represents the hyperfine interaction. The + and - signs are taken for the Mn2 and Mn1 nuclear spins respectively. We have ignored the electric quadrupole interaction and dipole terms which are very small [15]. This Hamiltonian is clearly oversimplified because we have assumed uniaxial anisotropy.

The H_2 term, representing the hyperfine interaction, can be written as $H_2 = H_{HF} + H'_{HF}$ where

$$\begin{aligned} H_{HF} &= AS^zI^z \\ H'_{HF} &= \frac{A}{2}(S^+I^- + S^-I^+) && (4.68) \end{aligned}$$

The effect of H'_{HF} can be treated with perturbation theory.

The zeroth order states of the lowest energy multiplet are characterized by the states $|S^z = -5/2,\ I^z = m>$. The first order correction to the eigenvectors gives a small admixture of the $|S^z = -3/2,\ I^z = m-1>$ states in the lowest energy multiplets. The energy difference between adjacent m and m + 1 levels in $B_0 = 0$, to second order in H'_{HF} is

$$\Delta E_{m,m+1} = -SA + Pm \qquad (4.69)$$

Note that the second order effects lead to an unequal splitting of the lowest energy substates. The "pseudoquadrupolar" term P is given by

$$P = \frac{SA^2}{g\mu_B B_E + 4D} \tag{4.70}$$

4.1.2 The host ^{55}Mn

The abundant ^{55}Mn spins interact via the Suhl-Nakamura interaction [13, 14] that involves the virtual emission of an electronic magnon by one spin and its absorption by another. The Suhl-Nakamura interaction between spins i and j separated by distance r_{ij} can be represented by

$$H_{SN} = \frac{1}{2}\sum_{i,j} U_{ij} I_i^+ I_j^- \tag{4.71}$$

with

$$U_{ij} = -\frac{A^2 S}{N}\sum_k \frac{\exp(ikr_{ij}))}{\omega_k} \tag{4.72}$$

where ω_k is the electronic magnon spectrum. In the case of a simple cubic, three dimensional lattice,

$$U_{ij} = \frac{A^2}{g\mu_b B_E}\frac{a}{r_{ij}}\exp(-\frac{r_{ij}}{b_0}) \tag{4.73}$$

Here a is the lattice spacing and $b_0 \sim (g\mu_B B_E/E_g)a$ where E_g is the magnon energy gap. Typically $b_0 \sim 10$, so that range of the interaction is $\sim 10a$. Actually, the mechanism for the pseudoquadrupolar interaction involves the virtual emission/absorption process by a single spin (U_{ii} term).

The Suhl-Nakamura interaction has a number of effects for abundant nuclei. First the coupling is usually relatively strong causing fast spin-spin relaxation, i.e. short T_2, and this results in a significant homogeneous line broadening which is usually $\delta\nu_{SN} \geq 1$MHz and dominates other contributions. At very low temperatures ($T \ll 1$ K), when there is a significant nuclear magnetization $< I^z >$, the strong Suhl-Nakamura coupling causes

the NMR frequency to be pulled down from the value $\nu_0 = AS/h$, to a value $\nu_0 - \Delta\nu$. Frequency pulling has been discussed e.g. [2, 3], and for the special case $I = 1/2$ at very low temperatures

$$\frac{\Delta\nu}{\nu_0} = \frac{A < I_z >}{E_g} \tag{4.74}$$

There is a band of nuclear magnons, i.e. excitations of the coupled abundant nuclear spins, the spectrum of which covers the range $\nu_0 - \Delta < \nu < \nu_0$. These have been indirectly observed by their effect of enhancing the NSLR of the ^{54}Mn2 compared to ^{54}Mn1 because the frequency of the former is closer to the nuclear magnon band [15].

4.1.3 The effect of the Suhl-Nakamura interaction on the ^{54}Mn impurities

The dilute ^{54}Mn spins are also coupled to their neighbours via the Suhl-Nakamura interaction. The effect of this interaction on the energy levels of the lowest order multiplet can be calculated using perturbation theory.

The ^{54}Mn are sufficiently dilute that we can treat them as a single impurity (at $\vec{R} = 0$) in a lattice of ^{55}Mn spins. The Hamiltonian can be written as

$$\begin{aligned} H &= H_0 + H_{SN} \\ &= AS\sum_j I_j^z + \frac{1}{2}\sum_{i,j} U_{ij} I_i^+ I_j^- \end{aligned} \tag{4.75}$$

We can calculate the correction in energy to a level $|m, \Phi >$ where $m = I_0^z$ is the state of the ^{54}Mn spin and Φ is an arbitrary state of the ensemble of ^{55}Mn spins.

The first order energy correction comes only from the self-interaction term. Since $I^+I^- = I(I+1) - (I^z)^2 + I^z$, the correction to the energy is simply given by

$$\delta E^{(1)} = \frac{1}{2}U_{ii}\left(I(I+1) - m^2 + m\right) \tag{4.76}$$

This first order correction is another way of calculating the pseudoquadrupolar interaction.

The hyperfine coupling constants for ^{54}Mn and ^{55}Mn are different and the second order correction can be calculated using non-degenerate perturbation theory:

$$\begin{aligned}\delta E^{(2)} &= -\sum_{\Phi',m'} \frac{|<m,\Phi|H_{SN}|m',\Phi'>|^2}{E_{m',\Phi'}-E_{m,\Phi}} \\ &= -\sum_j \frac{\left(I_{55}(I_{55}+1)-m'_j(m'_j-1)\right)\left(I_{54}(I_{54}+1)+m(m+1)\right)|U_{0j}|^2}{S(A_{54}-A_{55})} \\ &\quad -\sum_j \frac{\left(I_{55}(I_{55}+1)-m'_j(m'_j+1)\right)\left(I_{54}(I_{54}+1)+m(m-1)\right)|U_{0j}|^2}{S(A_{55}-A_{54})} \end{aligned} \quad (4.77)$$

where A_{54} and A_{55} are the hyperfine coupling constants for the ^{54}Mn and ^{55}Mn spins respectively. $I_{54}=3$ and $I_{55}=5/2$ are the nuclear spins of the ^{54}Mn and ^{55}Mn respectively. We could find a mean field energy correction by replacing m'_j with its thermodynamic average. However, it is clear that

$$\begin{aligned}\delta E^{(2)} &\sim \frac{1}{S(A_{55}-A_{54})}\sum_j |U_{0j}|^2 \\ &\sim \frac{S(A_{54}A_{55})^2}{4N(A_{55}-A_{54})}\sum_k \frac{1}{\omega_k^2} \end{aligned} \quad (4.78)$$

The ratio of the second order correction to the first order correction is then

$$\delta E^{(2)}/\delta E^{(1)} \sim \frac{A_{54}A_{55}}{2(A_{55}-A_{54})}\frac{\sum_k \omega_k^{-2}}{\sum_k \omega_k^{-1}} \quad (4.79)$$

Without calculating the electronic magnon spectrum, it is clear that

$$\sum_k 1/\omega_k^2 \ll 1/\omega_0 \sum_k 1/\omega_k \quad (4.80)$$

and

$$\begin{aligned}\delta E^{(2)}/\delta E^{(1)} &\ll \frac{A_{54}A_{55}}{2(A_{55}-A_{54})\omega_0} \\ &\ll 0.1 \end{aligned} \quad (4.81)$$

Since the first order energy corrections are on the order of 1 MHz, the second order corrections are much less than 100 kHz and can be ignored. The only significant effect

of the Suhl-Nakamura interaction on the ^{54}Mn spins is the self-interaction (or pseudo-quadrupolar term).

4.1.4 Using NMR-TDNO to study the frequency pulling

In order to study the spin dynamics we employ the techniques of NMRON and NMR-TDNO. The magnetic crystal is doped with radioactive ^{54}Mn (a few μCi) during its growth from a saturated solution. The crystal is mounted on the "cold finger" connected to the mixing chamber of a dilution refrigerator and cooled to a temperature 10 mK $< T <$ 100 mK. The nuclear spins are then oriented by the hyperfine interaction and a measure of this orientation is obtained from the angular distribution of γ-rays at 0° and 90°. $W(0)$ and $W(90)$ can be expressed according to equation 2.13, with $a_m(\theta)$ from table 2.2, such that

$$W(0) = \frac{5}{3}(p_2 + p_{-2}) + \frac{4}{3}(p_1 + p_{-1}) + p_0 \tag{4.82}$$

$$W(90) = \frac{5}{4}(p_3 + p_{-3}) + \frac{5}{4}(p_2 + p_{-2}) + \frac{3}{4}(p_1 + p_{-1}) + \frac{1}{2}p_0 \tag{4.83}$$

with p_m given by the Boltzmann factor,

$$p_m = \frac{\exp(\frac{SAm}{k_BT})}{\sum_m \exp(\frac{SAm}{k_BT})} \tag{4.84}$$

Having achieved a significant γ-ray anisotropy by cooling the sample to a low temperature $T \sim A/k_BT$, NMRON can be performed by applying an RF field and sweeping the frequency. For the dilute ^{54}Mn spins, the resonant frequencies $\nu_{m,m+1} = \Delta E_{m,m+1}/h$ corresponding to $m \rightarrow m+1$ transitions, can be selectively observed.

The dilute ^{54}Mn spins were investigated by NMRON and gave $<^{54} AS >_1 /h =$ 437.0 $\pm$ 0.2 MHz for the Mn1 site, $<^{54} AS >_2 /h =$ 480.5 $\pm$ 0.2 MHz for the Mn2 site, and $P/h = 1.2 \pm 0.1$ MHz [15].

The abundant host spins were investigated using NMR-TDNO. The beauty of combining these methods is that the effects of the Suhl-Nakamura interaction can be observed directly by comparing the NMR signals of the abundant ^{55}Mn spins, which feel the interaction, and the ^{54}Mn that do not. Thus in a 1 cm^3 crystal of ^{54}Mn-$MnCl_2{\cdot}4H_2O$ with 5 μCi activity, the separation of the ^{54}Mn atoms is $\sim 1000a$ which is much larger than the range of the interaction. Thus the line width is $\sim$ 35 kHz because there is no broadening from the Suhl-Nakamura interaction, whereas the line width of the ^{55}Mn resonance is several MHz and there is frequency pulling. In MnAc values of $(\Delta\nu/\nu)$ (Mn1) = 0.05 and $(\Delta\nu/\nu)$ (Mn2) = 0.06 were observed at $T \sim 40$ mK [15]. The expected values of 0.09 and 0.10 for the Mn1 and Mn2 spins respectively, calculated from equation 4.74, were significantly different from the measured values. It was noted that these effects would be investigated further, and this is the purpose of the present study.

4.2 Experimental Results

4.2.1 Sample preparation

Seed crystals of approximately 1 mm in length were grown from a saturated solution of MnAc by evaporation at room temperature. Unfortunately, larger crystals could not be grown by evaporation because the MnAc rapidly oxidized with the oxygen in the air, creating a brown oxide powder throughout the solution which prevented further growth. It was not possible to increase the acidity of the solution to prevent this oxidation.

To prevent oxidation, a seed crystal was placed in a groove cut in a piece of teflon, approximately 5 mm in width, as seen in figure 4.27. The goniometric data of Groth [24] was used to orient the crystal. The groove was covered with a microscope slide, sealed to the teflon with vacuum grease. Saturated MnAc solution was prepared and doped with approximately 100 μCi of ^{54}Mn. The solution was filtered to remove all the

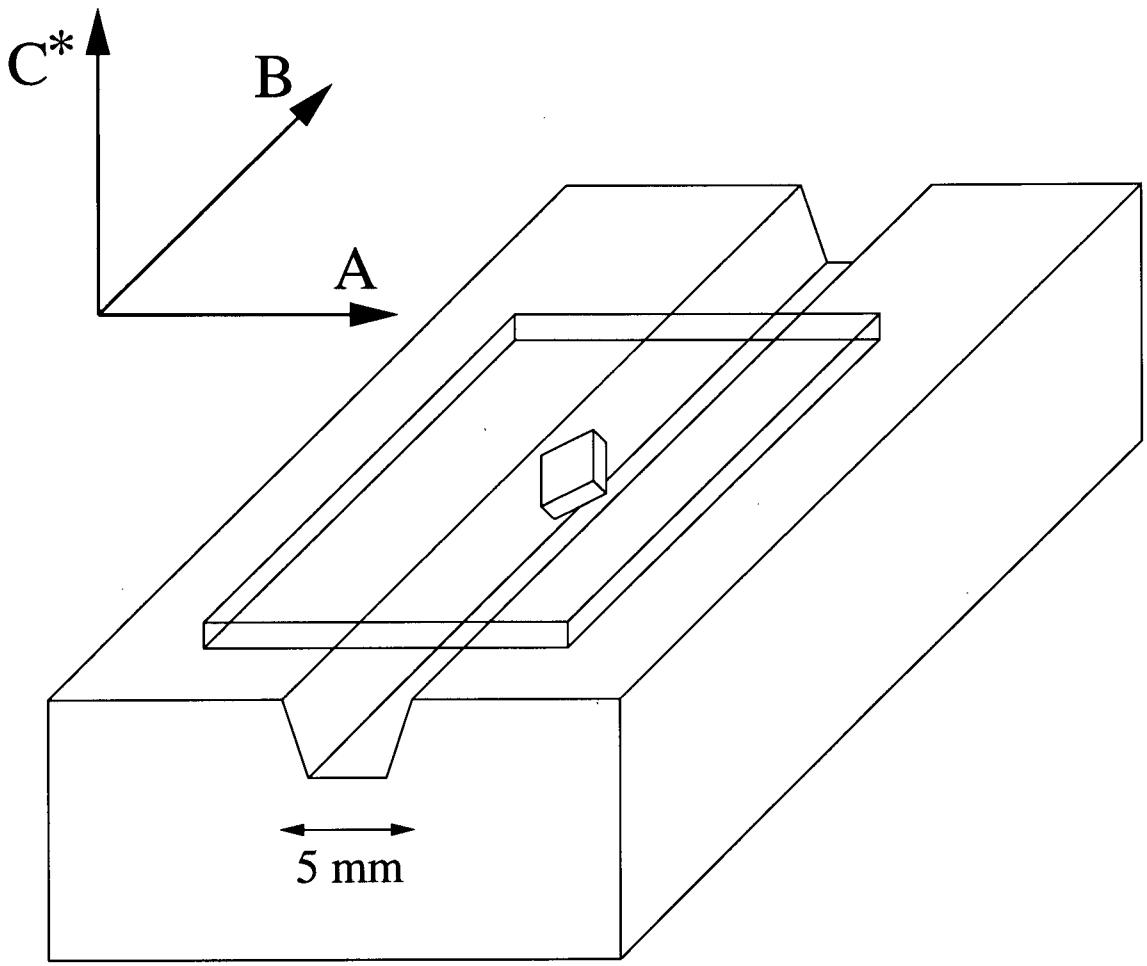

Figure 4.27: The orientation of the seed crystal in the groove cut in teflon and covered with a microscope slide in preparation for further growth with saturated solution containing some ^{54}Mn.

oxide powder and pipetted into the groove containing the seed crystal. The solution wet the microscope slide well (but not the teflon) and would run along the glass until the groove was completely filled with solution. Both ends of the groove were then sealed with vacuum grease to prevent any contact with the air.

Throughout the whole process, the solution, pipette, filter paper, teflon, microscope slide and vacuum grease were maintained at a temperature of 30° C in a feedback stabilized thermal bath controlled by a PC. Once the saturated solution surrounded the seed crystal, the temperature of the bath was lowered slowly over a period of 4 days from 30° C to 23°. It was not possible to grow a non-radioactive coating on the crystal and it had to be handled carefully. The final crystal had the orientation of the seed crystal, and an activity of approximately 1 μCi. The orientation of the crystal was verified by X-ray diffraction.

The crystal was covered with Apiezon N grease to protect it from the air, and was attached with unwaxed dental floss to the copper cold finger of a SHE dilution refrigerator, as shown in figure 4.28. A ^{60}Co in Fe thermometer was only mounted when fridge diagnostics needed to be performed because its higher energy γ-rays would otherwise contaminate the spectrum of the ^{54}Mn. Hydrated crystals deteriorate at reduced pressure at $T \geq 240$ K so the samples were precooled under an atmosphere of air.

4.2.2 Data acquisition

The NMR of the stable ^{55}Mn spins was observed utilizing the technique of NMR-TDNO [1] in which the radioactive ^{54}Mn are used as a temperature probe.

The spectra were obtained with two NaI detectors and four single channel analysers. The data was acquired from the single channel analyser output by a PC, which also controlled the RF power and frequency, and monitored the value of thermal resistors inside the cryostat.

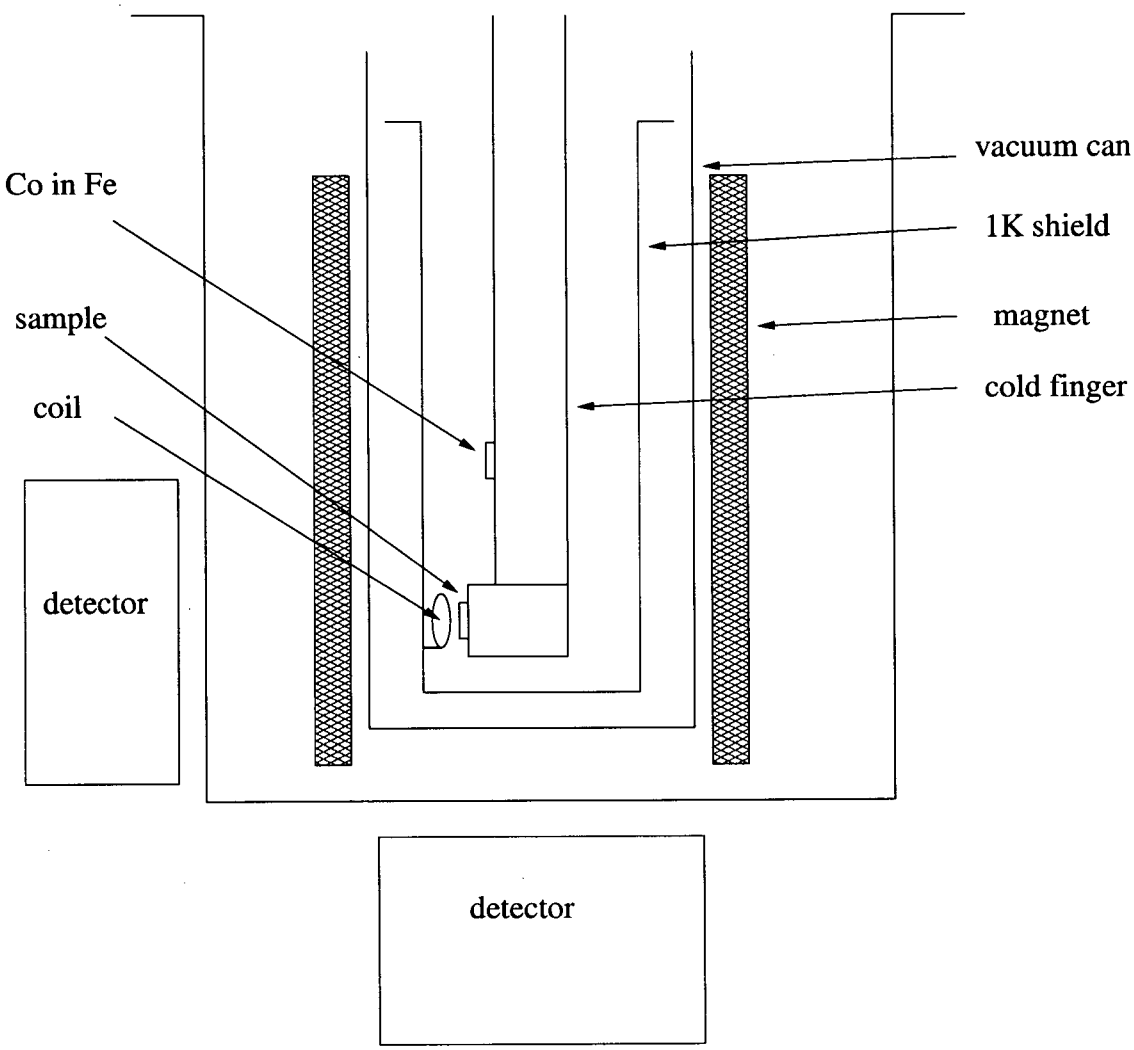

Figure 4.28: The experimental setup inside the SHE dilution refrigerator. The NaI or Ge detectors are outside the cryostat, at room temperature.

In order for NMR-TDNO to work well, the spin-lattice relaxation time, T_1, should be short compared to the dwell time of the RF frequency step and the time constant for the cooling of the sample to the cold finger. In zero field, the spin lattice relaxation times are $\sim 10^{-1}s$ [15], and the γ-ray anisotropy of the ^{54}Mn spins provides an accurate measure of the temperature of the ^{55}Mn spins. The isotropic warm counts necessary to normalize the counting rates were obtained at $T \sim 1$K.

In the previous experiment[15], only one measurement of the ^{55}Mn lines was made. The frequency step size was 1 MHz and the dwell time was 200 s. The RF power was stabilized by monitoring the temperature of the cold finger, but this has two disadvantages: first, the time constant of the feed-back loop was relatively long; second, the cold finger must undergo some warming at resonance, but the feed-back loop works to negate the effect. This stabilization procedure works well for NMRON of the dilute radioactive nuclei because there is essentially no warming, but is not well suited to the NMR-TDNO technique.

In the present experiment, the frequency was swept in 500 kHz steps with a dwell time of 100 s. The RF field was provided by the coil shown in figure 3.10. The coil inductance was $L \simeq 7 \cdot 10^{-9}$ H, the resistance was from the coil itself, the capacitor in parallel with the coil was $C_2 = 33$ pF and the capacitor in series with the coil was variable with $C_1 = 2 - 20$ pF. The series capacitor was used to tune the coil to the desired frequency. The main coil had a broad resonance centered approximately at 530 MHz at 100 mK. The RF power was monitored by a smaller, broad-band pick-up coil mounted behind the main coil, as shown in figure 3.17. The resistor values were $R_1' = R_2' = 100\ \Omega$. C' was only due to capacitive coupling between the coil and ground and was < 1 pF. A feedback loop, as shown in figure 3.16 allowed the RF power to be stabilized over the entire range of the frequency sweeps ($>$ 100MHz). This eliminated the effects of frequency dependent RF heating.

In the previous experiment the ^{55}Mn lines were observed in zero field at only one temperature and no structure was observed. Also, no measurements were performed above 600MHz.

In this experiment, the improved detection method allowed the resolution of the structure of the lines. Several spectra were obtained corresponding to different ^{55}Mn nuclear spin temperatures and these showed four peaks rather than the expected two. Two upward frequency sweeps can be seen in figure 4.29

In the thermometric method of detecting the resonances, sweeps upward and downward in frequency yield different line shapes in part due to the frequency pulling effect itself. Figure 4.30 shows three spectra at different temperatures in zero applied field, for a downward frequency sweep. The same spectra were observed in applied fields up to 110 mT. In Figure 4.30 the frequency pulling effect can be clearly observed.

4.2.3 Data analysis

In order to estimate the line positions as a function of temperature, the peaks were fitted by assuming a Gaussian line-shape and an exponential relaxation to the temperature of the dilution refrigerator. The change in anisotropy at frequency ω is then given by

$$\frac{dW(0)}{dt} = \sum_{i=1}^{4} A_i \int_{-\phi_0}^{\phi_0} \exp\left(\frac{(\omega+\phi-\omega_i)^2}{\sigma_i^2}\right) d\phi + \frac{W_0(0)-W(0)}{\tau} \qquad (4.85)$$

where the first term corresponds to the four resonance lines, and the second term is the relaxation to the base anisotropy, $W_0(0)$. ϕ_0 is the modulation, τ is the relaxation time, and the A_i, ω_i and σ_i are the amplitudes, positions and widths of the four resonance lines. The starting anisotropy was taken to be the average of the first five data points. $W(0)$ was then calculated by integrating equation 4.85 with respect to t and a χ^2 was calculated and minimized with MINUIT. The free parameters were A_i, ω_i, σ_i, τ and $W_0(0)$. $W_0(0)$ was not necessarily equal to the starting anisotropy because turning on the RF power

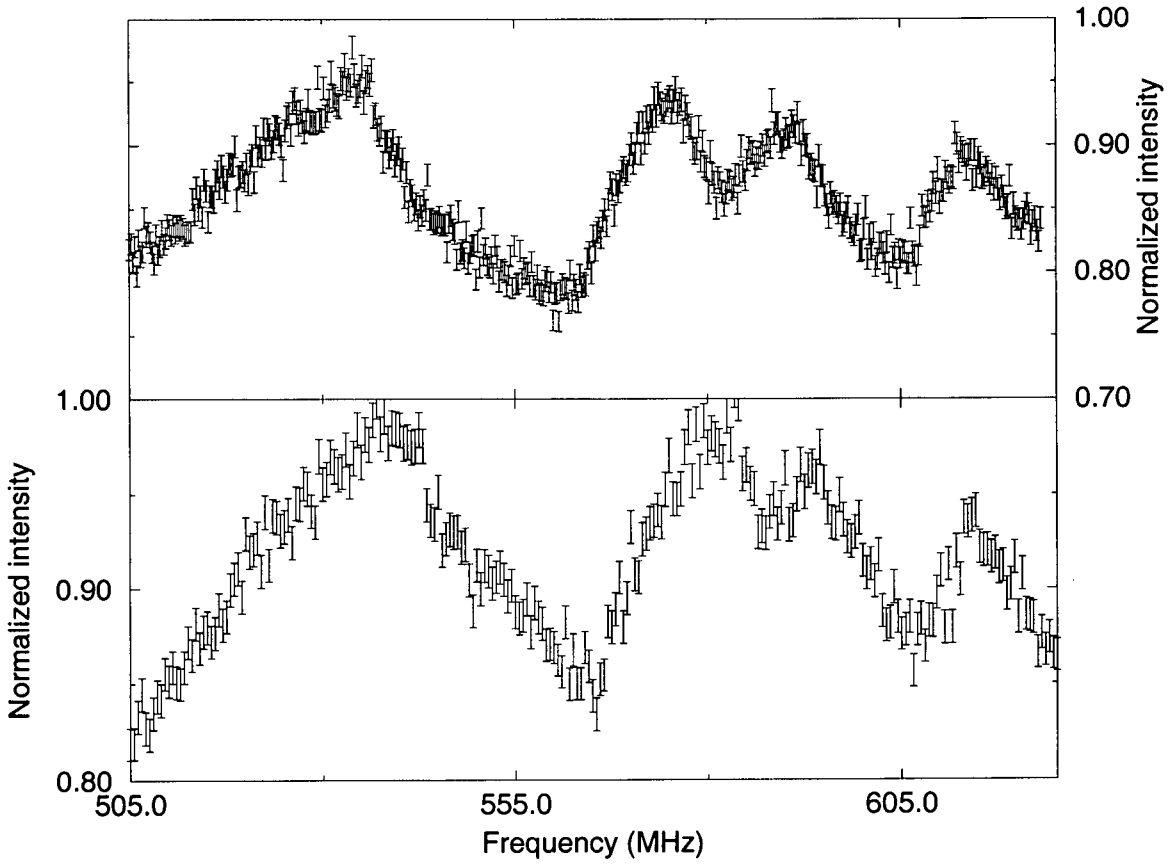

Figure 4.29: Two frequency spectra showing four resonance lines in zero applied field. The frequency was swept upwards. Although the temperature varies throughout the sweep, the lower line is in general warmer than the upper line and consequently experiences less frequency pulling. The unpulled resonant frequencies are 551.8 MHz for the Mn1 spins and 606.7 MHz for the Mn2 spins.

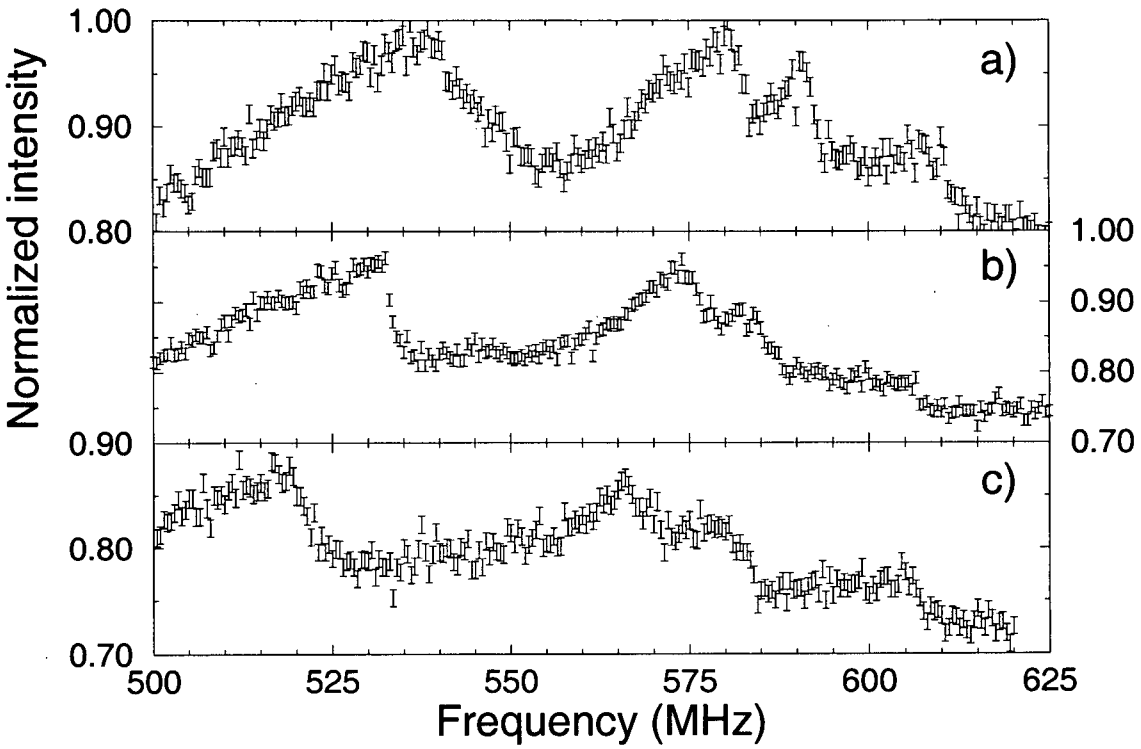

Figure 4.30: A comparison of 3 spectra. Although the temperature of the sample varies throughout the frequency sweep (from about 30 mK to over 100 mK), in general $T_a > T_b > T_c$ and the frequency pulling can be clearly seen. The frequency was swept downwards.

did affect the base temperature of the crystal through non-resonant warming of the cold finger. An example of a fit can be seen in figure 4.31. Although the relaxation processes,

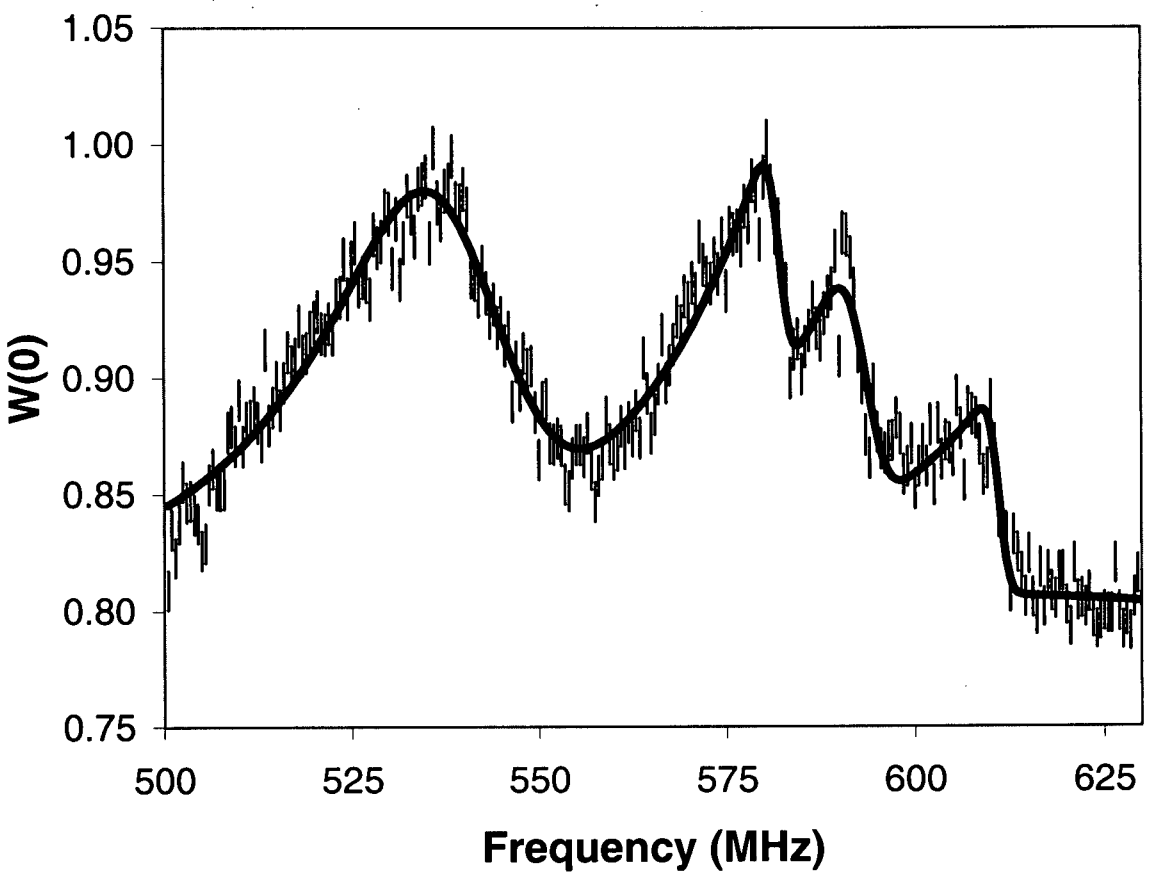

Figure 4.31: An example of the power spectrum with a best fit line. The frequency was swept downwards. At the start of the sweep the temperature is approximately 35 mK. When $W(0)$ approaches 1, the temperature is over 100 mK.

and the power absorption are more complicated than the assumptions of the model, the goal was to find a position of the lines as a function of temperature and this is clearly achieved. The width of the lines (σ_i) are used as the error in line position and the temperature was measured by averaging ten counts immediately before the start of the each peak. The position of the lines as a function of temperature are plotted in figure 4.32. In order to fit the data exactly, a theoretical model of the entire power spectrum

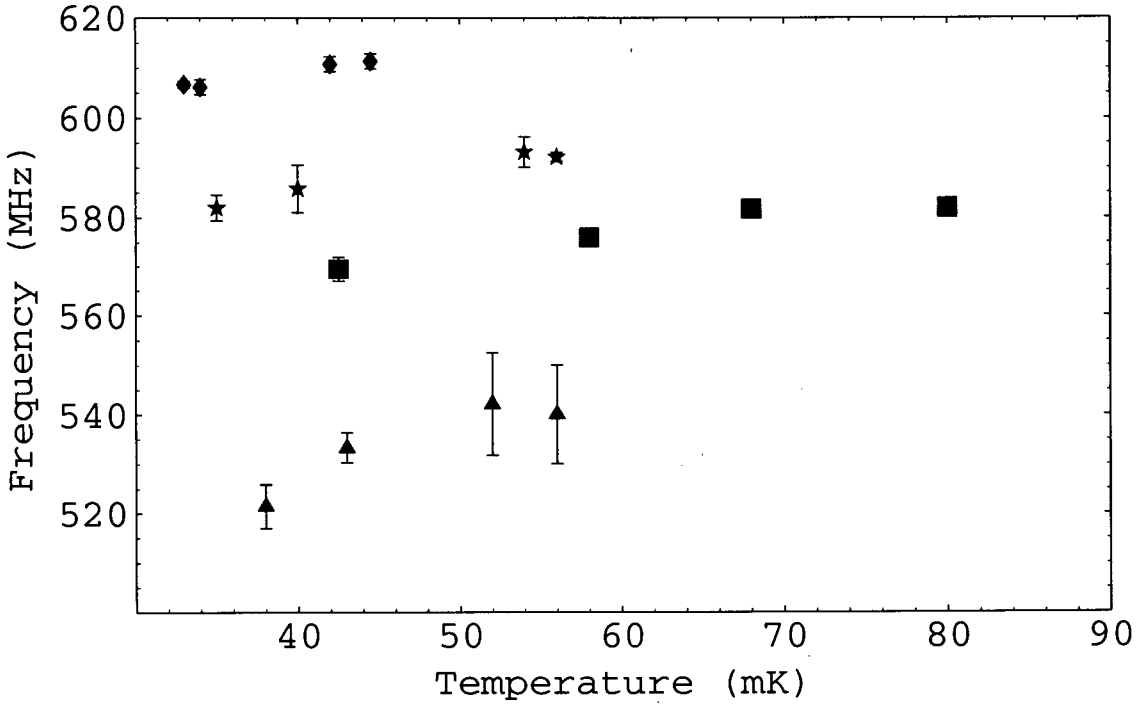

Figure 4.32: The position of each of the four resonant lines as a function of temperature.

as a function of temperature would be necessary. However, the Gaussian fit gives a very reasonable estimate, within the given error, of the position of the line as a function of temperature.

4.3 Conclusion

The simple model of the Suhl-Nakamura interaction for the case $I = 1/2$ with uniaxial anisotropy and a single ion per lattice site is clearly insufficient to explain the observed spectra. To the best knowledge of the author, the Suhl-Nakamura interaction with $I > 1/2$ has not been considered. When $I > 1/2$ the self interaction term (U_{ii}) cannot be neglected. When there is non-uniaxial anisotropy, the electronic magnon gap, which determines the overall amplitude of the frequency pulling needs to be calculated by a Bogliubov transformation. Finally, when there is a triplet of ions at each lattice site, the

interactions between the spins cannot be ignored, and will modify the frequency pulling. In the following chapter, a model is developed which takes all of these important effects into account.

Chapter 5

The general Suhl-Nakamura interaction: a basis of spins, $I \geq 1/2$ and non-uniaxial anisotropy

5.1 Introduction

As mentioned in the previous chapter, to the best of our knowledge, the Suhl-Nakamura interaction for $I > 1/2$ has not been rigorously dealt with theoretically. Therefore we have developed a theoretical model for this case in which the self-interaction term is important. The case of non-uniaxial crystal field anisotropy is also considered and it is shown to have an extremely important effect on the frequency pulling.

The frequency pulling is calculated for a triplet of spins and compared to the experimental data. Furthermore, the $T = 0$ spectrum of excitations is calculated by spin wave theory. The effects of the Mn1 spins on Mn2 spins and vice-versa is found to be important. A number of mechanisms which could explain the four observed lines are considered.

The linewidth is calculated in the case of a single spin per lattice site down to $T = 0$ and compared to a high temperature expansion previously calculated. The results agree well at the temperatures where the high temperature expansion is valid. However, our calculation also includes the effects of the self-interaction on the linewidth, and is valid as $T \to 0$.

The exact power spectrum involving 1 to 4 spins is calculated numerically at a variety of temperatures and classical simulations of a crystal of 15×15 spins are performed. The

results qualitatively confirm the predictions of our model.

5.2 The electronic magnon spectrum

The strong coupling between the three electronic spins forming a triplet allows us to treat the latter as an effective $S = 5/2$ single spin, ferromagnetically coupled to its neighbours in the a-b plane. We can also ignore the magnetic interactions between different layers and treat the system as a 2-D ferromagnet. With these approximations, all triplets in the a-b plane are equivalent in terms of their magnetic interactions. The magnetic anisotropy in this system is not uniaxial. The easy axis is the a-axis, $B_A^b = 0.14$ T and $B_A^c = 0.86$ T) [20]. The z-direction is chosen along the a-axis, and the x and y directions are chosen to be the b and c* axes respectively.

Two of the sites within the triplet of spins are equivalent and are denoted as Mn2, while the other site is Mn1.

The electronic magnon gap can be calculated from the electronic spin Hamiltonian

$$H = J_F \sum_{<nn>} \vec{S}_i \cdot \vec{S}_j + \sum_i g\mu_B \left(\frac{B_A^b}{2S}(S_i^x)^2 + \frac{B_A^c}{2S}(S_i^y)^2 - S_i^z B_0 \right) \tag{5.86}$$

A standard Holstein-Primakoff transformation can be used, ($S^z = S - a^\dagger a$, $S^+ \simeq \sqrt{2S}a$, $S^- \simeq \sqrt{2S}a^\dagger$) and is expected to give good results because the spin is large ($S = 5/2$) and the temperature is low compared to the coupling between electronic spins (the Curie temperature is $\sim$ 3 K while we are working at $T < 100$ mK. Working in momentum space,

$$a_{\vec{k}} = \frac{1}{\sqrt{N}} \sum_j a_j e^{i\vec{k}\cdot\vec{R}_j}. \tag{5.87}$$

the Hamiltonian can be written as

$$H - E_0 = \sum_{\vec{k}} \left(\Omega_0(\vec{k}) a_{\vec{k}}^\dagger a_{\vec{k}} + g\mu_B \frac{B_A^-}{2}(a_{\vec{k}} a_{-\vec{k}} + a_{\vec{k}}^\dagger a_{-\vec{k}}^\dagger) \right) \tag{5.88}$$

where E_0 is the ground state energy,

$$\Omega_0(\vec{k}) = S|J|\left(n - \sum_{i=1}^{n}\cos(\vec{k}\cdot\vec{\delta}_i)\right) + g\mu_B(B_A^+ + B_0), \tag{5.89}$$

$B_A^{\pm} = (B_A^b \pm B_A^c)/2$, n is the number of nearest neighbours (4 in the case of MnAc) and $\vec{\delta}_i$ is the position of the ith nearest neighbour. The reciprocal lattice can be divided into two sections which will be referred to as $\pm k$, and the Hamiltonian can be written in the following matrix form

$$H - E_0 = \sum_{+\vec{k}} \begin{pmatrix} a_{+k}^\dagger & a_{-k} \end{pmatrix} M \begin{pmatrix} a_{+k} \\ a_{-k}^\dagger \end{pmatrix} \tag{5.90}$$

where

$$M = \begin{pmatrix} \Omega_0(+k) & g\mu_B B_A^- \\ g\mu_B B_A^- & \Omega_0(-k) \end{pmatrix} \tag{5.91}$$

A Bogliubov transformation can be performed by diagonalizing the matrix M in the metric

$$\eta = \begin{pmatrix} -1 & 0 \\ 0 & 1 \end{pmatrix} \tag{5.92}$$

It is necessary to diagonalize in this metric to preserve the proper commutation relation of the new fields, which should themselves be bosonic creation and annihilation operators. The unit vectors of our space are a_k and $a_{-k}^\dagger$, and we define the scalar product between two unit vectors, α and β to be $\alpha\cdot\beta = [\alpha^\dagger, \beta]$. This definition of the scalar product gives our space the metric η. If we diagonalize M with η as the metric, the eigenvectors are orthogonal in that metric, and the new operators will obey all the correct commutation relations.

The eigenvectors can be found by solving

$$M\Phi_i = \varepsilon_i \eta \Phi_i. \tag{5.93}$$

Since $\eta^2 = 1$, we can solve $\eta M\Phi = \varepsilon\Phi$. The eigenvectors corresponding to positive eigenvalues can be normed such that $\Phi_i^\dagger \eta \Phi_i = 1$, the negative eigenvalues such that $\Phi_j^\dagger \eta \Phi_j = -1$, and $\Phi_i^\dagger \eta \Phi_j = 0$ for any $i \neq j$. If B is the matrix where each column is an eigenvector, then the orthogonality relations can be written as

$$B^\dagger \eta B = \eta \tag{5.94}$$

and $B^\dagger M B$ is diagonal, and all the terms are positive, since equation 5.93 can be rewritten as

$$M_{jk} B_{km} = \varepsilon_m \eta_{jq} B_{qm} \tag{5.95}$$

and, multiplying by $B^\dagger$, we have

$$\begin{aligned} B_{ij}^\dagger M_{jk} B_{km} &= \varepsilon_m B_{ij}^\dagger \eta_{jq} B_{qm} \\ &= \varepsilon_m \eta_{im} \end{aligned} \tag{5.96}$$

For a more complete discussion of diagonalization of bosonic and fermionic annihilation and creation operators Hamiltonians, see [25].

If we pose

$$\begin{pmatrix} a_k \\ a_{-k}^\dagger \end{pmatrix} = B\varphi \begin{pmatrix} \alpha_k \\ \alpha_{-k}^\dagger \end{pmatrix} \tag{5.97}$$

where

$$\varphi = \begin{pmatrix} e^{i\phi_1} & 0 \\ 0 & e^{i\phi_2} \end{pmatrix} \tag{5.98}$$

then H is diagonal in terms of the operators α_k and α_{-k}. The phases of the fields $\alpha_{\pm k}$ and $a_{\pm k}$ are arbitrary. Using equation 5.94, we have

$$\begin{pmatrix} \alpha_k \\ \alpha_{-k}^\dagger \end{pmatrix} = \varphi^\dagger \eta B^\dagger \eta \begin{pmatrix} a_k \\ a_{-k}^\dagger \end{pmatrix} \tag{5.99}$$

The Bogliubov transformation leads to the following electronic magnon spectrum

$$\omega_{\vec{k}} = \sqrt{\Omega_0^2(\vec{k}) - (g\mu_B B_A^-)^2} \tag{5.100}$$

and an electronic magnon gap of 0.35 T.

With a convenient choice of the phases ϕ_1 and ϕ_2, the new fields are

$$\begin{pmatrix} \alpha_k \\ \alpha_{-k}^\dagger \end{pmatrix} = \begin{pmatrix} u_k & -v_k \\ -v_k & u_k \end{pmatrix} \begin{pmatrix} a_k \\ a_{-k}^\dagger \end{pmatrix} \tag{5.101}$$

where

$$\begin{aligned} u_k &= \frac{\Omega_0(k) + \omega(k)}{\sqrt{2\omega(k)(\omega(k) + \Omega_0(k))}} \\ v_k &= \frac{-g\mu_B B_A^-}{\sqrt{2\omega(k)(\omega(k) + \Omega_0(k))}} \\ -u_k v_k &= \frac{-g\mu_B B_A^-}{2\omega(k)} \\ u_k^2 + v_k^2 &= \frac{\Omega_0(k)}{\omega(k)} \\ u_k^2 - v_k^2 &= 1 \end{aligned} \tag{5.102}$$

Typical values of the parameters give $u_k = 1.105$ and $v_k = -0.470$ when $k \to 0$. Plots of u_k and $|v_k|$ over the first Brillouin zone are shown in figures 5.33 and 5.34.

5.3 The Suhl-Nakamura interaction between nuclear spins

The Suhl-Nakamura interaction can be calculated for the MnAc crystal, with the assumption that the electronic spins in a triplet behave as a single, $S = 5/2$ spin coupled to each of the three nuclear spins. If we introduce the operator

$$\vec{\Lambda}_j = \mathbf{A_1}\vec{I}_j + \mathbf{A_2}(\vec{I}_{a,j} + \vec{I}_{b,j}) \tag{5.103}$$

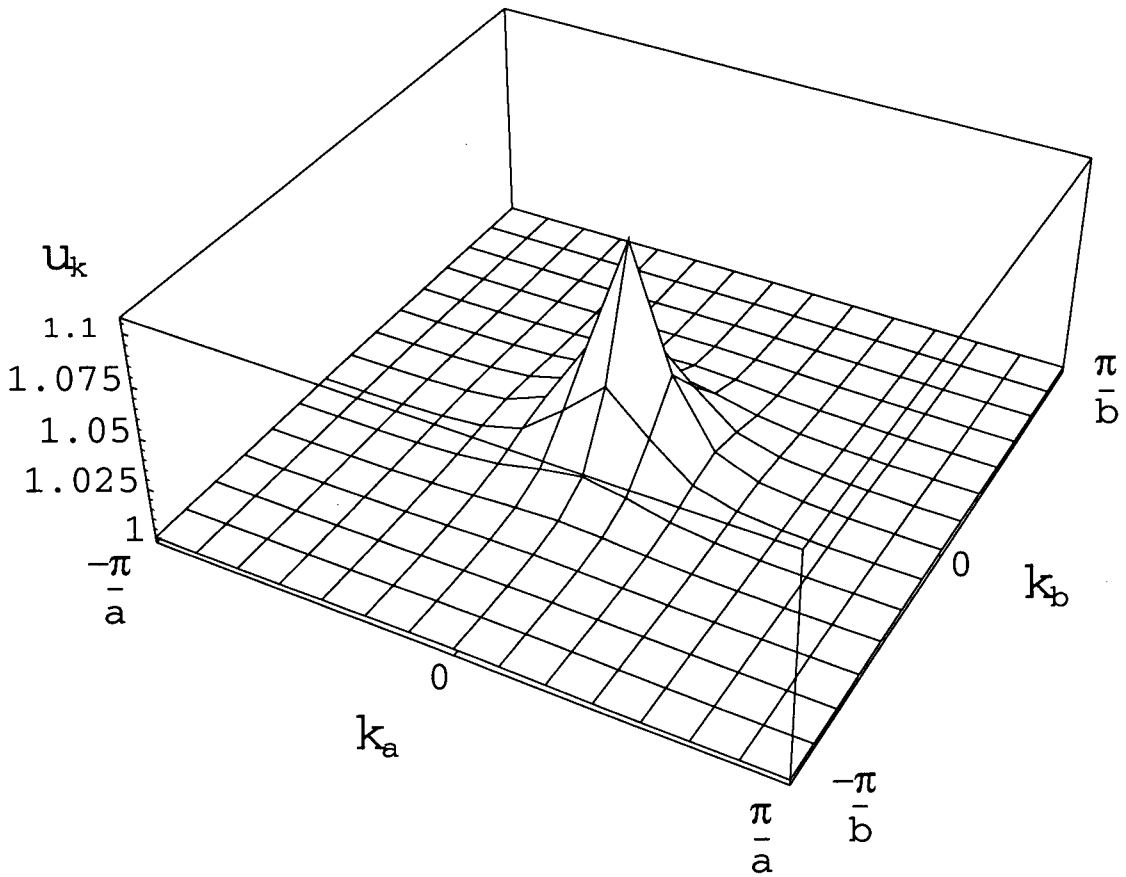

Figure 5.33: The value u_k over the first Brillouin zone. Note that u_k is only different from unity near $k = 0$. The graph is calculated with $J/k_B = 0.456$ K, $B_A^c = 0.14$ T and $B_A^b = 0.86$ T.

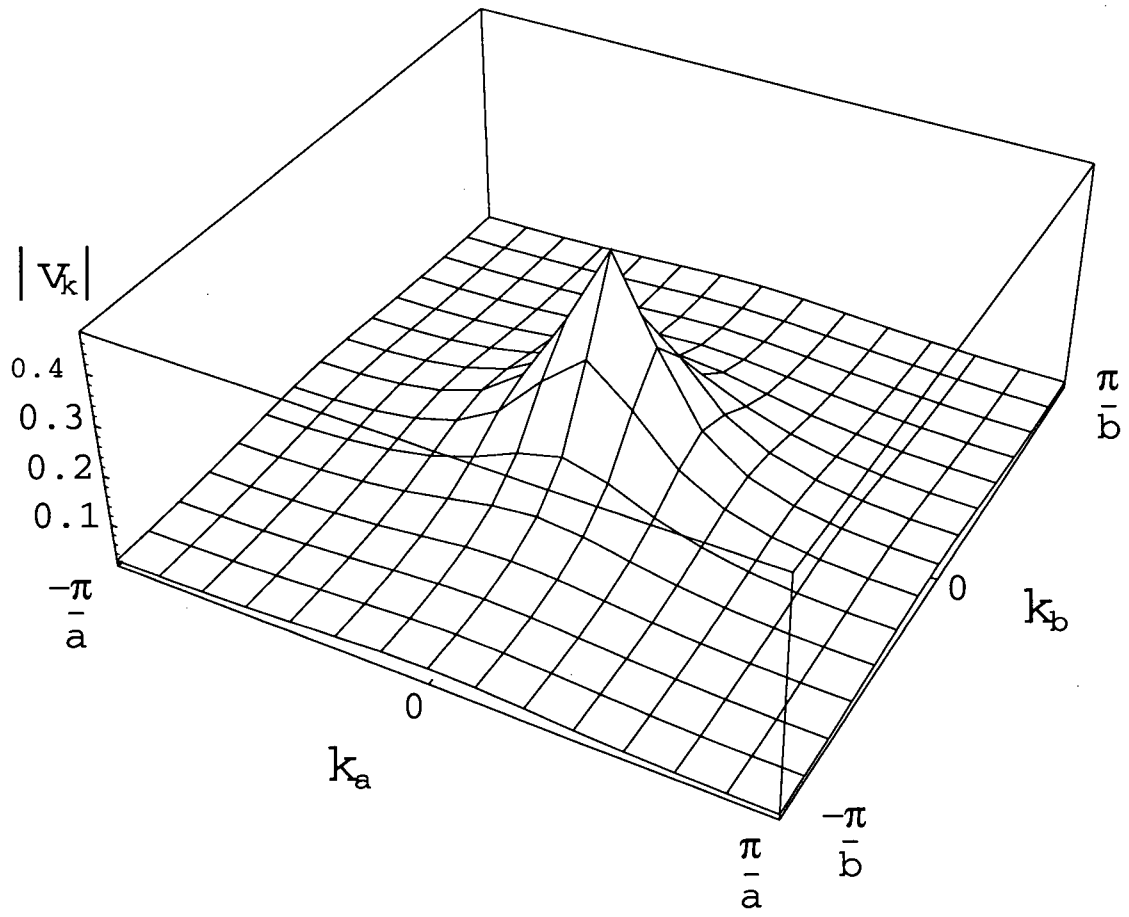

Figure 5.34: The value $|v_k|$ over the first Brillouin zone. Note that v_k is only different from zero near $k = 0$. The graph is calculated with $J/k_B = 0.456$ K, $B_A^c = 0.14$ T and $B_A^b = 0.86$ T.

where $\mathbf{A_1}$ and $\mathbf{A_2}$ are the effective hyperfine coupling tensors of the sites 1 and 2 and the indices a and b refer to the two equivalent Mn2 sites, then the hyperfine Hamiltonian can be expressed as

$$H_{HF} = \sum_j \vec{\Lambda}_j \cdot \vec{S} = \sum_j \left(\Lambda_j^z S_j^z + \frac{1}{2}(\Lambda_j^+ S_j^- + \Lambda_j^- S_j^+) \right) \tag{5.104}$$

where $\Lambda_j^{\pm} = \Lambda_j^x \pm i\Lambda_j^y$.

We can use the Holstein-Primakoff transformation, introduced above, to rewrite the electronic spins in terms of annihilation and creation operators. Ignoring constant terms, and working in momentum space, the hyperfine Hamiltonian becomes

$$H_{HF} = S\sum_j \Lambda_j^z - \frac{1}{N}\sum_{j,k,k'} \Lambda_j^z a_k^+ a_k e^{i(k-k')R_j} + \sqrt{\frac{S}{2N}} \sum_{j,k} \left(\Lambda_j^- a_k^\dagger e^{-ikR_j} + \Lambda_j^+ a_k e^{ikR_j} \right) \tag{5.105}$$

Finally, we can introduce the operators α_k and $\alpha_{-k}^\dagger$. The Hamiltonian $H = H_0 + H'$ becomes

$$H_0 = S\sum_j \Lambda_j^z + \sum_k \omega_k \alpha_k^\dagger \alpha_k \tag{5.106}$$

$$\begin{aligned} H' = & -\frac{1}{N}\sum_{j,k,k'} \Lambda_j^z \left(u_k u_{k'} \alpha_k^\dagger \alpha_{k'} + v_k v_{k'} \alpha_{-k'}^\dagger \alpha_{-k} + u_k v_{k'} \alpha_k^\dagger \alpha_{-k'}^\dagger + u_{k'} v_k \alpha_{k'} \alpha_{-k} \right) e^{i(k-k')R_j} \\ & + \sqrt{\frac{S}{2N}} \sum_{j,k} \left(\Lambda_j^- (u_k \alpha_k^\dagger + v_k \alpha_{-k}) e^{-ikR_j} + \Lambda_j^+ (u_k \alpha_k + v_k \alpha_{-k}^\dagger) e^{ikR_j} \right) \end{aligned} \tag{5.107}$$

If we consider H' as a perturbation of H_0, we can calculate the correction to the energy for a state $|\Psi> = |\psi_0 \phi>$ where $|\psi_{n,k_1,...,k_n}>$ is the electronic state with n magnons of wave vector $k_1, ..., k_n$, and $|\phi>$ is an arbitrary nuclear state. Clearly, there is no first order correction to the energy. To second order, only terms with one or two electronic magnons contribute. Since $\omega_k \gg E_\Phi$

$$\Delta E^{(2)} = -\sum_{\phi',n,k1,...,k_n} \frac{|<\psi_{0,k}\phi|H'|\psi_{n,k_1,...,k_n}\phi>|^2}{\omega_{k1} + ... + \omega_{k_n} + E_{\phi'} - E_\phi}$$

$$\simeq \frac{1}{N^2}\sum_{\phi',k_1,k_2}\frac{e^{-i(k_1+k_2)(R_j-R_{j'})}}{\omega_{k_1}+\omega_{k_2}}(u_{k_1}v_{k_2}+u_{k_2}v_{k_1})^2 < \phi|\Lambda_j^z|\phi' >< \phi'|\Lambda_{j'}^z|\phi >$$
$$-\frac{S}{2N}\sum_{\phi',k,j,j'}\frac{e^{ik(R_j-R_{j'})}}{\omega_k}\Big(< \phi|\Lambda_j^-|\phi' >< \phi'|\Lambda_{j'}^-|\phi > u_kv_k$$
$$+ < \phi|\Lambda_j^+|\phi' >< \phi'|\Lambda_{j'}^-|\phi > u_k^2 + < \phi|\Lambda_j^-|\phi' >< \phi'|\Lambda_{j'}^+|\phi > v_k^2$$
$$+ < \phi|\Lambda_j^+|\phi' >< \phi'|\Lambda_{j'}^+|\phi > u_kv_k\Big) \quad (5.108)$$

Using $\sum_{\phi'}|\phi' >< \phi'| = 1$, this expression is equivalent to the diagonal matrix elements of an effective nuclear Hamiltonian

$$H_{eff} = \frac{1}{2}\sum_{j,j'}\left(U_{jj'}^{++}(\Lambda_j^-\Lambda_{j'}^- + \Lambda_j^+\Lambda_{j'}^+) + U_{jj'}^{+-}\Lambda_j^+\Lambda_{j'}^- + U_{jj'}^{-+}\Lambda_j^-\Lambda_{j'}^+ + 2U_{jj'}^z\Lambda_j^z\Lambda_{j'}^z\right) \quad (5.109)$$

with

$$\begin{aligned}
U_{jj'}^{++} &= -\frac{S}{N}\sum_k\frac{u_kv_ke^{ik(R_j-R_{j'})}}{\omega_k}\\
U_{jj'}^{+-} &= -\frac{S}{N}\sum_k\frac{u_k^2e^{ik(R_j-R_{j'})}}{\omega_k}\\
U_{jj'}^{-+} &= -\frac{S}{N}\sum_k\frac{v_k^2e^{ik(R_j-R_{j'})}}{\omega_k}\\
U_{jj'}^{z} &= -\frac{1}{N^2}\sum_{k_1,k_2}\frac{(u_{k_1}v_{k_2}+u_{k_2}v_{k_1})^2e^{-i(k_1+k_2)(R_j-R_{j'})}}{\omega_{k_1}+\omega_{k_2}}
\end{aligned} \quad (5.110)$$

5.3.1 The pseudoquadrupolar interaction

We can first consider the pseudoquadrupolar interaction, for ^{54}Mn. In this case, there is no coupling between nuclear spins because the spins are so dilute. Using $I^+I^- = I(I+1)-(I^z)^2+I^z$, and assuming an isotropic hyperfine interaction A, the Hamiltonian for each spin (1 or 2) reduces to

$$\begin{aligned}
H &= AI^z + \frac{A^2}{2}\Big(\Big(I(I+1)-(I^z)^2\Big)(U_{ii}^{+-}+U_{ii}^{-+}) + I^z(U_{ii}^{+-}-U_{ii}^{-+})\\
&\quad + U_{ii}^{++}(I^+I^+ + I^-I^-) + 2U_{ii}^z(I^z)^2\Big)
\end{aligned} \quad (5.111)$$

Using equations 5.102 and 5.110, all the terms can be calculated numerically. Since $\vec{k} = x\vec{b_1} + y\vec{b_2}$ where $x = n/N_1$ and $y = m/N_2$ and $\vec{b_i} \cdot \vec{a_i} = 2\pi\delta_{ij}$ it follows that

$$\frac{1}{N}\sum_{\vec{k}} f(\vec{k_1}\cdot\vec{a_1}, \vec{k_2}\cdot\vec{a_2}) = \int_{-1/2}^{1/2}\int_{-1/2}^{1/2} dx\, dy\, f(2\pi x, 2\pi y) \tag{5.112}$$

Considering equations 5.102, it is clear that $U_{ii}^{+-} \gg U_{ii}^{--}$, $U_{ii}^{+-} \gg U_{ii}^{++}$ and $U_{ii}^{+-} \gg U_{ii}^{z}$ because $u_k \gg v_k$ except for a small region near $k = 0$. This conclusion is supported by the numerical results because, for $J = 0.456K$, $B_0 = 0$, $B_A^c = 0.14T$, $B_A^b = 0.86T$, we find

$$\begin{aligned} U_{ii}^{+-}/h &= -3.4\cdot 10^{-5}\mathrm{MHz}^{-1} \\ U_{ii}^{--}/h &= -8.9\cdot 10^{-7}\mathrm{MHz}^{-1} \\ U_{ii}^{++}/h &= 4.2\cdot 10^{-6}\mathrm{MHz}^{-1} \\ U_{ii}^{z}/h &= -2.2\cdot 10^{-7}\mathrm{MHz}^{-1} \end{aligned} \tag{5.113}$$

Consequently, equation 5.111 reduces to

$$H = AI^z + \frac{A^2}{2}\left(I(I+1) - (I^z)^2 + I^z\right)U_{ii}^{+-} \tag{5.114}$$

The difference in energy between levels m and $m+1$ is given by

$$h\nu_{m,m+1} = A - mA^2U_{ii}^{+-} \tag{5.115}$$

We can compare to values measured for ^{54}Mn [15] where, in $B_0 = 0.2$ T, the value of $-(A_1^{54})^2U_{ii}^{+-}/h$ for the Mn2 site is found to be 1.2 MHz. The mean field Curie temperature for a Heisenberg Hamiltonian is given by [26]

$$k_BT_c^{mf} = \frac{4}{3}S(S+1)J \tag{5.116}$$

Our magnetic system is a Hamiltonian with nearest neighbour coupling (equivalent to a square lattice model since J is the same for all 4 nearest neighbours). From the exact

2 dimensional square lattice result for an Ising, nearest neighbour model, we know that $T_c/T_c^{mf} = 0.567$ [27]. Since $T_c = 3.19$K for MnAc, we can predict that $J/k_B \simeq 0.456$ K. Using $B_A^c = 0.14$ T, $B_A^b = 0.86$ T, $B_0 = 0.2$ T and $J/k_B = 0.456$ K, we find that $-(A_1^{54})^2 U_{ii}^{+-} = 1.1$ MHz, which compares very well with the experimental result of 1.2 MHz.

5.3.2 The interaction for the host spins

In the case of the abundant ^{55}Mn spins, the interaction between neighbouring spins cannot be ignored. The equations of motion for $I_{\alpha,j}^{\pm}$, where α denotes the Mn1 or Mn2 site ($\alpha = 1, 2$), are given by

$$\frac{dI_{\alpha,j}^{\pm}}{dt} = i[H, I_{\alpha,j}^{\pm}] \tag{5.117}$$

This leads to

$$\begin{aligned} -i\frac{dI_{\alpha,j}^{+}}{dt} &= \left(SA_\alpha + A_\alpha^2 U_{ll}^{+-} + 2A_\alpha^2 U_{ll}^{z}(I_{\alpha,i}^{z} - 1) + 2A_\alpha \sum_j U_{ij}^{z}\Lambda_j^{z} \right) I_{\alpha,i}^{+} - 2A_\alpha I_{\alpha,i}^{z} \sum_j U_{ji}^{++}\Lambda_j^{-} \\ &\quad -A_\alpha I_{\alpha,i}^{z} \sum_j (U_{ji}^{+-} + U_{ij}^{-+})\Lambda_j^{+} - 2A_\alpha^2 U_{ll}^{++}(I_{\alpha,i}^{z} + 1) I_{\alpha,i}^{-} \end{aligned} \tag{5.118}$$

and

$$\begin{aligned} i\frac{dI_{\alpha,j}^{-}}{dt} &= \left(SA_\alpha - A_\alpha^2 U_{ll}^{-+} + 2A_\alpha^2 U_{ll}^{z}(I_{\alpha,i}^{z} + 1) + 2A_\alpha \sum_j U_{ij}^{z}\Lambda_j^{z} \right) I_{\alpha,i}^{-} - 2A_\alpha I_{\alpha,i}^{z} \sum_j U_{ji}^{++}\Lambda_j^{+} \\ &\quad -A_\alpha I_{\alpha,i}^{z} \sum_j (U_{ji}^{+-} + U_{ij}^{-+})\Lambda_j^{-} - 2A_\alpha^2 U_{ll}^{++}(I_{\alpha,i}^{z} - 1) I_{\alpha,i}^{+} \end{aligned} \tag{5.119}$$

We can linearize these equations by replacing $I_{\alpha,j}^{z}$ with its thermodynamic average $< I_\alpha^z >$. The thermodynamic average of an operator O is defined as

$$< O >= \frac{Tr\left[e^{-\beta H} O\right]}{Tr\left[e^{-\beta H}\right]} \tag{5.120}$$

where $\beta = 1/k_b T$. This approximation leaves an indeterminacy in the equations because $< I_\alpha^z >$ is a c-number and the commutation relations with $I_{\alpha,j}^{\pm}$ are lost. However, as we

shall see, the terms are small enough to be neglected. If we write the equations in Fourier space, using

$$\begin{aligned} I^+_{\alpha,k} &= \frac{1}{\sqrt{N}}\sum_j e^{ikR_j} I^+_j \\ I^-_{\alpha,k} &= \frac{1}{\sqrt{N}}\sum_j e^{-ikR_j} I^-_j \\ I^z_{\alpha,k} &= \frac{1}{\sqrt{N}}\sum_j e^{ikR_j} I^z_j \end{aligned} \tag{5.121}$$

then equations 5.118 and 5.119 become

$$\begin{aligned} -i\frac{dI^+_{\alpha,k}}{dt} &= \left(SA_\alpha + A^2_\alpha U^{+-}_{ll} + 2A^2_\alpha U^z_{ll}(< I^z_\alpha > -1) + -4A_\alpha U_z < \Lambda^z >\right) I^+_{\alpha,k} \\ &\quad +2A_\alpha S < I^z_\alpha > \frac{u_k v_k}{w_k}\Lambda^-_{-k} + SA_\alpha < I^z_\alpha > \frac{u^2_k + v^2_k}{w_k}\Lambda^+_k \\ &\quad -2A^2_\alpha U^{++}_{ll}(< I^z_\alpha > +1) I^-_{\alpha,-k} \end{aligned} \tag{5.122}$$

and

$$\begin{aligned} i\frac{dI^-_{\alpha,k}}{dt} &= \left(SA_\alpha - A^2_\alpha U^{-+}_{ll} + 2A^2_\alpha U^z_{ll}(< I^z_\alpha > +1) + -4A_\alpha U_z < \Lambda^z >\right) I^-_{\alpha,k} \\ &\quad +2A_\alpha S < I^z_\alpha > \frac{u_k v_k}{w_k}\Lambda^+_{-k} + SA_\alpha < I^z_\alpha > \frac{u^2_k + v^2_k}{w_k}\Lambda^-_k \\ &\quad -2A^2_\alpha U^{++}_{ll}(< I^z_\alpha > -1) I^+_{\alpha,-k} \end{aligned} \tag{5.123}$$

where

$$U_z = \frac{1}{N}\sum_k \frac{(u_k v_k)^2}{w_k} \tag{5.124}$$

The numerical results shown in equation 5.113 show that we can ignore all the terms involving U^{-+}_{ll},U^{++}_{ll} and U^z_{ll}. Finally, the term involving U^{+-}_{ll} only leads to a renormalization of the unpulled frequency. Since $A^2_\alpha U^{+-}_{ll} \sim 2$ MHz in $B_0 = 0$ and $SA^2_\alpha \sim 600$

MHz, we will ignore this term as well. Finally, we have

$$-i\frac{d}{dt}\begin{pmatrix} I_k^+ \\ I_{a,k}^+ \\ I_{b,k}^+ \\ I_{-k}^- \\ I_{a,-k}^- \\ I_{b,-k}^- \end{pmatrix} = G_k(T)\begin{pmatrix} I_k^+ \\ I_{a,k}^+ \\ I_{b,k}^+ \\ I_{-k}^- \\ I_{a,-k}^- \\ I_{b,-k}^- \end{pmatrix} \tag{5.125}$$

where the indices a and b refer to the two Mn2 sites,

$$G_k(T) = \begin{pmatrix} \alpha_1+\beta_1 & \alpha_{12} & \alpha_{12} & \delta_{11} & \delta_{12} & \delta_{12} \\ \alpha_{21} & \alpha_2+\beta_2 & \alpha_{22} & \delta_{21} & \delta_{22} & \delta_{22} \\ \alpha_{21} & \alpha_{22} & \alpha_2+\beta_2 & \delta_{21} & \delta_{22} & \delta_{22} \\ -\delta_{11} & -\delta_{12} & -\delta_{12} & -\alpha_1-\beta_1 & -\alpha_{12} & -\alpha_{12} \\ -\delta_{21} & -\delta_{22} & -\delta_{22} & -\alpha_{21} & -\alpha_2-\beta_2 & -\alpha_{22} \\ -\delta_{21} & -\delta_{22} & -\delta_{22} & -\alpha_{21} & -\alpha_{22} & -\alpha_2-\beta_2 \end{pmatrix} \tag{5.126}$$

and

$$\begin{aligned}
\alpha_1(T) &= A_1S + A_1^2S < I_1^z > \frac{u_k^2+v_k^2}{w_k} \\
\alpha_2(T) &= A_2S + A_2^2S < I_2^z > \frac{u_k^2+v_k^2}{w_k} \\
\alpha_{12}(T) &= A_1A_2S < I_1^z > \frac{u_k^2+v_k^2}{w_k} \\
\alpha_{21}(T) &= A_1A_2S < I_2^z > \frac{u_k^2+v_k^2}{w_k} \\
\alpha_{22}(T) &= A_2^2S < I_2^z > \frac{u_k^2+v_k^2}{w_k} \\
\delta_{11}(T) &= 2A_1^2S < I_1^z > \frac{u_kv_k}{w_k} \\
\delta_{22}(T) &= 2A_2^2S < I_2^z > \frac{u_kv_k}{w_k}
\end{aligned}$$

$$\begin{aligned}
\delta_{12}(T) &= 2A_1A_2S < I_1^z > \frac{u_k v_k}{w_k} \\
\delta_{21}(T) &= 2A_1A_2S < I_2^z > \frac{u_k v_k}{w_k} \\
\beta_1(T) &= -4A_1U_z(A_1 < I_1^z > +2A_2 < I_2^z >) \\
\beta_2(T) &= -4A_2U_z(A_1 < I_1^z > +2A_2 < I_2^z >)
\end{aligned} \tag{5.127}$$

We expect that $U_{ll}^{+-} \gg U_z$, and numerical results show that $U_z/h = 1.0 \cdot 10^{-10}$ MHz^{-1}. We will therefore ignore terms involving U_z, namely $\beta_1(T)$ and $\beta_2(T)$.

Finally, the power spectrum can be calculated

$$P(\omega, k) = \int dt\, e^{i\omega t} \left(< \Upsilon_k^-(t)\Upsilon_k^+(0) > + < \Upsilon_k^+(t)\Upsilon_k^-(0) > \right) \tag{5.128}$$

where Υ is the sum of the spins at each of the three lattice sites,

$$\Upsilon_k^{\pm}(t) = I_k^{\pm}(t) + I_{a,k}^{\pm}(t) + I_{b,k}^{\pm}(t) \tag{5.129}$$

In the case of a single spin per lattice site, one of the terms in equation 5.128 is zero due to energy conservation. For MnAc, both terms contribute because the effective hyperfine field is in opposite directions for the Mn1 and Mn2 sites.

The resonant lines in the power spectrum will correspond to the eigenvalues of the matrix G. There are three excitation modes. The first corresponds to an unpulled optical mode where the 2 Mn2 sites precess in opposition of phase and there is no precession of the Mn1 spins. From equation 5.128 and 5.129 it is clear that this mode should not be absorbed. Indeed, there is no net precession of the magnetization and this mode should not couple to the precessing magnetic field [28]. Although the other two modes involve precession of all three spins it is worthwhile to note that the spins of the Mn2 sites precess exactly in phase. Also, the higher frequency mode corresponds almost entirely to precession of the Mn2 spins, while the lower frequency mode corresponds mostly to

motion of the Mn1 spin. This admixture between Mn1 and Mn2 spins decreases with increasing separation of the unpulled frequencies.

In principle it is possible to integrate equation 5.125 by assuming that $dI^z/dt = 0$, without making the approximation $I_i^z =< I^z >$. Indeed, this is justified in the sense that $< dI^z/dt > \ll < dI^{\pm}/dt >$. It is then possible to calculate the first moment of the power spectrum. The first moment gives the resonant lines already calculated.

5.4 The frequency pulling at $T = 0$ calculated with spin wave theory

The low temperature limit of the theory can be calculated using spin wave theory. We can make following Holstein-Primakoff transformation,

$$\begin{aligned}
I_j^z &= I - c_j^\dagger c_j \\
I_j^+ &\simeq \sqrt{2I}c_j \\
I_j^- &\simeq \sqrt{2I}c_j^\dagger \\
I_{a,j}^z &= -I + a_j^\dagger a_j \\
I_{a,j}^+ &\simeq \sqrt{2I}a_j^\dagger \\
I_{a,j}^- &\simeq \sqrt{2I}a_j \\
I_{b,j}^z &= -I + b_j^\dagger b_j \\
I_{b,j}^+ &\simeq \sqrt{2I}b_j^\dagger \\
I_{b,j}^- &\simeq \sqrt{2I}b_j
\end{aligned} \tag{5.130}$$

where $\vec{I}_j$ refers to the Mn1 sites, and $\vec{I}_{a,j}$ and $\vec{I}_{b,j}$ refer to the 2 Mn2 sites. The Hamiltonian can then be written in terms of the annihilation and creation operators introduced in equations 5.130. If we then work in momentum space,

$$d_j = \frac{1}{\sqrt{N}} \sum_k e^{ikR_j} d_k \tag{5.131}$$

where d_j is any of the annihilation operators, a_j,b_j or c_j, then the Hamiltonian can be expressed as

$$H = \sum_{k+} \begin{pmatrix} c_k^\dagger & a_{-k} & b_{-k} & c_{-k} & a_k^\dagger b_k^\dagger \end{pmatrix} Q_k \begin{pmatrix} c_k \\ a_{-k}^\dagger \\ b_{-k}^\dagger \\ c_{-k}^\dagger \\ a_k \\ b_k \end{pmatrix} \tag{5.132}$$

where

$$Q_k = \begin{pmatrix} -\alpha_1 - \beta_1 & -\alpha_{12} & -\alpha_{12} & -\delta_{11} & -\delta_{12} & -\delta_{12} \\ \alpha_{21} & \alpha_2 + \beta_2 & \alpha_{22} & \delta_{21} & \delta_{22} & \delta_{22} \\ \alpha_{21} & \alpha_{22} & \alpha_2 + \beta_2 & \delta_{21} & \delta_{22} & \delta_{22} \\ -\delta_{11} & -\delta_{12} & -\delta_{12} & -\alpha_1 - \beta_1 & -\alpha_{12} & -\alpha_{12} \\ \delta_{21} & \delta_{22} & \delta_{22} & \alpha_{21} & \alpha_2 + \beta_2 & \alpha_{22} \\ \delta_{21} & \delta_{22} & \delta_{22} & \alpha_{21} & \alpha_{22} & \alpha_2 + \beta_2 \end{pmatrix} \tag{5.133}$$

and α_1, α_2, α_{12}, α_{21}, δ_{12}, δ_{21}, δ_{22}, β_1 and β_2 are defined in equations 5.127 but here are taken at $T = 0$. In order to diagonalize Q_k and find the spectra of the excitations, it is necessary to diagonalize in the metric η in order to preserve the correct commutation relations between the bosonic annihilation and creation operators, where

$$\eta = \begin{pmatrix} -1 & 0 & 0 & 0 & 0 & 0 \\ 0 & 1 & 0 & 0 & 0 & 0 \\ 0 & 0 & 1 & 0 & 0 & 0 \\ 0 & 0 & 0 & 1 & 0 & 0 \\ 0 & 0 & 0 & 0 & -1 & 0 \\ 0 & 0 & 0 & 0 & 0 & -1 \end{pmatrix} \tag{5.134}$$

As discussed earlier, it is necessary to find the eigenspectrum of ηQ_k in the usual sense. However, $\eta Q_k = G_k(0)$ and the spectra calculated by both techniques are identical at T=0.

5.5 Linewidth

The calculation of the second moment is quite complicated because of the three spins. We shall return to the case of a single spin in order to understand the behaviour of the linewidth as a function of temperature.

The Suhl-Nakamura Hamiltonian is

$$\begin{aligned} H &= H_0 + H_1 \\ &= AS\sum_i I_i^z + \frac{1}{2}\sum_{ij} U_{ij} I_i^+ I_j^- \end{aligned} \tag{5.135}$$

The power spectrum is given by

$$P_k(\omega) = \int dt \; < I_k^+(t) I_k^-(0) > \exp(i\omega t) \tag{5.136}$$

where $I_k^{\pm}$ are defined in equation 5.121. The thermodynamic average is defined as

$$< O >= \frac{Tr[e^{-\beta H} O]}{Tr[e^{-\beta H}]} \tag{5.137}$$

This expression of the power spectrum implies that $A < 0$ and we have chosen our axis of quantization such that $< I_j^z > \rightarrow +I$ as $T \rightarrow 0$.

Because $AS \gg \sum_i U_{ij}$ we can, to an excellent approximation, calculate the thermodynamic averages with $H = H_0$. Following Van Vleck's method of moments [29], we can calculate the nth moment of the power spectrum, defined as

$$< \omega^n >= \frac{\int d\omega \, \omega^n P_k(\omega)}{\int d\omega \, P_k(\omega)} \tag{5.138}$$

Using integration by parts, the first and second moments can be expressed as

$$< \omega > = -i\frac{< dI_k^+/dt\ I_k^- >}{< I_k^+ I_k^- >} \tag{5.139}$$

$$< \omega^2 > = -\frac{< d^2 I_k^+/dt^2\ I_k^- >}{< I_k^+ I_k^- >} \tag{5.140}$$

Since $dI_k^+/dt = i[H, I_k^+]$,

$$< \omega > = \frac{< [H, I_k^+] I_k^- >}{< I_k^+ I_k^- >} \tag{5.141}$$

$$< \omega^2 > = -\frac{< [H, [H, I_k^+]] I_k^- >}{< I_k^+ I_k^- >} \tag{5.142}$$

The width of the resonance, $(\Delta\omega)^2 =< \omega^2 > - < \omega >^2$ can then be calculated.

Since we are interested in the uniform mode ($k = 0$), we will restrict ourselves to that case from here on. The first moment can be evaluated from

$$\sqrt{N}[H, I_{k=0}^+] = AS \sum_m I_m^+ - \sum_{im} U_{im} I_i^+ I_m^z \tag{5.143}$$

When calculating the thermodynamic averages, we have used $H = H_0$ and therefore $< I_i^+ I_m^z I_j^- >=< I_i^+ I_j^- >< I_m^z > \delta_{ij}$ when $i \neq m$. Of course, when $i = m$ we can, to a good approximation at low temperatures, use $< I_i^+ I_m^z I_j^- >=< I_i^+ I_j^- >< I_m^z - 1 > \delta_{ij}$. With these approximations, we find

$$< \omega >= AS + U_{jj} - \sum_i U_{im} < I^z > \tag{5.144}$$

where m is arbitrary but fixed. This is the expected result because

$$\sum_i U_{im} = -\frac{A^2 S}{\omega_0} \tag{5.145}$$

and this gives the same frequency pulling as equation 4.74.

The second moment has been calculated by an expansion in $1/T$ [4], and the linewidth is found to be

$$(\Delta\omega) = (\Delta\omega_\infty)\left(1 - \frac{3|\delta\omega|}{8 < \omega >}\right) \tag{5.146}$$

where $(\Delta\omega_\infty)$ is the high temperature linewidth and $\delta\omega = \sum_i U_{im} < I^z >$ is the frequency pulling.

However, the result of Pincus has two problems for our application. Firstly, it is only valid when $AS \ll k_B T$ which is certainly not the case at the temperatures of interest to us. Secondly, it is calculated assuming that there is no self interaction term ($U_{ii} = 0$).

The second moment can be calculated from

$$\sqrt{N}[H,[H,I^+_{k=0}]] = A^2S^2\sum_j I^+_j - 2AS\sum_{im} U_{im}I^+_i I^z_m - \frac{1}{2}U_{ij}U_{nm}[I^+_i I^-_j, I^+_n I^z_m] \quad (5.147)$$

where there are no restrictions on the indices i, j, n and m. The second moment can be evaluated using $H = H_0$ to evaluate thermodynamic averages and by assuming that

$$\begin{aligned} < I^+_i I^z_i I^-_i > &\sim < I^+_i I^-_i >< I^z_i - 1 > \\ < I^+_i I^z_i I^z_i I^-_i > &\sim < I^+_i I^-_i >< (I^z_i - 1)^2 > \end{aligned} \quad (5.148)$$

The final result for the linewidth is

$$\begin{aligned} (\Delta\omega)^2 &= U_{ii}\left(\sum_i U_{ij}\right)\left[\frac{3 < (I^z)^2 >}{2} + \frac{< I^z >}{2} - \frac{I(I+1)}{2} - < I^z >^2\right] \\ &+ \sum_i U^2_{ij}\left[< I^z >^2 - \frac{< I^z >}{2} + \frac{I(I+1)}{2} - \frac{< (I^z)^2 >}{2}\right] \\ &- U^2_{ii} < I^z >^2 \end{aligned} \quad (5.149)$$

The linear terms in $< I^z >$ appear to indicate that the linewidth depends on the choice of quantization axis. However, the expression of the power spectrum in equation 5.136 changes if the quantization axis changes. If $z \to -z$, the Green's function used to calculate the power spectrum is $< I^-_k(t) I^+_k(0) >$. If the linewidth is recalculated in this case we find, of course, that the linewidth in independent of the choice of quantization axis. It is important to remember that in equation 5.149 the linear terms are positive. The linear term in the result of Pincus (equation 5.146) is expressed as an absolute value to avoid this confusion.

Note that, at high temperature $< I^z >= 0$ and $< (I^z)^2 >= \frac{I(I+1)}{3}$. Therefore $(\Delta\omega_\infty)^2 = \frac{1}{3}\sum_i U_{ij}^2 I(I+1)$. This is precisely the result of van Vleck [29] calculated at the high temperature limit and is also the high temperature limit used by Pincus [4]. Since the result of Pincus is only valid for $U_{ii} = 0$, we can compare the two predictions in this case (see figure 5.35). The results agree well when $k_B T \gg AS$ when the high temperature expansion is valid, but they deviate markedly at low temperatures when our approximation should be valid.

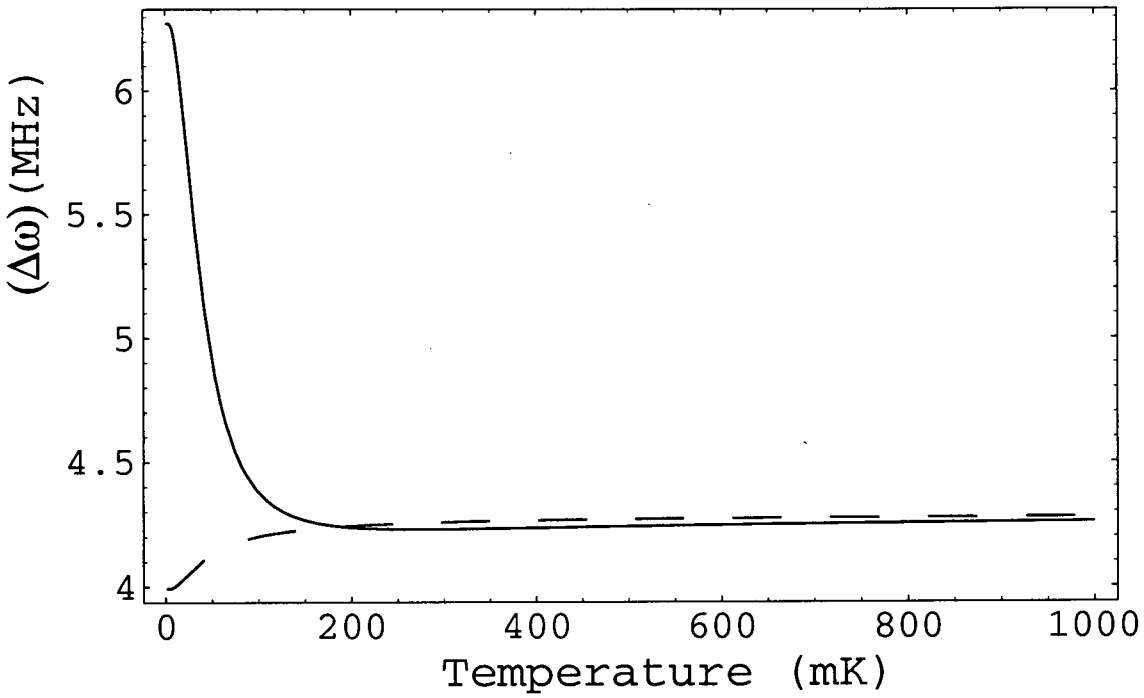

Figure 5.35: The mean square width for $U_{ii} = 0$, $\sum_i U_{ij} = 14.1$ MHz, and $\sum_i U_{ij}^2 = 6.3$ MHz. The dashed line is the prediction of Pincus.

It is also useful to consider the case where only the self interaction term is present. In this case,

$$(\Delta\omega)^2 = U_{ii}^2 \left(< (I^z)^2 > - < I^z >^2 \right) \tag{5.150}$$

This is exactly the result expected for a pseudoquadrupolar splitting. At $T = 0$ only the

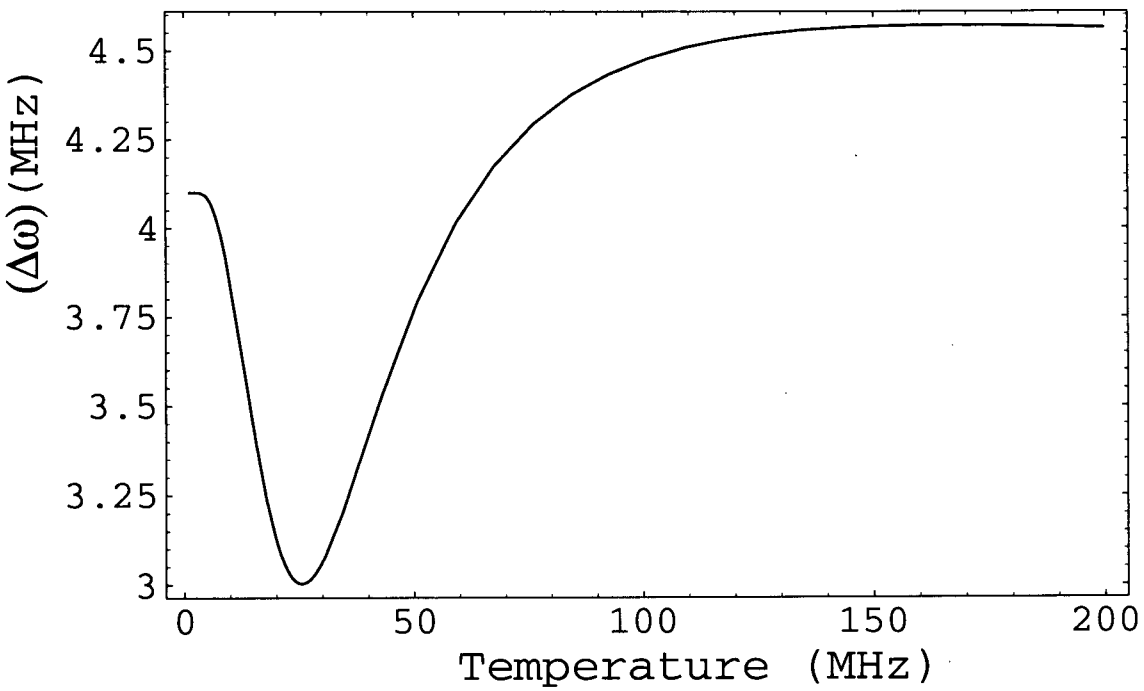

Figure 5.36: The mean square width for $U_{ii} = 1.9$ MHz, $\sum_i U_{ij} = 14.1$ MHz, and $\sum_i U_{ij}^2 = 6.3$ MHz.

lowest energy level is occupied and the line is infinitely narrow. At $T = \infty$, the resonance is made up of six individual transitions of equal amplitude, with a spacing U_{ii} between each. The linewidth for such a resonance is clearly on the order of $U_{ii}I$.

The result when U_{ii} is not zero is shown in figure 5.36. The temperature dependence of the linewidth is very surprising, precisely in the region of interest for our experiments. These results indicate that the temperature dependence of the linewidth in the more complicated case involving triplets of nuclear spins may be unusual precisely in the region of interest for our data. Indeed, some of the unusual temperature dependence of the linewidths in the experimental data may indicate that these effects are present. Unfortunately, the second moment has not been calculated in the case of the triplet nuclear spins because it is difficult to find which terms contribute to which of the four lines. In order for a second moment calculation to be meaningful only terms contributing to a single resonance should be included.

5.6 Calculating the exact power spectrum for 1 to 4 spins

In order to explore the change in linewidth with temperature, and the possibility that the splitting of the pulled Mn2 line could be lost in the linearization procedure, we have calculated numerically the exact power spectrum for up to four spins with I=5/2, including nearest neighbour interactions. The simplified Hamiltonian used, for a single spin has the form

$$H = \sum_i \left(aI_i^z + \frac{b}{2} I_i^+ I_i^- \right) + \frac{c}{2} \sum_{<ij>} I_i^+ I_j^- \tag{5.151}$$

where $< ij >$ denotes a sum over nearest neighbours. In the simulations, $a/h = 500$ MHz, $b/h = 2$ MHz and $c/h = 1$ MHz. The power spectrum is calculated by diagonalizing the Hamiltonian and using equation 5.128. The results for one to four spins at $k_B T/h = 500$ MHz can be seen in figure 5.37, and for four spins at different temperatures in figure 5.38.

These numerical results indicate that the pseudoquadrupolar structure is smoothed out as the number of interacting spins increases. If there are N spins, the matrix to diagonalize is of dimension $n \times n$ where $n = (2I+1)^N$. Using the fact that the Hamiltonian conserves the total angular momentum ($[H, \sum_i I_i^z] = 0$) allows the matrix to be reduced to a block diagonal form. However, it is still very difficult to treat numerically the case of a real crystal lattice with longer range interactions.

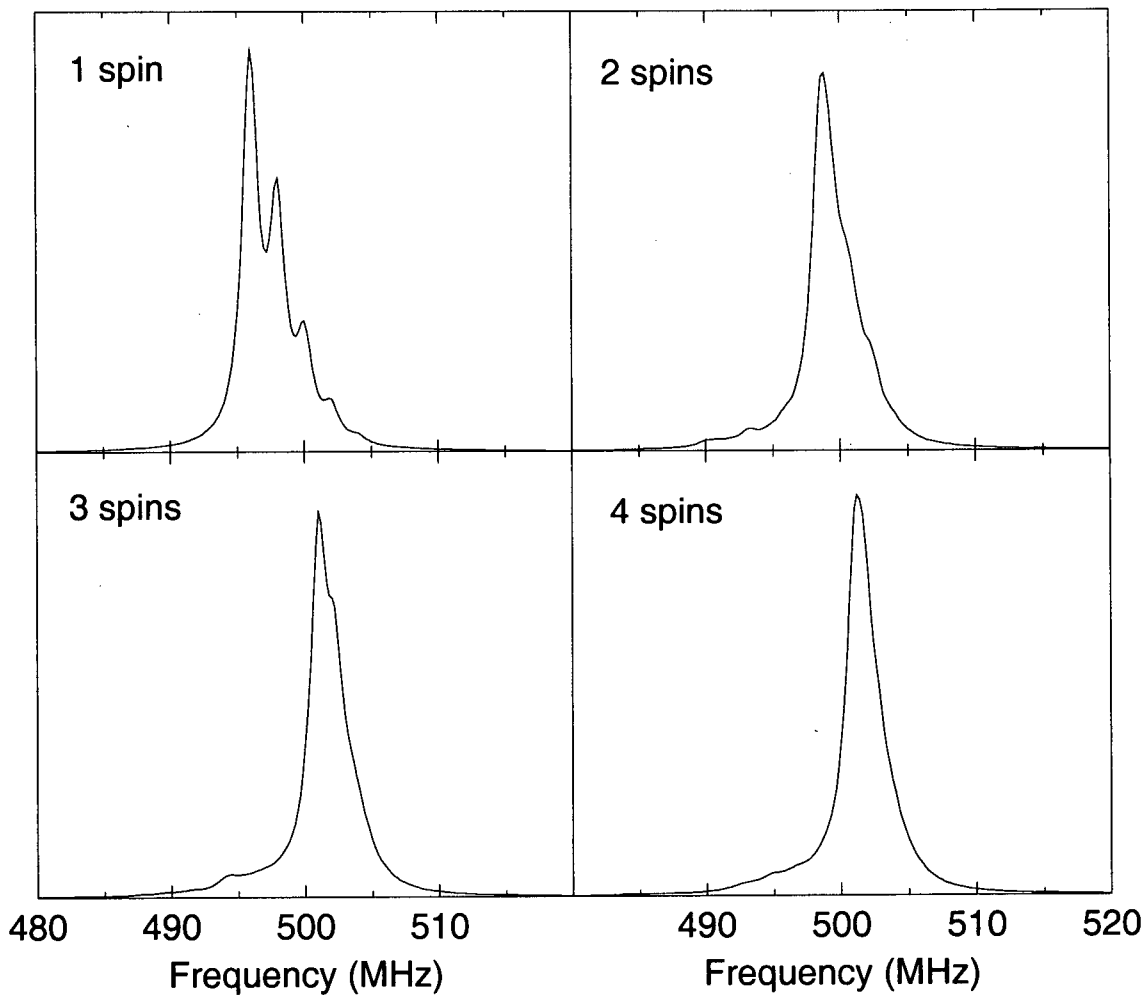

Figure 5.37: The exact power spectrum for one to four spins at $k_B T/h = 500$ MHz or $T = 24$ mK, including pseudoquadrupolar interactions of 2 MHz and nearest neighbour interactions of 1 MHz

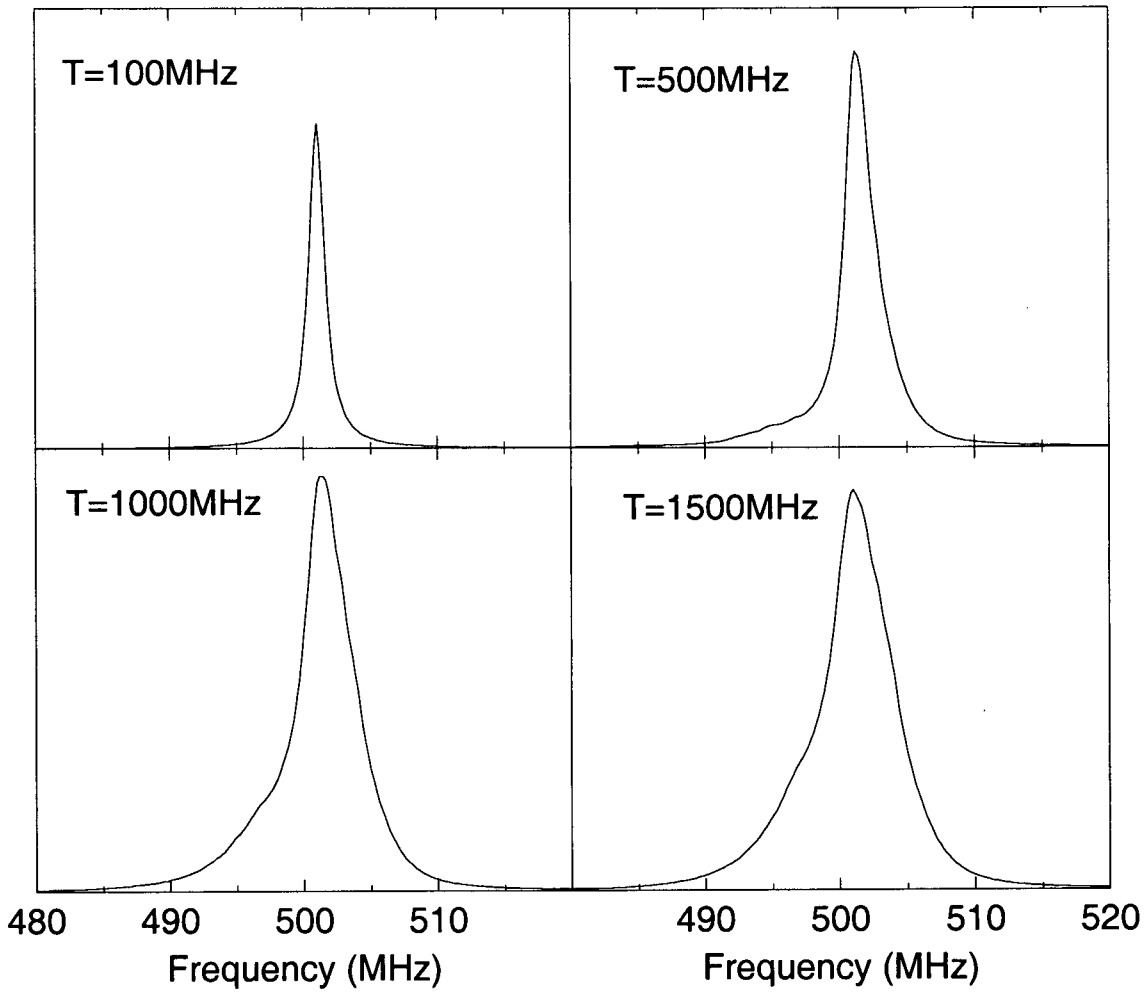

Figure 5.38: The exact power spectrum for four spins at different temperatures, including pseudoquadrupolar interactions of 2 MHz and nearest neighbour interactions of 1 MHz. The temperatures ($T = h\nu/k_b$) are: 4.8 mK, 24 mK, 48 mK and 72 mK.

5.7 Classical model and simulations

In order to perform numerical simulations involving more spins, it is simpler to work in a classical system. We shall first consider the classical theoretical predictions of a crystal with a single nucleus per lattice site. We will then compare these predictions to some classical simulations. We show that, qualitatively, these simulations confirm the picture we have developed from the quantum mechanical treatment of the frequency pulling.

The Hamiltonian can be written as

$$\begin{aligned} H &= AS\sum_i I_i^z + \frac{1}{2}\sum_{ij} U_{ij} I_i^+ I_j^- \\ &= AS\sum_i I_i^z + \frac{1}{2}\sum_{ij} U_{ij}(I_i^x I_j^x + I_i^y I_j^y) \\ &= \sum_i \left(AS\hat{u}_z + \frac{1}{2}\sum_j U_{ij}(I_j^x \hat{u}_x + I_j^y \hat{u}_y) \right) \cdot \vec{I}_i \\ &= \sum_i \gamma_N \vec{B}_i \cdot \vec{I}_i \end{aligned} \tag{5.152}$$

The equation of motion of each spin is, in the reference frame rotating at angular velocity ω,

$$\frac{d\vec{I}_i}{dt} = \gamma_N \vec{I}_i \times \vec{B}_{eff} \tag{5.153}$$

where $\vec{B}_{eff} = \vec{B}_i + \vec{\omega}/\gamma_N$. The equations of motion can be linearized by replacing I_i^z with its thermodynamic average, $< I^z >$ in all quadratic terms. The result for the uniform mode ($k = 0$), in the rotating reference frame, is

$$\frac{d\vec{I}_0}{dt} = \begin{pmatrix} I_0^y(AS + \omega - \frac{1}{2}\sum_i U_{ij} < I^z >) \\ bI_0^z - I_0^x(AS + \omega - \frac{1}{2}\sum_i U_{ij} < I^z >) \\ -bI_0^y \end{pmatrix} \tag{5.154}$$

where b is the amplitude of the oscillating magnetic field. The resonance condition is clearly

$$\omega = -\left(AS - \frac{1}{2}\sum_i U_{ij} < I^z > \right) \tag{5.155}$$

In other words, the frequency pulling effect predicted classically is the same as the effect predicted quantum mechanically in equation 5.144 except for the factor of 1/2 in the second term of equationclassicalpulling.

Classical simulations were performed with an array of 15 by 15 nuclear spins. The spins were first thermalized without including the interaction terms. The interactions and the oscillating magnetic field were then added, and the system was evolved for a short period of time, Δt. The change in I^z was measured for each spin, and the absorbed power is then

$$\begin{aligned} P &\simeq \frac{AS}{\Delta t}\sum_j I_j^z(t=\Delta t) - I_j^z(t=0) \\ &\propto < I_f^z - I_i^z > \end{aligned} \tag{5.156}$$

where the average <> is taken over all the spins in the lattice, $I_f^z = I^z(t = \Delta t)$ and $I_i^z = I^z(t = 0)$. Δt was chosen in order to remain in the limit of CW NMR. The centre frequency of the resonance was obtained by plotting the P as a function of frequency.

The result of several simulations at the same temperature (10 mK) with longer and longer range interactions is shown in figure 5.39. The results of several simulations at different temperatures is shown in figure 5.40. The agreement with the theory is reasonable, even with a short range interaction. The discrepancy may be partly due to errors associated with the strength of the oscillating magnetic field. In order to perform the simulations in a reasonable time, the oscillating field was stronger by five orders of magnitude than it is experimentally. The discrepancy between the theory and the simulations was reduced when the oscillating field was reduced.

A simulation involving an array of 12 by 12 triplets of spins was also performed, and the results can be seen in figure 5.41. Only interactions within a triplet of spins were included in the calculation. The quantity plotted is $< I_f^z - I_i^z >$ where the average is over the Mn1 spins or one of the Mn2 spins. It appears there are only two resonances.

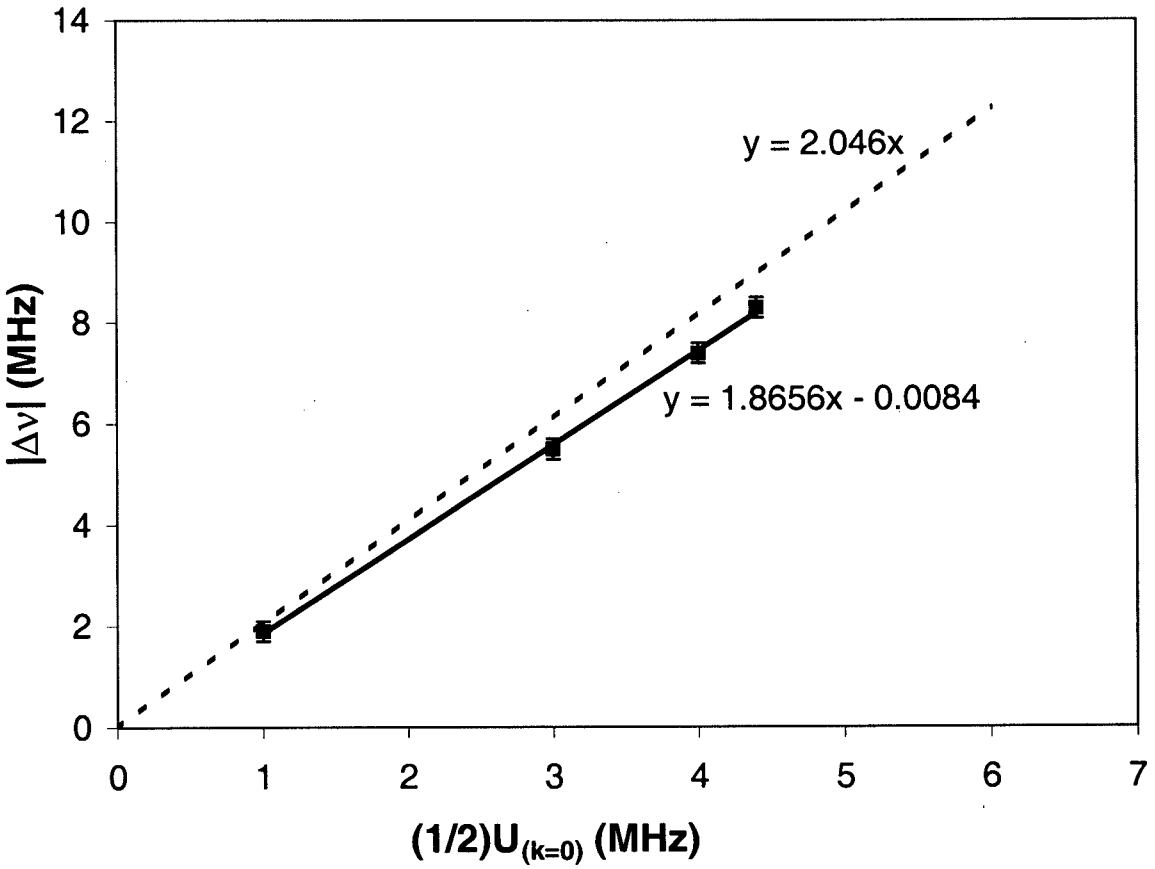

Figure 5.39: The frequency pulling for a variety of interactions at $T = 10$ mK. Each data point is calculated by increasing the range of U_{ij}. The first point corresponds to only a self interaction of 2 MHz. A nearest neighbour interaction of 1 MHz was added, then a second nearest neighbour interaction of 0.5 MHz and finally a third nearest neighbour interaction of 0.2 MHz. The solid line is the best fit to the data, and the dashed line is the prediction of equation 5.155 because at $T = 10$ mK, $< I^z >= 2.046$.

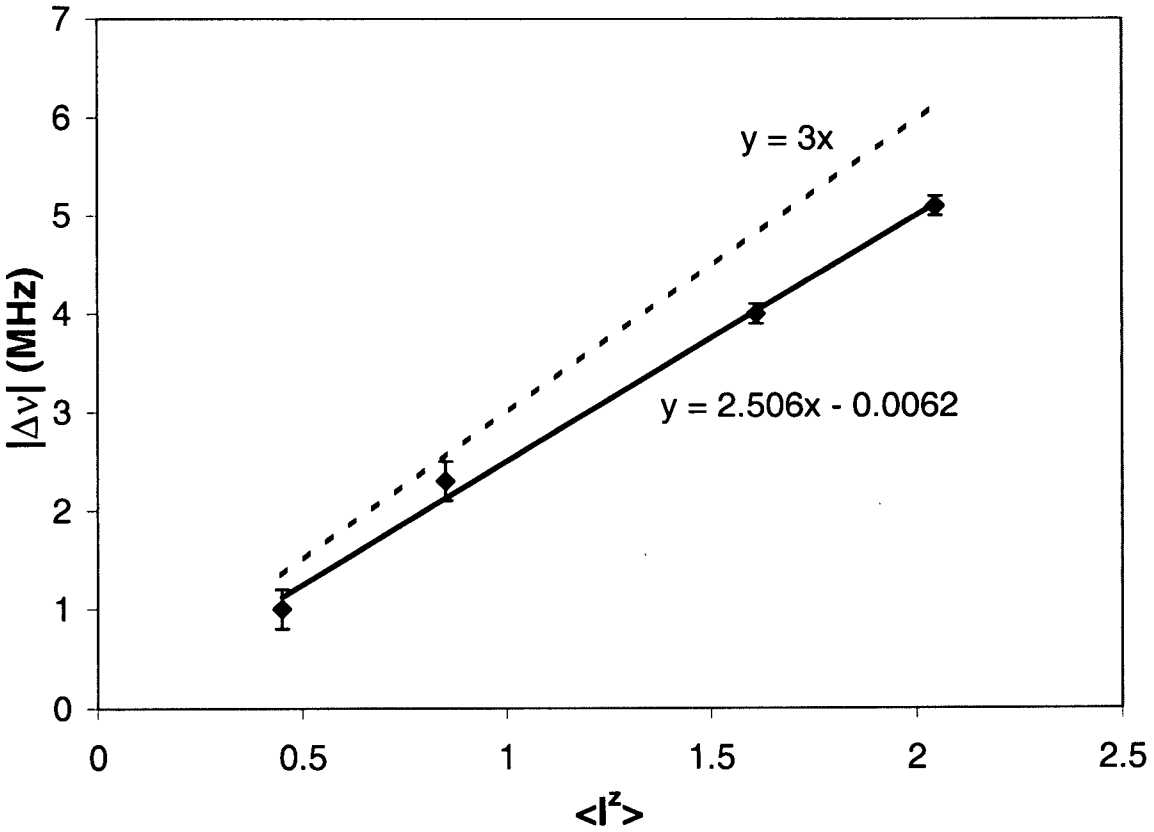

Figure 5.40: The frequency pulling for a variety of temperatures (10, 20, 50, 100 mK) with a self interaction of 2 MHz and a nearest neighbour interaction of 1 MHz. The solid line is the best fit to the data, and the dashed line is the prediction of equation 5.155.

The first corresponds mainly to precession of the Mn1 spins, while the higher frequency line corresponds mainly to precession of the Mn2 spins.

In order to observe the unpulled optical mode, as discussed in section 5.3.2, the quantity $< |I_f^z - I_i^z| >$ was calculated for the Mn2 spins (see figure 5.42). The increased self interaction was of 10 MHz and the temperature of 1 mK was used in order to separate the pulled and unpulled modes. The result can be seen in figure 5.42. Both the unpulled optical mode and the frequency pulled mode are visible. It was verified that the Mn2 spins precess in opposition of phase in the unpulled mode, and in phase in the pulled mode. Therefore, in the unpulled mode, the power absorbed by one of the spins is given up by the other Mn2 spin and there is no net power absorption.

It should be noted that the frequency pulled Mn2 mode involves some precession of the Mn1 spin. It was also found that the Mn1 mode contained some precession of the Mn2 spins. However, the unpulled optical mode involves no precession of the Mn1 spins. The unpulled optical mode has no net precession of magnetization to couple to the oscillating RF field and the optical mode is not visible in the plot of the power spectrum. These results confirm qualitatively the picture obtained from quantum mechanical calculations in section 5.3.2. Unfortunately, due to numerical limitations, it was not possible to include sufficiently long range interactions to compare the simulations to experimental data.

5.8 Comparing the theoretical model to the experimental results

The data and models are plotted together in figure 5.43. The data were obtained from spectra such as that shown in figure 4.31, as explained in section 4.2.3. The theoretical line is a fit using B_A^b and B_A^c as the only free parameters. The fit had to be performed in several steps because the power spectrum has four lines rather than the expected two. In

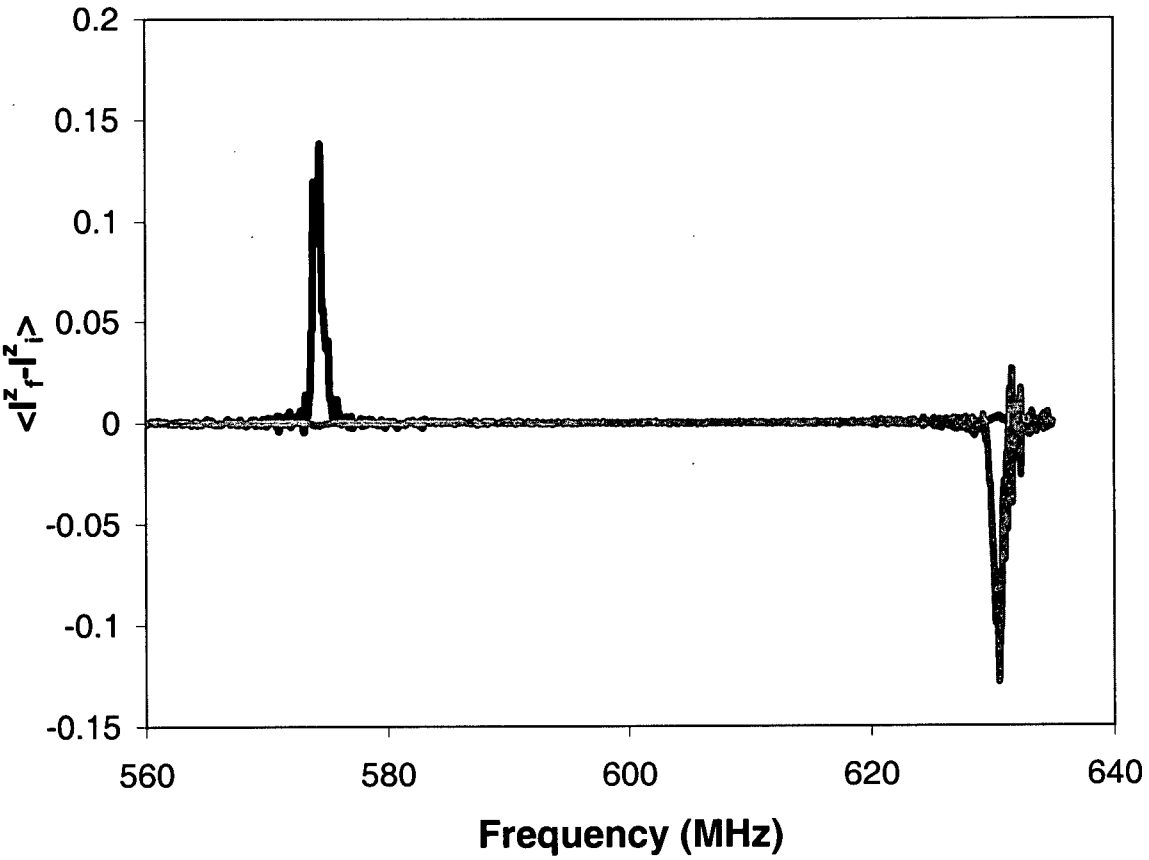

Figure 5.41: The quantity $< I_f^z - I_i^z >$, which is proportional to the power spectrum, as a function of frequency for triplets of spins. The self interaction term which allows interactions between the three spins within a triplet is 2 MHz. The unpulled frequencies are 573.8 MHz and 631.7 MHz. The temperature is 10 mK. The black line is the average change of the the Mn1 spin, while the grey line is the average change of one of the Mn2 spins.

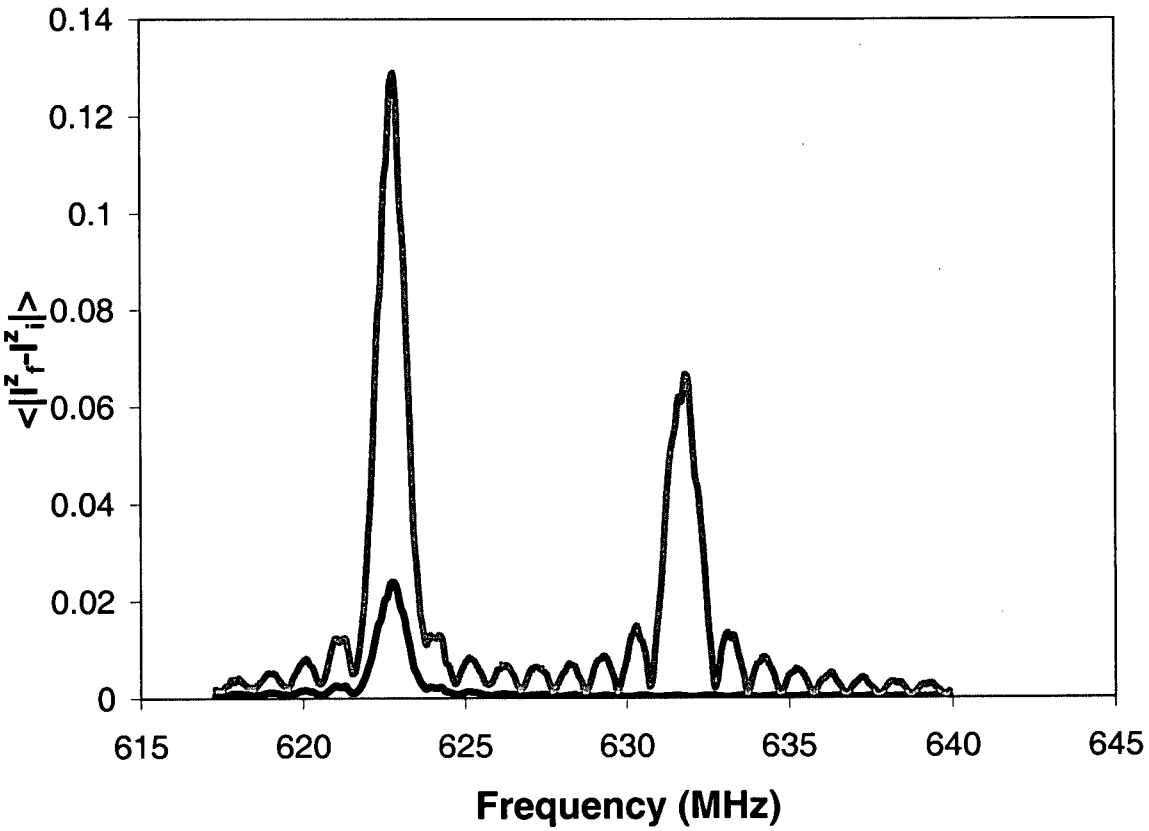

Figure 5.42: The quantity $< |I_f^z - I_i^z| >$ as a function of frequency for triplets of spins. The self interaction term which allows interactions between the three spins within a triplet is 10 MHz. The unpulled frequency is 631.7 MHz. The temperature is 1 mK. The black line corresponds to the Mn1 spin, while the grey line corresponds to one of the Mn2 spins.

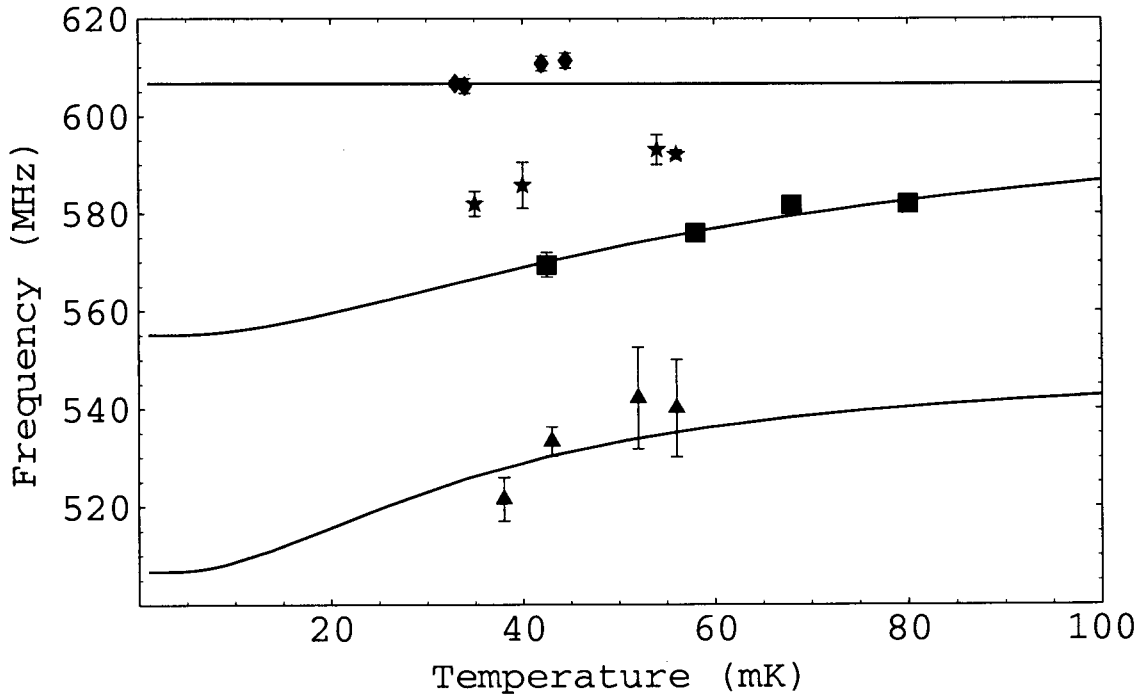

Figure 5.43: The spectrum of the zero momentum nuclear spin excitations as a function of temperature and the experimental data. The best fit values are $B_A^b = 0.27 \pm 0.03$ T and $B_A^c = 0.81 \pm 0.05$ T.

each of the χ^2 fits described below, four data points were used. A reasonable fit should yield $\chi^2_{min} \simeq 4$.

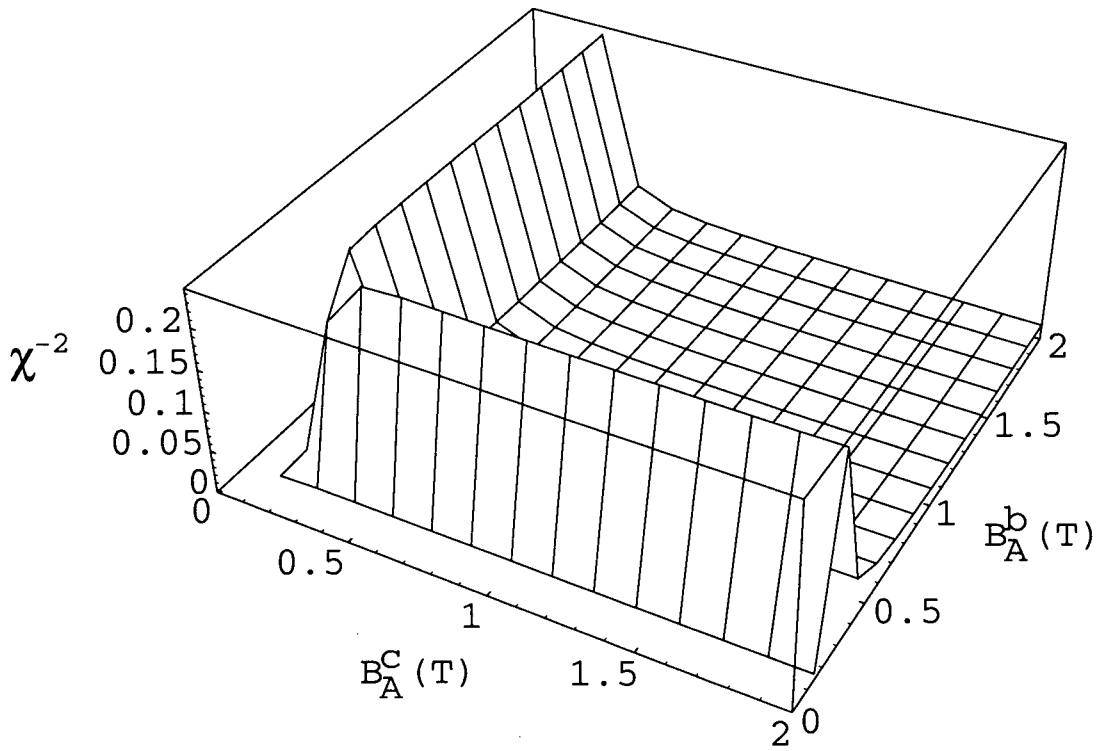

Figure 5.44: $1/\chi^2$ as a function of both B_A^b and B_A^c for the fit to the lowest frequency resonance (corresponding mainly to precession of the Mn1 spins).

A χ^2 fit was first performed on only the lowest frequency line (corresponding essentially to the precession of the Mn1 spins). This is the obvious choice because the resonance corresponding to Mn2 spins precessing in phase is split into two lines. A graph of $1/\chi^2$ is shown in figure 5.44. The inverse of χ^2 is shown because it is easier to see a maximum, rather than a minimum. This plot is interesting because it shows that only one of the two parameters can be determined from this fit. This is essentially because the errors on the low frequency line are relatively large. The slope of the line is therefore difficult to determine from the data. What can be determined is the overall magnitude

of the frequency pulling effect which depends almost entirely on the smallest of the two anisotropy fields. It is impossible to determine from this model whether the smallest field corresponds to the b or the c directions. However, we know from the results of Cowen *et al.* [20] that B_A^b is the smaller anisotropy field. Our fit then yields $B_A^b = 0.27 \pm 0.03$ T.

In order to determine the value of B_A^c we need to fit the model to the data from the higher frequency lines corresponding essentially to precession of the Mn2 spins. There are two choices of lines. A χ^2 fit was performed on both of the possible resonances independently. The free parameter was B_A^c while B_A^b was fixed at 0.27 T. The plots of χ^2 vs B_A^c are shown for both the lower and higher frequency Mn2 lines in figures 5.45 and 5.46 respectively. Clearly, the lower frequency Mn2 line gives an excellent fit (figure 5.45) with $B_A^c = 0.81 \pm 0.05$ while the higher frequency line (figure 5.46) cannot be fitted reasonably.

The unpulled optical mode is not frequency pulled and does not have any dependence on the anisotropy fields.

The conclusion is that Mn1 resonance, and the lower of the frequency pulled Mn2 resonances are described well by our model, with $B_A^b = 0.27 \pm 0.03$ T and $B_A^c = 0.81 \pm 0.05$ T. The higher of the frequency pulled Mn2 lines is an excitation not described by our model. Furthermore, our model correctly predicts the existence of an unpulled optical mode involving precession of the Mn2 spins, but does not explain how this mode is excited by an RF field.

The values of the anisotropy fields previously measured at 1.2 K are $B_A^b = 0.14$ T and $B_A^c = 0.86$ T [20]. While our results for B_A^c are entirely consistent with this result, B_A^b is significantly different. There are several explanations for this discrepancy. The first is that the anisotropy fields depend on temperature, and were only previously measured down to 1.2 K. The trend for B_A^b is to increase with decreasing temperature. Cowen *et al.* did not include the trend for B_A^c. Another source of discrepancy is relating

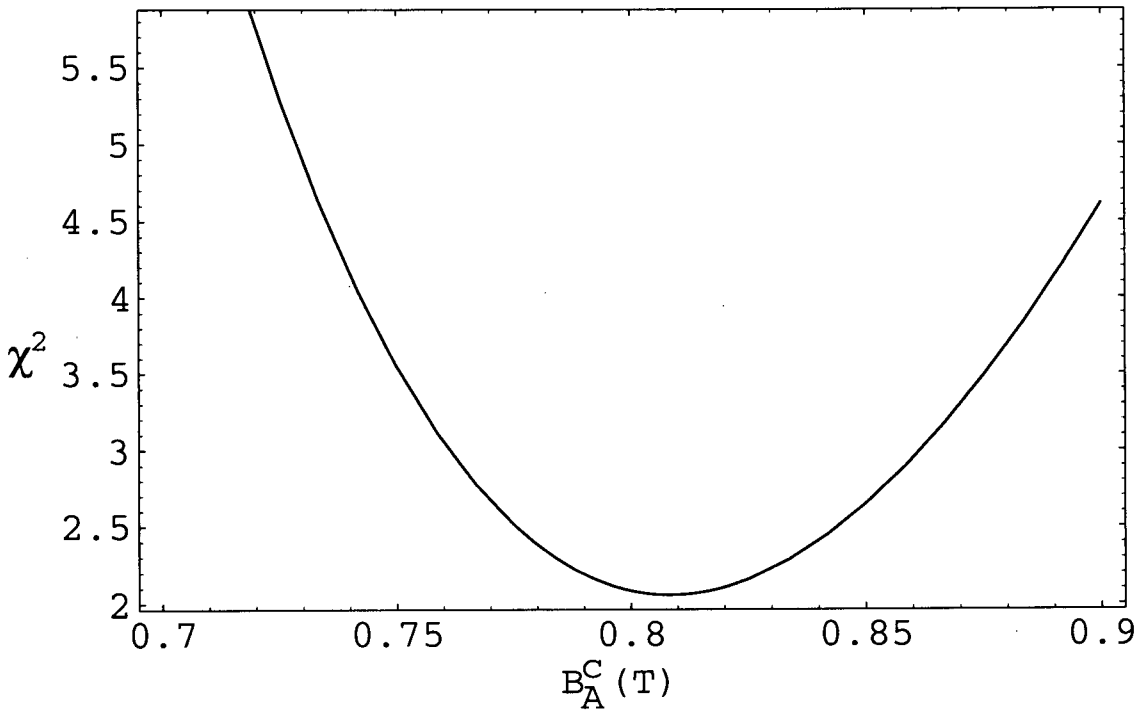

Figure 5.45: χ^2 as a function of B_A^c for the lower of the 2 resonances corresponding mainly to precession of the Mn2 spins. B_A^b was fixed at 0.27 T. The graph shows the best fit be $B_A^c = 0.81 \pm 0.05$ T.

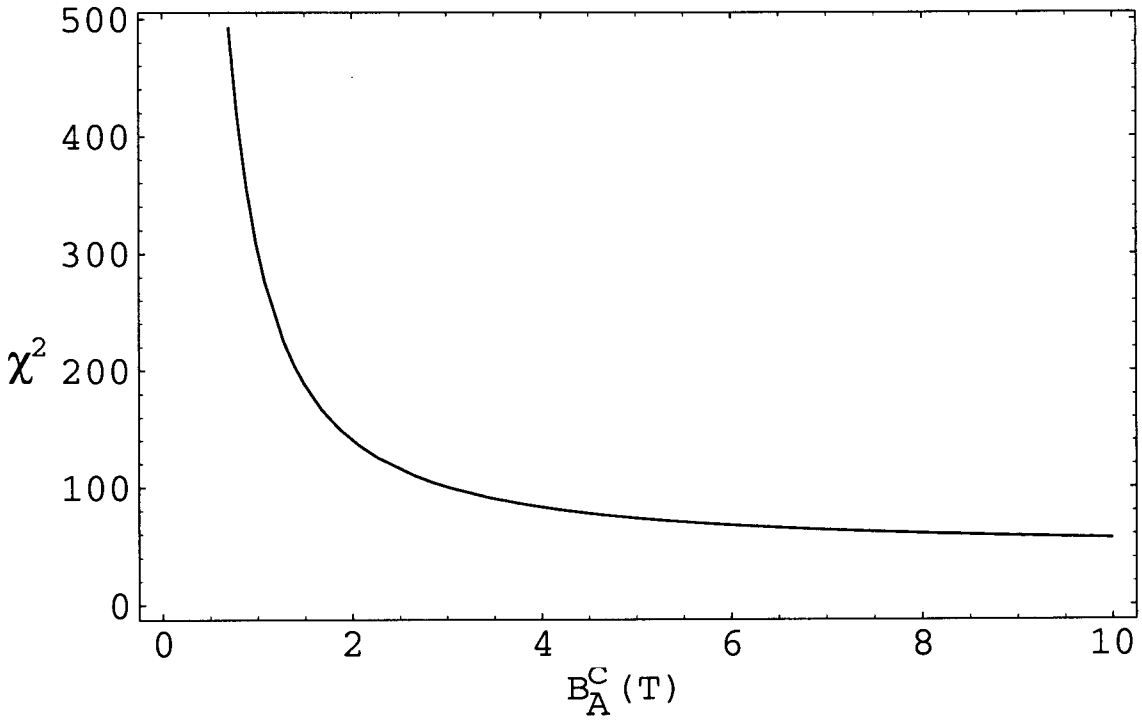

Figure 5.46: χ^2 as a function of B_A^c for the higher of the 2 resonances corresponding mainly to precession of the Mn2 spins. B_A^b was fixed at 0.27 T. There is no physical minimum for χ^2, indicating that the model does not describe the magnitude and temperature dependence of this resonance.

the parameter measured by Cowen *et al.* with the parameter of our model. Indeed, Cowen *et al.* measured the anisotropy fields by measuring the field necessary to force the magnetization into the b and c directions. Relating that field to our parameters requires the assumption that only quadratic terms in S_i^b and S_i^c are present in the original electron spin Hamiltonian (equation 5.86). Ignoring higher order terms is justified in our model because the $< S_i^a > \simeq S$, but is not justified when forcing the magnetization into the b and c directions.

The relatively small errors reported in the values of the anisotropy fields are an indication of the sensitivity of the frequency pulling to the anisotropy fields. It is not possible to fit both the Mn1 and Mn2 frequency pulled lines with a model involving only uniaxial anisotropy. A plot of the predictions with uniaxial anisotropy ($B_A^+ = 0.35$ T and $B_A^- = 0$) is shown in figure 5.47.

Although the resonant lines measured experimentally are shifted downwards in frequency as a function of temperature, and the magnitude of the overall shifts agree well with the theory, there are several places where the model fails. The existence of four observed lines rather than two, the mechanism of absorption above 600 MHz, near the unpulled frequency, and the small temperature dependence of the unpulled frequency is not explained by our model.

Our model predicts the existence of an unpulled optical mode, but also predicts that this mode should not couple to the precessing magnetic field. We believe that our model correctly predicts the existence of this mode, but the absorption mechanism is lost due to the approximations made. The linearization procedure consisting of replacing I_i^z with its thermodynamic average, $< I^z >$ at each site in equations 5.118 and 5.119, and the artificial equivalence of the two Mn2 sites makes it impossible to predict an absorption mechanism for the optical mode.

If we do not treat each triplet of electronic spins as a single, S=5/2 spin, then we must

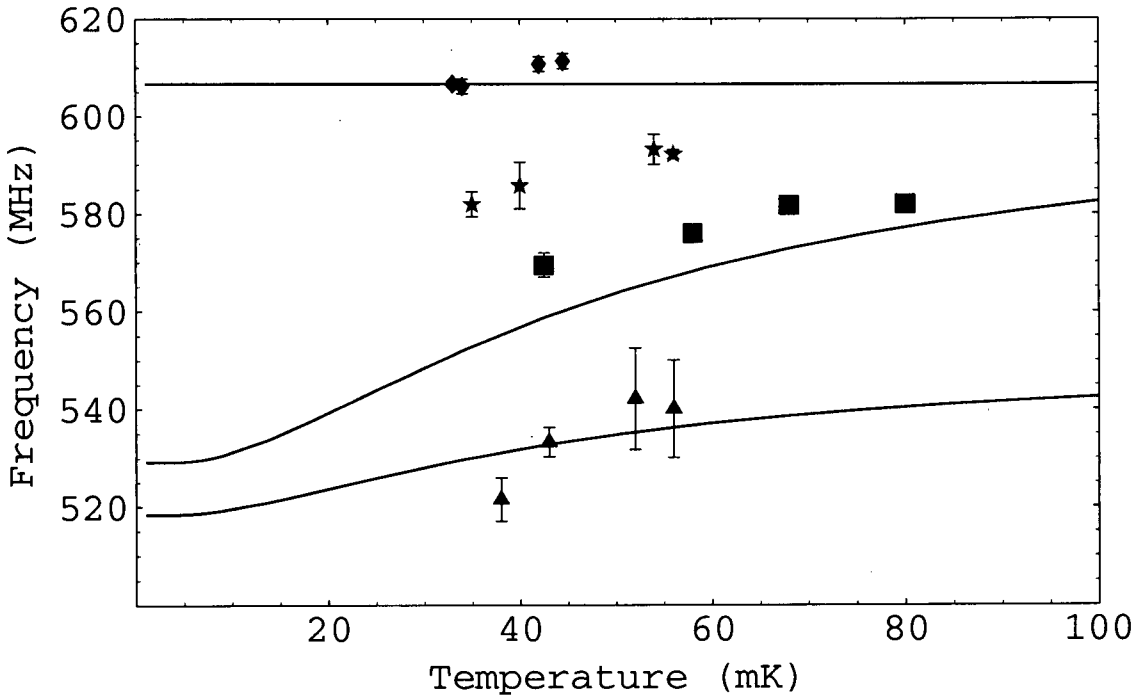

Figure 5.47: The spectrum of the zero momentum nuclear spin excitations as a function of temperature for uniaxial anisotropy ($B_A^+ = 0.35$ T and $B_A^- = 0$) and the data.

include 6 atoms per unit cell. There will then be 12 electronic magnon modes, and as many nuclear magnon modes. Of the nuclear magnon modes corresponding essentially to precession of the Mn2 spins, there will be 2 modes with all nuclear Mn2 spins in phase, 4 modes with Mn2 spins in opposition of phase within the same triplet, and 2 modes with Mn2 spins in phase within the same triplet but in opposition of phase with the other triplet in the same unit cell. It is important to note that a careful consideration of the crystal structure and the exchange and super-exchange bonds (see [16]) shows that each Mn2 spin is strongly coupled to two nearest neighbour triplets. The two nuclear Mn2 sites are then coupled differently to different electronic magnon excitations. Since the exact couplings between electronic spins within each triplet, and with nearest neighbour spins outside the triplet are not known, there are too many free parameters to make a full calculation worthwhile. However, these different couplings will clearly break down many of the symmetries in our model that prevent absorption of optical Mn2 line (presumably there will be some admixture of the Mn1 nuclear spin). A full calculation should also predict another excitation mode not presently seen in our model. This mode would correspond to the observed resonance that could not be fitted with our model. There could also be a small temperature dependence of the optical line.

Furthermore, there is the possibility of different anisotropy fields for each of the 6 ions. Crystal symmetries prevent different anisotropy fields for the two triplets in each unit cell, but it is very likely that the anisotropy fields for the Mn1 sites and the Mn2 sites are different. Again these parameters are not known. What has been measured previously [20] is the average anisotropy field over a triplet of ions.

There is the possibility that some of the observed structure is due to domains. The magnetic behaviour of MnAc at low temperatures has been extensively studied by SQUID magnetometry [15]. At very low fields ($B < 14$ mT), there exist mixed phases of ferromagnetic and antiferromagnetic alignment of the a-b planes. However, no domain structure

was observed at higher applied fields. In our experiment, the same line structure was observed at applied fields up to 110 mT, in two separate measurements. (Higher fields were not possible due to the increase in T_1.) Therefore, it seems unlikely that domains can account for the observed structure.

The exact power spectrum calculated for four spins gives a reasonable qualitative picture. It seems improbable that the number of lines in our spectrum is due to an enhanced pseudoquadrupolar splitting. On the other hand, our numerical results indicate that the linewidth and lineshape are strongly dependent on temperature even if the individual transitions cannot be observed. This could partly explain the asymmetry of the peaks observed and may introduce some error into the estimation of the centre frequency of the line.

In an effort to explain the fourth resonant line without calculating the electronic spectrum including all 6 ions per unit cell, we have applied the perturbation technique of Kubo and Tomita [8], where we regard a single ion Hamiltonian as unperturbed. In this approximation, it is necessary to identify the observed lines in the unperturbed Hamiltonian and the corrections to the positions of the lines can then be calculated. However, we are unable to account for the observed spectra by including the pseudoquadrupolar lines in the unperturbed Hamiltonian. There is no energy scale of the order of 10 MHz in the basic Hamiltonian except the symmetry breaking effect between Mn1 and Mn2. It is difficult, therefore, to account for four lines, separated by more than 10 MHz using this perturbative approach.

The MnAc crystal has low symmetry so that the hyperfine coupling constant might have some anisotropy which is also indicated by the relatively strong anisotropy fields. However, we expect the anisotropy to be small since the magnetic moment of Mn^{++} is spin only. The effect of anisotropy is essentially to include $I_i^+ I_j^+$ and $I_i^- I_j^-$ in the effective Hamiltonian. In other words it has the same effect as the anisotropy fields.

Since the hyperfine anisotropy should be small, we expect this to lead to small corrections. Demagnetizing effects can also yield $I_i^+ I_j^+$ and $I_i^- I_j^-$ terms, but the demagnetizing factor for the thin, planar shape is very small, and, in zero magnetic field, the antiferromagnetic coupling between different layers (in the a-b plane) ensures that no demagnetizing fields are present. Further, we observe no change in structure on applying a sufficiently large magnetic field to make the sample fully magnetic.

The nuclear spin in MnAc is large ($I = 5/2$), and it it seems reasonable to expect that spin wave calculations using the Holstein-Primakof transformation ($1/I$ expansion) should yield good results at low temperatures. Spin wave theory does indeed agree with our prediction at low temperatures. However, to treat the effect of higher temperatures using spin wave theory, it would be necessary to introduce coupling between the bosons, making the calculation difficult. Since the $T = 0$ results agree with our predictions, however, we have some confidence that our model is accurate.

5.9 Conclusion

We have measured the frequency pulling effect in MnAc. The temperature dependence of the frequency pulling could not be explained by a simple model assuming uniaxial anisotropy fields and no coupling between Mn1 and Mn2 spins. Furthermore, the experimental data shows a spectrum involving four resonance lines, rather than the expected two.

A model including coupling between all the nuclear spins and non-uniaxial anisotropy was developed. This model agrees well with the magnitude and temperature dependence of the frequency pulling and shows that it is highly sensitive to the strength of the anisotropy fields. Classical and quantum simulations support qualitatively the results of the calculations and a spin wave calculation, accurate at $T = 0$, agrees exactly with this

model at zero temperature.

The absorption of the unpulled optical mode, and the existence of another resonance mode (presumably mainly involving precession of the Mn2 spins) is lost in the approximation that each triplet of electronic spins behaves as a single, $S = 5/2$ spin. Although there are too many unknown parameters to make a full calculation worthwhile, it is clear that including the full electronic magnon spectrum will break many of the artificial symmetries that prevent absorption of the unpulled optical line, and the existence of another frequency pulled Mn2 resonance.

We believe, however, that the essential physics of the nuclear magnon excitations has been captured by the model. The model is also of interest in itself because it extends the theory of frequency pulling to cases with $I \geq 1/2$ where the self-interaction term is important and to cases where the crystalline anisotropy fields are not uniaxial.

Chapter 6

First NO of a radioactive isotope implanted in insulators

6.1 Introduction

The great majority of experiments exploiting the technique of on-line nuclear orientation (NO) of implanted isotopes have been motivated by nuclear or fundamental physics. All experiments to date have used a metallic magnetic material, usually an Fe foil, as the host. However, from the condensed matter point of view, there is a very wide range of magnetic insulators that would be interesting implantation targets and we decided to investigate the performance of these as hosts for on-line experiments. In this regard, we note that implantation of radioactive isotopes has been used to study the physics of semiconductors and insulating systems by the Mossbauer [30] and perturbed angular correlation (PAC) [31] techniques. Usually the experiments are performed off-line although there have been on-line measurements using PAC on, for example, high temperature superconductors [32]. For nuclear orientation, on-line measurements would open the door to many new experiments to investigate interesting magnetic structures. Although NO and NMR on oriented nuclei (NMRON) have many orders of magnitude more sensitivity than conventional NMR, it is often very difficult to obtain samples doped with a suitable isotope. This problem would be obviated if an isotope could be implanted in an on-line experiment. An insulating host may also, in specific cases, provide a larger hyperfine interaction than an Fe host.

In these first experiments to investigate the efficacy of the method, we chose to implant

^{56}Mn into antiferromagnetic crystals of $MnCl_2{\cdot}4H_2O$ and $CoCl_2{\cdot}6H_2O$. $MnCl_2{\cdot}4H_2O$ is antiferromagnetic below $T = 1.6$ K. The crystal structure is monoclinic with $\beta = 99.7°$ [33], and the magnetic easy axis (along which the magnetization is aligned in zero field) is close to the c-axis [34]. The magnetic properties have been studied by NO and NMRON using ^{54}Mn as the radioactive probe [35, 36, 37, 38]. In fact, it was the first insulating ordered magnet in which NMRON was successfully performed [35]. $CoCl_2{\cdot}6H_2O$ is also antiferromagnetic with a similar crystallographic structure, but with $\beta = 122.3°$ [39], and an ordering temperature of 2.3 K [40]. The easy axis of magnetization is the c-axis. In this case, the magnetism is more complicated with some orbital contribution. Previous NO studies have shown that a significant orientation of ^{54}Mn can be achieved by incorporating it as an impurity in the crystal [41]. The magnetism is close to "spin only" in these crystals and the hyperfine field is large with a value $B_{hf} \approx 60$ T.

Radioactive ^{56}Mn has spin $I = 3$, magnetic moment $\mu = 3.227\mu_N$, and a half-life $t_{1/2} = 2.6$ hr. It decays by β^- emission to the daughter ^{56}Fe and the γ-ray observed in the experiment is the E2 transition from the 2^+ 847 keV level to the 0+ ground state. Fig. 2.3 represents a simplified decay scheme in which only the β^- decays with intensities greater than 1 % and the subsequent γ-rays feeding to the observed 847 keV transition are shown.

The isotope ^{54}Mn, with $I = 3$, magnetic moment $\mu = 3.282\mu_N$, and a half-life $t_{1/2} =$ 303 d, was also utilized in these experiments. In this case, the decay to the daughter ^{54}Cr is by electron capture to the 835 keV level and the observed γ-ray is the subsequent E2 transition to the 0+ ground state. The decay scheme is shown in Fig. 2.2.

6.2 Sample Preparation and Experimental Procedure

Seed crystals were grown from saturated aqueous solutions of $MnCl_2 \cdot 4H_2O$ and $CoCl_2 \cdot 6H_2O$. The crystals were then grown from saturated solutions of the salts in a temperature controlled environment. The final crystals had an area of ~ 1 cm^2 and a thickness of ~ 0.2 cm. During growth, the $MnCl_2 \cdot 4H_2O$ crystal was doped with the radioactive isotope ^{54}Mn while the $CoCl_2 \cdot 6H_2O$ crystal was doped with both ^{54}Mn and ^{60}Co. These isotopes are long lived, have simple decay schemes and their γ-ray anisotropies were used both to ascertain the temperature of the crystals and to provide a comparison with the γ-ray anisotropy of the implanted isotopes.

A special sample holder was designed to clamp the crystal to the cold finger using Apiezon N grease yet allow ~ 1 cm^2 of its face to be exposed to the ion beam. The cold finger was "top-loaded" into the Louvain-La-Neuve dilution refrigerator [42], but, because the hydrated crystals deteriorate under reduced pressure at temperatures $T \geq 240$ K, the top-loading equipment was modified to enable the crystals to be pre-cooled before insertion into the dilution refrigerator. A ^{57}Co-Fe foil was also soldered to the cold finger in order to monitor its temperature. A magnetic field, B_0 was applied not only to magnetize the ^{57}Co-Fe foil, but also to reduce the nuclear spin-lattice relaxation time, T_1, of the Mn spins and so increase their rate of cooling.

The ^{56}Mn ions were produced at the CYCLONE cyclotron in Louvain-La-Neuve. A 100 MeV, 2.5 mA deuteron beam was directed on to a ^{55}Mn target foil mounted in an ion guide source. Reaction products recoiling out of the foil were thermalized in helium buffer gas at 200 mbar pressure inside the ion source. The positive ions leaving the source through the extraction hole were accelerated to 50 keV, mass separated and then transported to the dilution refrigerator where they were implanted at a rate $\sim 10^3$ s^{-1} into the crystal samples.

Germanium detectors were placed in various directions with respect to the crystalline axes to measure the intensities of the 835 keV γ-ray in the ^{54}Mn decay (electron capture to ^{54}Cr), the predominant 847 keV γ-ray in the ^{56}Mn decay, the 1173 keV and 1332 keV γ-rays for ^{60}Co (in the ^{56}Mn-$CoCl_2{\cdot}6H_2O$ experiment) and the thermometric 122 keV transition in the ^{57}Co decay. Pulser signals were also recorded in each detector to correct for electronic dead time and to check the stability of the data acquisition system. A magnetic field, B_0, was applied in a horizontal direction, and two high efficiency detectors mounted in the horizontal plane, counted radiation emitted parallel (detector 1) and perpendicular (detector 2) to B_0. A third, lower efficiency detector monitored counts in the vertical direction, i.e. perpendicular to B_0.

In order to analyse the Ge detector spectra, software was written that used a peak finding algorithm to track any changes in peak position due to gain changes. The peaks were then integrated and the background was subtracted using the average counts to the left and right of the peak. The pulser peaks were also integrated in this way, and the dead time corrections were made by dividing the areas of the peaks by the area of the pulser peaks. This software allowed the hundreds of spectrum files to be analysed easily.

In the first experiment, the $MnCl_2{\cdot}4H_2O$ crystal was oriented so that the crystalline c-axis, which is close to the magnetic easy axis, was horizontal. Thus the directions of the c-axis and the applied field, B_0, were parallel within the angular uncertainty of aligning the crystal that was $\pm 4°$. With this geometry, detectors 1 and 2 measured radiation emitted at angles $\theta_1 = 0°$ and $\theta_2 = 90°$ respectively. When ^{56}Mn was implanted into the sample, a problem was immediately encountered. The insulating crystals warmed up to $T \sim 100$ mK during the implantation process. This was not due to the deposition of energy by the implanted isotopes, but because of the exposure to thermal radiation down the side access. This problem was overcome because the half-life of ^{56}Mn (2.6 hr) allowed the experiment to be done pseudo-on-line in cycles. The detectors collected data

at all times, and in each cycle the following operations were performed:

- ^{56}Mn was first implanted into the crystal for a time $> \tau_{1/2}$ so that sufficient activity built up;
- The side access was closed and the system cooled for a time $> \tau_{1/2}$;
- The dilution refrigerator was warmed up to a temperature $T > 100$ mK to obtain "warm" counts for normalization.

The cooling of the crystal is limited by the extraction of the heat capacity of the abundant nuclear spins (^{55}Mn or ^{59}Co). There are two "bottlenecks": the Kapitza boundary between the crystal and the copper cold finger, and the nuclear spin-lattice relaxation characterized by a time T_1. In $B_0 = 0$, the cooling is initially limited by the Kapitza resistance, but as the temperature falls, T_1 increases exponentially [38] with an exponent proportional to (- E_g/k_BT) where E_g is the magnon energy gap. In order to increase the cooling rate one can utilize the "magnon cooling" effect [37]. B_0 is adjusted to a value very close to the "spin-flop" field, $B_{AE} \sim (2B_EB_A)^{1/2} \sim 0.7$ T, where B_A and B_E are the anisotropy field and exchange field respectively. This causes E_g to be decreased, at least for one branch of the magnons, and T_1 is much reduced.

In the second experiment ^{56}Mn was implanted into $CoCl_2 \cdot 6H_2O$ and measurements made using the same pseudo-on-line procedure discussed above. The same γ-rays were counted as in the $MnCl_2 \cdot 4H_2O$ experiment as well as the 1173 keV and 1332 keV transitions in the ^{60}Co decay. In this case, because of the way in which the crystal grew, it was fitted into the sample holder with the a-axis vertical. The b-axis was horizontal and perpendicular to B_0. Thus the angular directions of detectors 1 and 2 were 32° and 90° to the easy c-axis respectively assuming exact alignment of the crystal.

6.3 Results and Analysis

The ^{54}Mn nuclei sit at lattice sites in the crystal because the ions are incorporated into the crystals during their growth. The nuclei thus experience a unique magnetic hyperfine field, B_{hf}, and the normalized γ-ray intensity observed at angle θ to the magnetization axis at temperature T is given by equation 2.5 which can be written as

$$W(\theta)_{54} = 1 + \sum_{k=2,4} B_k U_k A_k Q_k P_k(cos\theta) \tag{6.157}$$

The A_k and U_k coefficients can be found in table 2.1. The Q_k are corrections for the solid angle subtended by the detectors and are $Q_2 = 0.820$ and $Q_4 = 0.490$ for the geometry used.

For implanted nuclei there is a possibility that not all of them go into lattice sites. In the case of metals (e.g. iron), this effect is usually taken into account by a simple, two site model which assumes that a fraction f of the ions experience the full hyperfine field B_{hf} and a fraction $(1 - f)$ feel zero field. Although the hydrated crystals used in these experiments have a more complicated crystalline structure, we assume the same model so that the normalized intensity γ-ray intensity for the ^{56}Mn nuclei is given by

$$W(\theta)_{56} = 1 + f \sum_{k=2,4} B'_k U'_k A'_k Q_k P_k(cos\theta) \tag{6.158}$$

In the ^{56}Mn decay scheme there are several preceding transitions feeding the observed 847 keV γ-ray and the NO parameters can be found in table 2.1.

Note that, even if the assumptions of the two site model are inappropriate, the factor f is still a useful parameter to describe the effect of implantation because it does describe the reduction in the γ-ray anisotropy, i.e.

$$f = \frac{W(\theta)_{56} - 1}{W(\theta)_{56,m} - 1} \tag{6.159}$$

where $W(\theta)_{56}$ is the observed intensity and $W(\theta)_{56,m}$ is the maximum intensity that would be observed if all the ^{56}Mn ions were at substitutional sites.

In experiments on nuclei with a long half-life it is usual to measure $W(0)$ and $W(90)$, by comparing cold counts to warm counts measured in directions along the quantization axis (0°) and perpendicular to it (90°) respectively. The effect of the decay of a short lived isotope can be obviated by measuring the ratio $\varepsilon(0,90) = W(0)/W(90)$ and comparing this ratio cold and warm.

6.3.1 ^{56}Mn-$MnCl_2{\cdot}4H_2O$ experiment

Figure 6.48 shows the results obtained from four successful implantation/cooling/warming cycles performed in the ^{56}Mn-$MnCl_2{\cdot}4H_2O$ experiment. In each cycle counts were taken at intervals of 300 s. The values of $W(0)/W(90)$ for ^{54}Mn and ^{56}Mn obtained from the cold counts were normalized against a weighted average from warm counts taken before and after the cooling to give the anisotropy $\varepsilon(0,90)$. In each separate run counts were averaged over five consecutive 300 s intervals and then the grand average for $\varepsilon(0,90)$ taken. The lowest value of $\varepsilon(0,90)$ for ^{54}Mn, about 0.87, corresponding to a temperature $T \sim 60$ mK, was obtained in ~ 3 hours. This temperature is a little higher than expected, but may have been due to extraneous heating of the crystal by thermal radiation from 4 K walls. It should be noted that even in off-line experiments with optimum heat shielding, an initial cooling of a $MnCl_2{\cdot}4H_2O$ crystal from 100 mK to a low temperature, e.g. 30 mK, takes many hours [37].

The ^{54}Mn data can be fitted by a curve calculated from equation 6.157 with an exponential dependence on time given by

$$\varepsilon(0,90) = 1 - 0.135\left[1 - \exp\left(-\frac{t}{\tau_1}\right)\right] \tag{6.160}$$

with the time constant $\tau_1 = 5500$ s. This is an effective relaxation time for the cooling

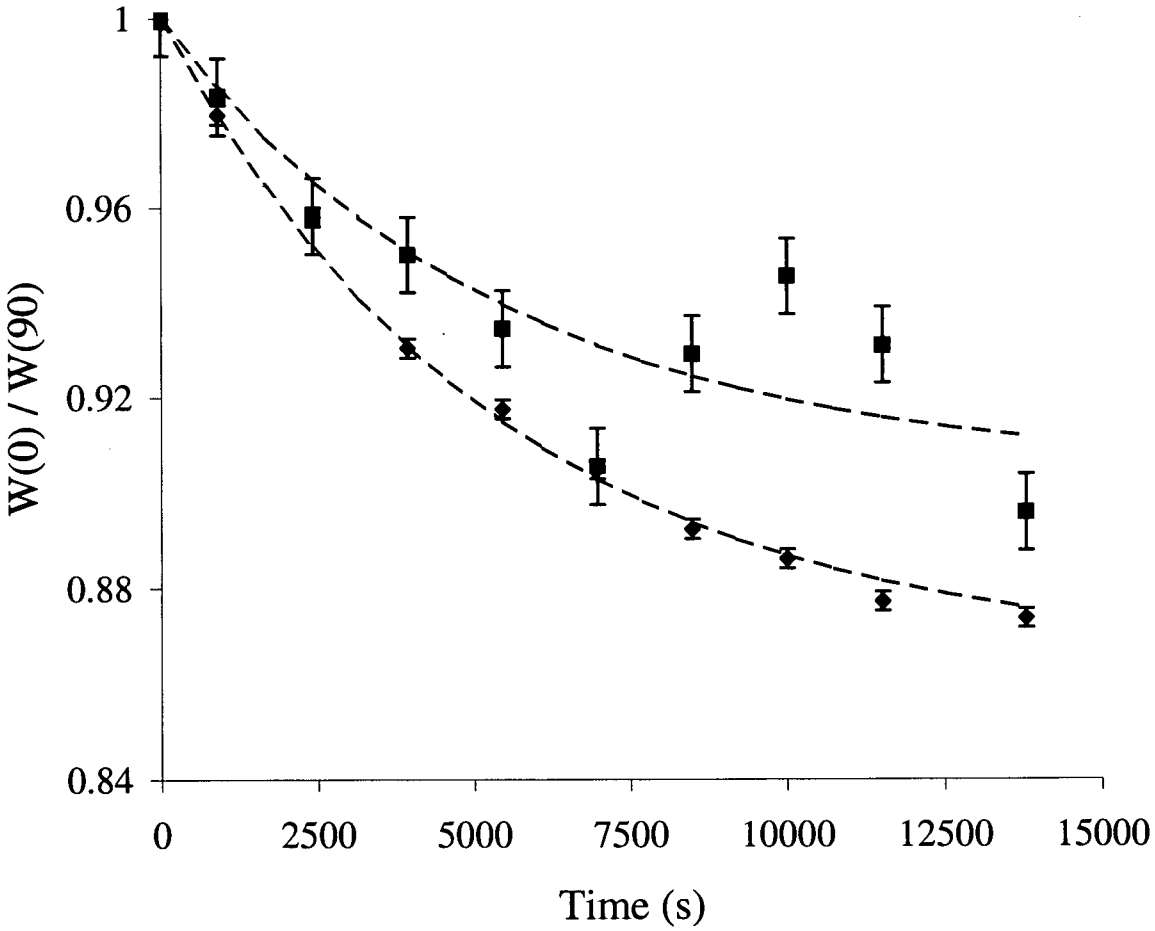

Figure 6.48: Variation of the γ-ray anisotropy, ε = W(0) / W(90), versus time for implanted ^{56}Mn (□) and ^{54}Mn (◇) in $MnCl_2 \cdot 4H_2O$ single crystal. The dashed curve through the ^{56}Mn data is calculated from the fit through the ^{54}Mn data that is a simple exponential decay described in equation 6.160, with $f = 0.96$.

which, as mentioned above, is limited by the Kapitza boundary and nuclear spin-lattice relaxation. A very rough estimate using $\tau_1 = R_K C$, where the Kapitza resistance R_K, for area A, is defined by $R_K A T^3 \sim 5 \cdot 10^{-3}$ $K^4 m^2 W^{-1}$ [43] and the thermal capacity C is given by $CT^2 \sim 5 \cdot 10^{-5}$ JK, gives a time constant of 3000 s at $T \sim 60$ mK for the crystal used, indicating that both bottlenecks are limiting the cooling. As well as the two bottlenecks, the spin-lattice relaxation involves the solution of a master equation that includes populations of the 2I+1 magnetic substates and the transition rates between them [2]. Thus the simple exponential behaviour described by equation 6.160 is very oversimplified because the actual relaxation process is quite complicated. However, the objective was to find a model that described the variation of the ^{54}Mn anisotropy with time in order to determine how the ^{56}Mn anisotropy changed. The dashed curve through the ^{56}Mn data was obtained by calculating the ^{56}Mn anisotropy from the ^{54}Mn curve (see figure 6.49) using equations 6.157 and 6.158 with a value $f = 0.96$,and assuming the same relaxation time, τ_1.

The comparison of $\varepsilon(0, 90)$ for ^{54}Mn and ^{56}Mn is shown in figure 6.49. A least squares analysis of the data gives the solid line corresponding to $f = 0.96^{+0.04}_{-0.07}$. The dashed line is for $f = 1$. The value obtained for f indicates that the occupancy of lattice sites by the implanted ions is very high in the two site model.

It should be noted that, even in metals, the two site model, which is generally used for the analysis of nuclear orientation data, is rather crude. Nuclei can end up in substitutional lattice positions, in interstitial sites (and perhaps there are more than one of these), or in positions damaged by the implantation process. Thus the nuclei might feel the full hyperfine field, a reduced one, or none at all. The structure of $MnCl_2 \cdot 4H_2O$ is more complex than a metal like iron so that there may be more non-substitutional sites. The $^{2+}$Mn ion has a half-filled 3d shell and "spin only" magnetism, but there are crystal field effects that reduce the hyperfine field from that expected for the free ion value [36].

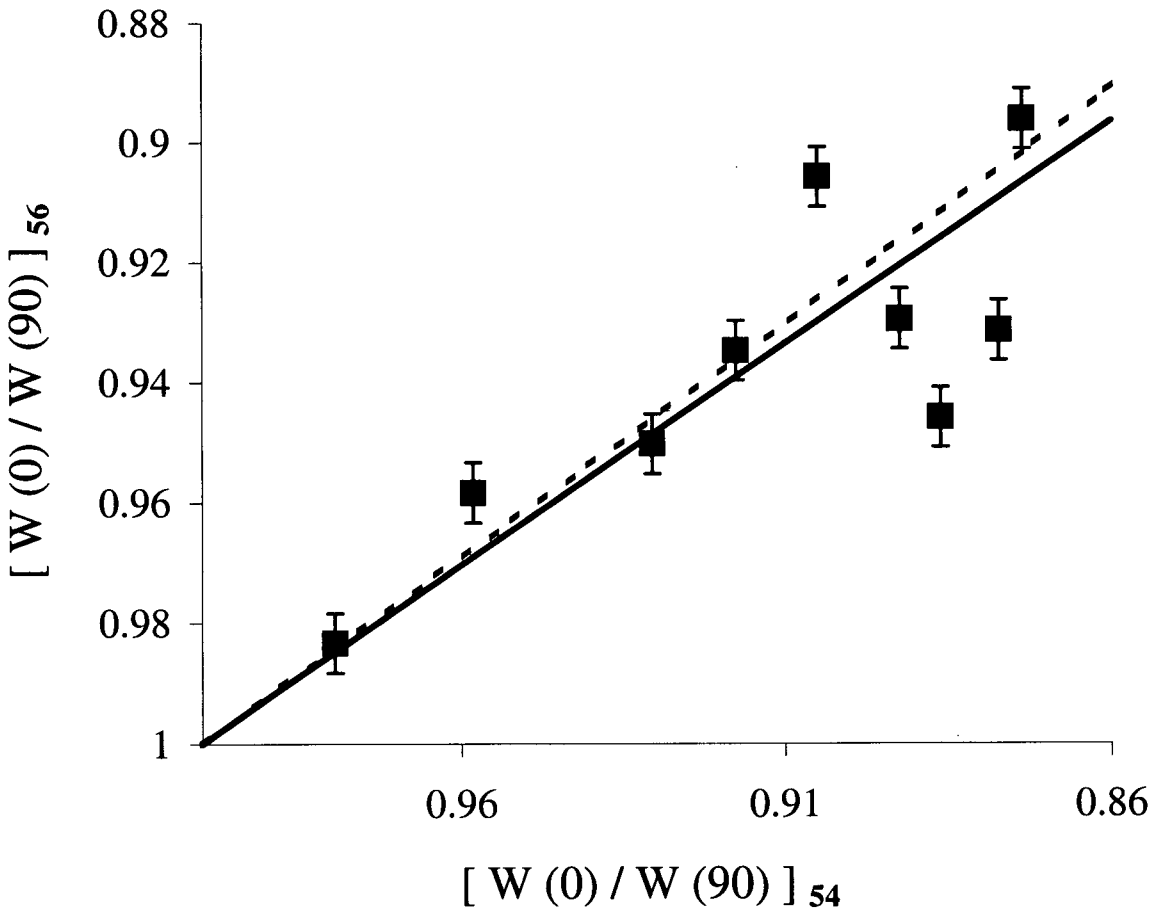

Figure 6.49: The comparison of the ^{56}Mn anisotropy $W(0)/W(90)$ with that for ^{54}Mn in $MnCl_2 \cdot 4H_2O$ single crystal. The solid line is the best fit to the data and corresponds to a value for the lattice site occupancy $f = 0.96^{+0.04}_{-0.07}$, i.e. close to unity. The dashed line corresponds to a value for the lattice site occupancy $f = 1$.

Therefore it is likely that the hyperfine interaction for non-substitutional Mn ions will be different from, but possibly close to, the full value. The observed anisotropy might be due to a majority of implanted ions in substitutional sites feeling the full hyperfine field and a few experiencing zero effect (two site model) or to many ions having a field slightly different from the full value. Future experiments using NMR experiments on the oriented nuclei (NMRON) should clarify the situation.

6.3.2 ^{56}Mn-$CoCl_2 \cdot 6H_2O$ experiment

These experiments were performed in $B_0 = 0.6$ T. Because of the alignment of the crystal, the magnetization is turned away from the easy axis towards the applied field as the latter is increased. We calculate, using the reported values for the exchange and anisotropy constants [44], that the electronic sublattice magnetizations are turned 4° towards the direction of B_0 that is also the direction of detector 1. In this case, the angular position for the horizontal detector 1, which was at 32° to the magnetization axis in $B_0 = 0$, would be $\theta_1 = 28°$ assuming exact alignment of the crystal. The orientation of detector 2 remained $\theta_2 = 90°$. The angle θ_1 can actually be determined from the ^{54}Mn data. The plot of the normalized intensities of the ^{54}Mn γ-rays measured in the two detectors is shown in figure 6.50 and the best fit to the data (dashed line) indicates that θ_1 was actually 27° instead of the calculated 28°, but this difference is well within the uncertainty in aligning the crystal. For the data analysis we used the measured value $\theta_1 = 27°$.

The average results for four successful implantation cycles are shown in figure 6.51. The final value of $\varepsilon(27, 90) = W(27)/W(90)$ corresponds to a lower crystal temperature of $T = 40(2)$ mK. The dashed curve through the ^{54}Mn is a fit using a double exponential function

$$\varepsilon(27,90) = 1 - 0.05\left[1 - \exp\left(-\frac{t}{\tau_2}\right)\right] - 0.15\left[1 - \exp\left(-\frac{t}{\tau_3}\right)\right] \qquad (6.161)$$

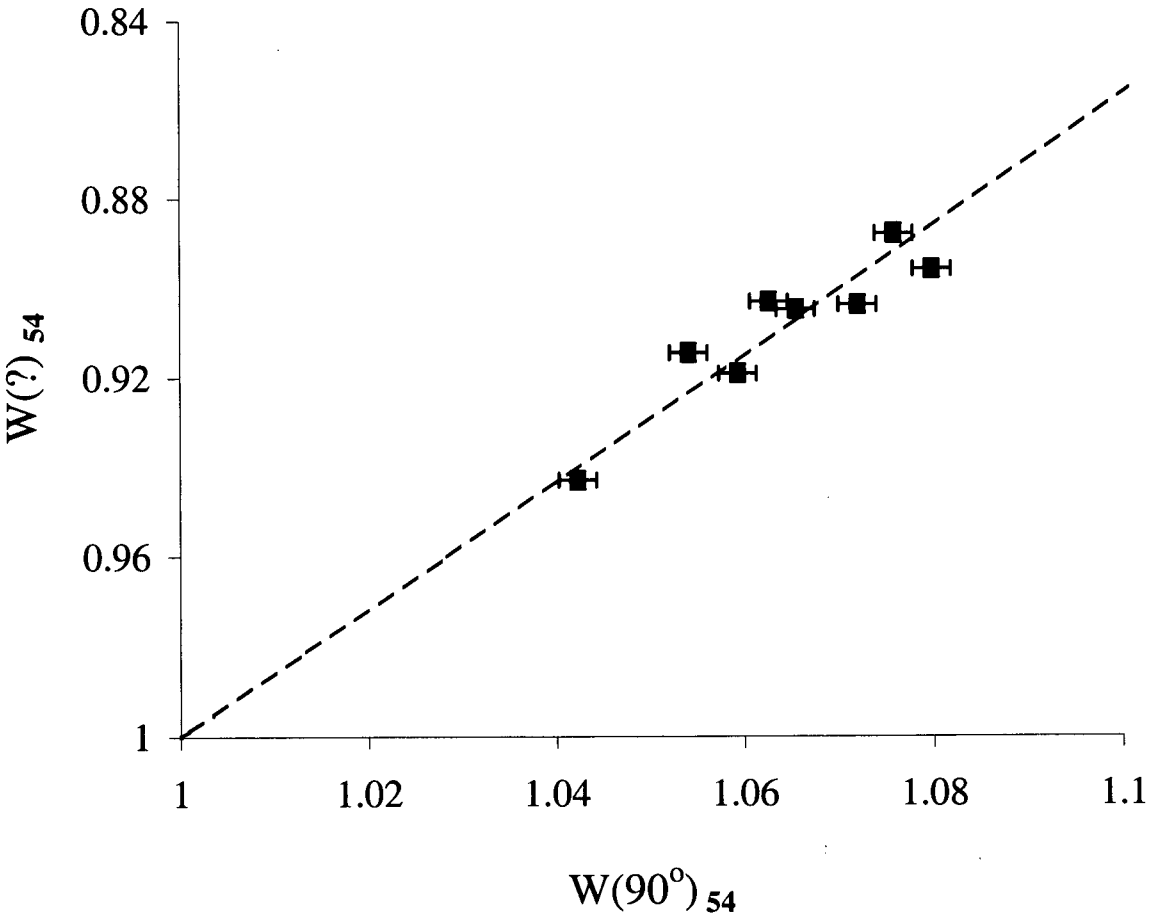

Figure 6.50: The plot of the normalized intensities for ^{54}Mn measured in the two detectors. Detector 2 is at an angle of 90° to the magnetization direction and therefore measures a normalized intensity $W2 = W(90)$. Because of the alignment of the $CoCl_2 \cdot 6H_2O$ crystal, detector 1 is at angle θ_1 to the magnetization direction, and the best fit to the data (dashed line) shows that $\theta_1 = 27°$ so that $W1 = W(27)$.

where τ_2 and τ_3 are 250 s and 4000 s respectively. This expression was chosen to fit the data, but the first term could be considered to represent the removal of ^{59}Co nuclear spin heat capacity (which is much smaller than for the ^{55}Mn heat capacity in $MnCl_2{\cdot}4H_2O$ because of the much smaller hyperfine field) while the second term is due to the nuclear spin-lattice relaxation (expected to be weaker for the same reason). The dashed curve through the ^{56}Mn data is then calculated from the fit to the ^{54}Mn data using equations 6.157 and 6.158 with a value for $f = 0.53$ estimated from the comparison of $\varepsilon(27, 90)$ for ^{54}Mn and ^{56}Mn shown in figure 6.52. The best fit for the data shown in figure 6.52 is obtained using $f = 0.53 \pm 0.10$.

There are various explanations for the smaller ^{56}Mn γ-ray anisotropy relative to that for ^{54}Mn in the $CoCl_2{\cdot}6H_2O$ experiment. Because the ^{56}Mn ions were implanted into a Co crystal host, it seems likely that fewer of them ended up in good lattice positions. The hyperfine field in interstitial sites may be less than in lattice sites. Also, the interstitial Mn spins may not have been aligned with the easy axis of the crystal. In each case, the average anisotropy of the γ-rays would be reduced.

Incident thermal radiation could also cause a temperature gradient across the crystal that has quite a low thermal conductivity. The ^{56}Mn are implanted only a few hundred Å into the surface and, therefore, might be at a higher temperature than the ^{54}Mn deep in the interior. However, this reduced effect in ^{56}Mn should then also be observed in the $MnCl_2{\cdot}4H_2O$ experiments. The quality of the surface might be a factor, and, indeed, the surface of the $MnCl_2{\cdot}4H_2O$ was visually better than that of the $CoCl_2{\cdot}6H_2O$ crystal so that in the latter there may have been a significant number of ions in damaged sites feeling a low or zero hyperfine field. Again, future experiments, measuring $W(\theta)$ vs T down to lower temperatures and performing NMRON would provide more precise information concerning these effects.

A very small value of $\varepsilon \sim 1\%$ was measured for the ^{60}Co indicating that the hyperfine

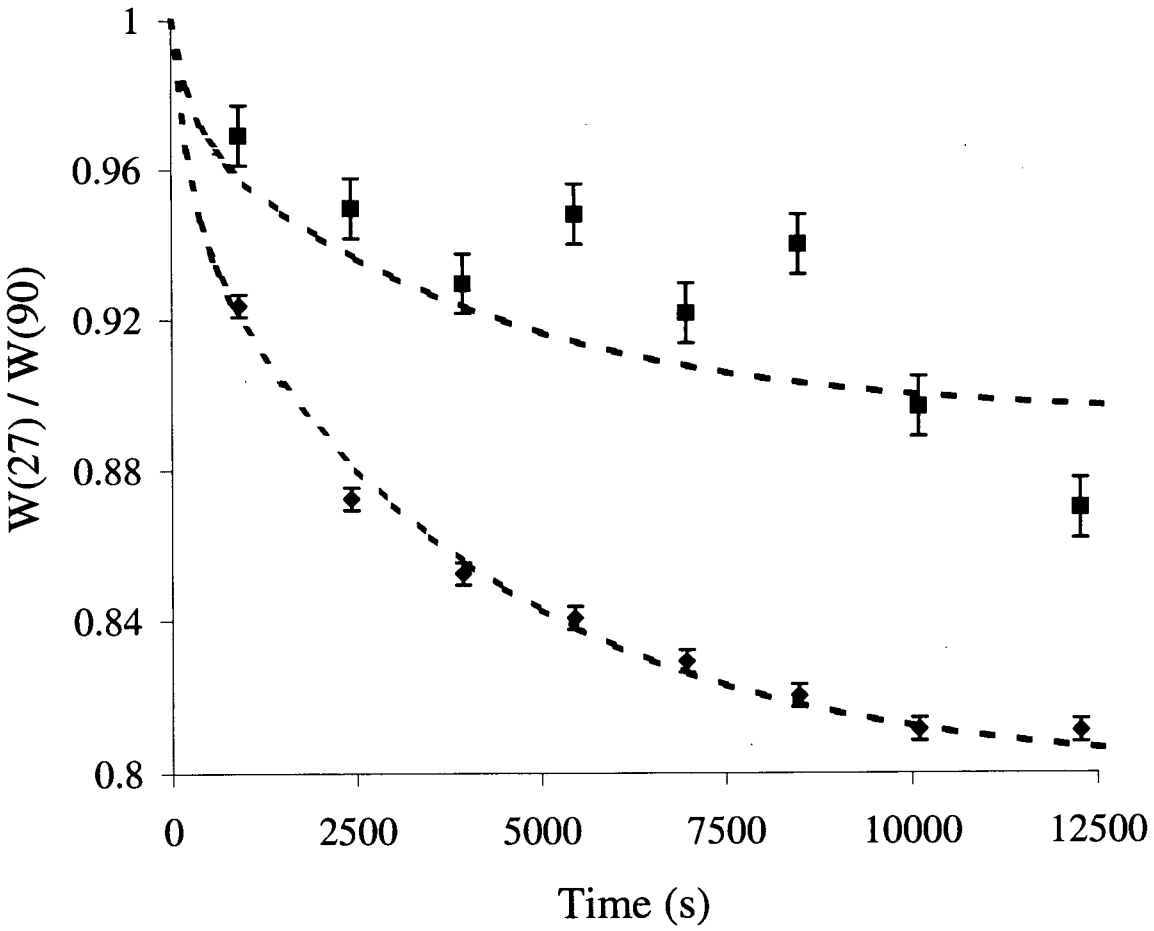

Figure 6.51: Variation of γ-ray anisotropy, $\varepsilon = W(27)/W(90)$, versus time for implanted ^{56}Mn (□) and ^{54}Mn (◇) in $CoCl_2 \cdot 6H_2O$ single crystal. The dashed curve through the ^{56}Mn data is calculated from the fit through the ^{54}Mn data that is the double exponential decay described by equation 6.161, with $f = 0.53$.

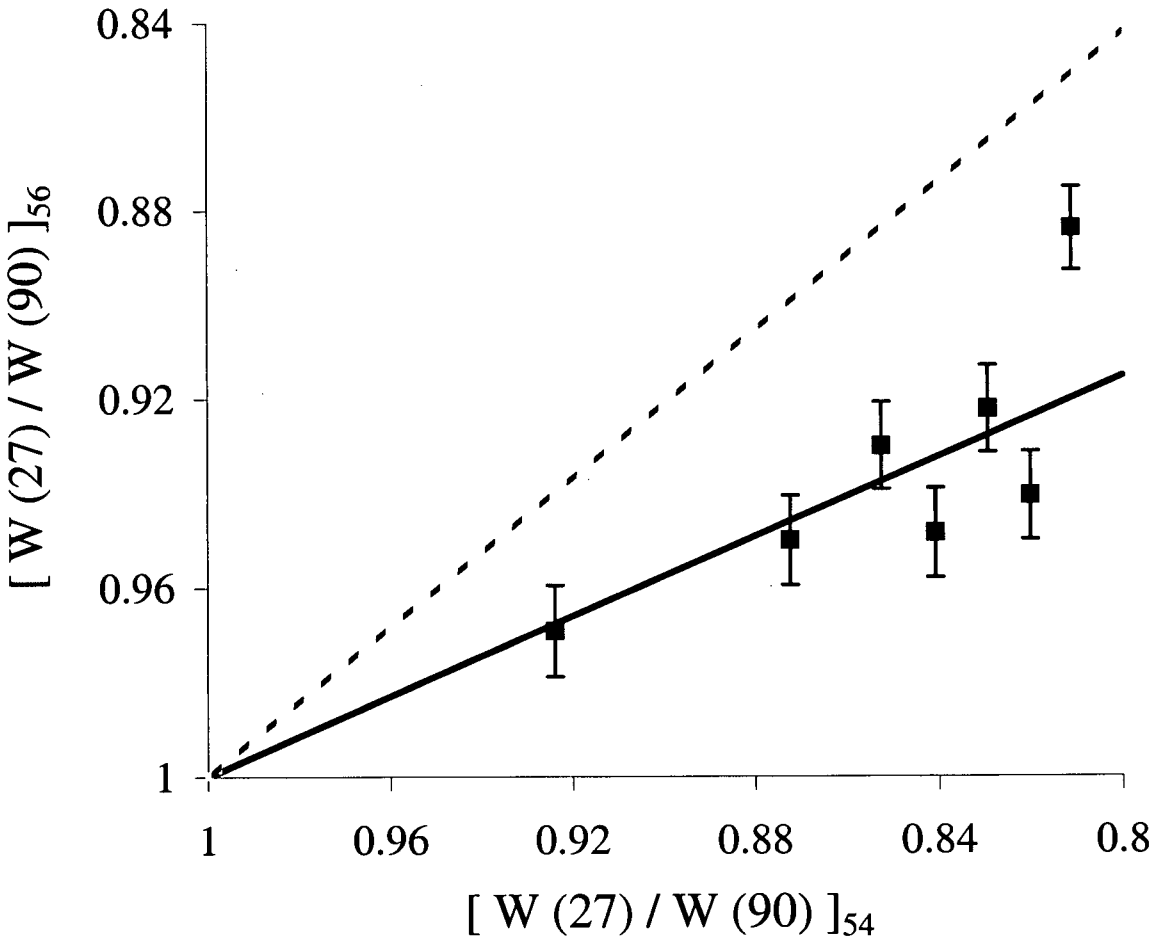

Figure 6.52: The comparison of the ^{56}Mn anisotropy with that for ^{54}Mn in $CoCl_2 \cdot 6H_2O$ single crystal for the data shown in figure 6.51. Because the last two points in fig. 6.51 have the same value of 0.811 for $[W(27)/W(90)]_{54}$, the average of the two $[W(27)/W(90)]_{56}$ values is taken to give the last point in this figure. The best fit is given by the solid line and gives a value of the lattice site occupancy $f = 0.53 \pm 0.10$. The dashed line corresponds to $f = 1$.

interaction in the cobalt atoms is quite small.

6.4 ^{104}Ag implantation

A further experiment to to implant ^{104}Ag into $MnCl_2 \cdot 4H_2O$ doped with ^{54}Mn was attempted, again at Louvain-La-Neuve. Unfortunately, due to experimental difficulties, only a short period of data could be obtained and in zero field. Without the benefit of a reduced T_1 due to "magnon cooling" the crystal could not be cooled enough to see anisotropy in the ^{54}Mn. It appeared, however, that there was a 2% anisotropy in one of the analysed ^{104}Ag γ lines. Subsequent careful analysis, using techniques that will be described in section 7.2, showed that the observed effect was due to a small drift in the position of the beamline. This could be determined by comparing areas of γ rays which should increase with areas which should decrease in the same detector. Although the experiment is inconclusive, it is important to note that beamline drift can be an important source of error if the detectors are close enough to the sample.

A future experiment using Ag as an impurity in $MnCl_2 \cdot 4H_2O$ is planned. The isotope ^{110m}Ag is suitable for growth into $MnCl_2 \cdot 4H_2O$ because the half life is 250 days. ^{110m}Ag is also a suitable isotope for NO because $\mu = +3.6\mu_N$, $I = 6$ and there are suitable γ-rays. Production of ^{110m}Ag is currently underway at TRIUMF.

6.5 Conclusions

Our experimental results demonstrate that radiation damage does not preclude significant γ-ray anisotropies being obtained after implantation into insulators. For ^{56}Mn implanted into $MnCl_2 \cdot 4H_2O$ an effect close to that for ^{54}Mn was observed, corresponding to $f = 0.96^{+0.04}_{-0.07}$ in the simple two site model. This value for f might also represent a large number of ^{56}Mn ions being in sites in which the hyperfine field is less but close to the

full substitutional value. It appears that the situation is similar to that in metallic hosts, in which there may be some radiation damage, but the final position of the implanted nucleus is not in the region of greatest damage. For ^{56}Mn implanted into $CoCl_2 \cdot 6H_2O$, the observed γ-ray anisotropy was significantly less than that for ^{54}Mn with $f = 0.53 \pm 0.10$. It is also shown that the long spin-lattice relaxation times that can occur in insulators does not prevent the nuclear orientation of implanted isotopes.

These experiments have demonstrated that insulators can be used as hosts for on-line experiments, at least for implanted isotopes with half-lives > 1 hr. Potentially, a new and exciting area for condensed matter physics has been opened up. Interesting magnetic structures which are difficult to dope could be studied by nuclear methods by implantation of a suitable isotope.

Chapter 7

Cobalt impurities in $MnCl_2 \cdot 4H_2O$

In order to use magnetic insulating crystals as hosts for the implantation of a variety of ions, it is important to understand the properties and effects of impurities. The implantation fractions measured in Chapter 6 of $f = 0.96^{+0.04}_{-0.07}$ for ^{56}Mn into $MnCl_2 \cdot 4H_2O$ and $f = 0.53 \pm 0.10$ for ^{56}Mn into $CoCl_2 \cdot 6H_2O$ indicate that the implanted ions find good lattice sites when they are the same element as the host crystal, but that a significant fraction do not when they are different. If NMR measurements are to be attempted on implanted isotopes it is important to understand the possible arrangements of the impurities in the lattice.

In order to investigate the effects of impurities, a series of $MnCl_2 \cdot 4H_20$ crystals were grown with Co impurities (see Table 7.3). ^{54}Mn was also included in the crystals for two reasons. Firstly, the temperature of the crystals could be monitored at all times. Secondly, the effects of the impurities on the NMR line of ^{54}Mn was studied.

crystal	^{54}Mn (μCi)	^{57}Co (μCi)	^{60}Co (μCi)	^{59}Co %
A	1.4	3.3	0	0
B	0.6	0	3	0
C	2.5	3.2	1.6	3.96

Table 7.3: The activities of the 3 crystals grown to investigate the properties of impurities in $MnCl_2 \cdot 4H_20$

7.1 Sample preparation and experimental details

Seed crystals of approximately 2 mm in length were grown from saturated aqueous solutions of $MnCl_2 \cdot 4H_20$ at room temperature. The seed crystals were then suspended in a saturated solution containing the radioactive isotopes and stable Co in a thermal bath maintained at a temperature of 30°C. As the water evaporated from the solution, the crystals grew to a size of 1-2 cm in length over a period of 12 to 24 hours. Finally, the crystals were suspended in a saturated solution of stable $MnCl_2 \cdot 4H_20$ in order to grow a layer of non-radioactive layer to protect from possible contamination of the apparatus by radioisotopes.

The smooth, (100) face of the crystal was cleaned by rubbing on a damp piece of filter paper. The crystal was then mounted with the (100) face in contact with the cold finger, in the SHE dilution refrigerator, as shown in figure 4.28. Apiezon N grease was used to improve the thermal contact, and the crystal was tied down tightly with unwaxed dental floss. The easily identifiable c-axis was mounted vertically. The easy axis of magnetization is at an angle $\Psi = 7°$ to the c-axis (towards the a-axis). In zero field, therefore, we measured the angular distribution of γ-rays, $W(7°)$, rather than $W(0)$. Prior to mounting the crystal, the copper cold finger was annealed overnight at 800°C under an atmosphere of hydrogen. The ^{60}Co in Fe thermometer was only mounted with crystal A for refrigerator diagnostics purposes.

The crystal was precooled to 240 K under an atmosphere of air because hydrated crystals deteriorate rapidly under reduced pressure at room temperature.

The RF coil used in this experiment was an untuned, single turn shown in figure 3.17, with $R_1' = 60\ \Omega$ and $R_2' = 60\ \Omega$. The capacitance, C', came from capacitance between the coil and ground and was less than 1 pF. No stabilization was used, although the cold finger resistor, which is extremely sensitive to direct RF heating was monitored at all

times to ensure that RF power was being received by the sample. The typical voltage settings were $|v_g| = 400$ mV. This corresponded to a current through the coil of ~ 1.3 mA and, using equation 3.57, the oscillating field was ~ 1.6 mG. This field is similar to employed in previous NMR experiments on $MnCl_2 \cdot 4H_20$ [37].

Measurements were taken with either 2 NaI detectors at 7° and 90° to the easy axis, or with 1 Ge detector at 7° to the easy axis. In general, the high resolution Ge detector was used for NO measurements, while the higher efficiency NaI detectors were used for NMR. All results for ^{57}Co were obtained with the Ge detector since the 122 keV and 136 keV γ-rays cannot be resolved with the NaI detectors.

7.1.1 Stable Co

Crystal C (see Table 7.3) was grown with a fraction of stable ^{59}Co. This fraction can be precisely determined because the crystal was also grown with ^{60}Co and ^{57}Co.

A solution was prepared with 13.1586 g of $MnCl_2 \cdot 4H_20$ and 0.8330 g of $CoCl_2 \cdot 6H_2O$. The total number of Mn and Co ions in solution is then

$$\begin{aligned} N_{Mn} &= \mathcal{N}\frac{13.1586}{55 + 2 \cdot 35.45 + 4 \cdot 2 + 4 \cdot 16} = 6.649 \cdot 10^{-2}\mathcal{N} \\ N_{Co} &= \mathcal{N}\frac{0.8330}{59 + 2 \cdot 35.45 + 4 \cdot 2 + 6 \cdot 16} = 3.561 \cdot 10^{-3}\mathcal{N} \end{aligned} \tag{7.162}$$

where $\mathcal{N}$ is Avagadro's constant. The fraction of Co ions in solution is

$$\frac{N_{Co}}{N_{Mn}} = 5.356 \cdot 10^{-2} \tag{7.163}$$

The fraction of Co atoms in the crystal is certainly less than the fraction of Co ions in the master solution. The fraction of Co ions that grow into the crystal can be calculated based on the activities of the radioactive isotopes in the crystal.

The activity of the original master solution and the final crystal were counted for a 1000 s live time at 50 cm from the Ge detector. The background counts were subtracted

and the counts from the 122 keV line of ^{57}Co and the 1173 keV and 1330 keV lines of ^{60}Co were added together to find an overall fraction of Co that grew into the crystal. The fraction of ^{54}Mn was calculated from the 835 keV line. The results are shown in Table 7.4.

Isotope	fraction %
^{54}Mn	4.49 ± 0.04
total ^{57}Co and ^{60}Co	3.32 ± 0.02

Table 7.4: The fraction of each isotope in solution which grows into the crystal.

The ratio of ^{59}Co in the crystal is then

$$\frac{N_{Co}}{N_{Mn}} = r = \frac{3.32}{4.49} 0.0536 = (3.96 \pm 0.04) \cdot 10^{-2} \tag{7.164}$$

Since each Mn ion has 6 nearest neighbours, the probability $p(n)$ of an Mn ion having n nearest neighbour Co ions is

$$p(n) = r^n (1-r)^{6-n} C_6^n \tag{7.165}$$

if the Co ions grow into substitutional lattice positions. In this case, $p(1) = 0.19$, while $p(2) = 0.02$. If the Co ions sit at substitutional lattice sites, and have an effect on the hyperfine field at neighbouring Mn sites, we would expect to see a satellite line approximately 1/4 the intensity of the main ^{54}Mn resonance line.

7.2 Data collection and analysis

The data were collected on 2 PCs as shown in figure 7.53. Four single channel analysers (SCA) were used to monitor the ^{54}Mn NMR resonances. A multichannel analyser (MCA) was used while searching for ^{57}Co and ^{60}Co resonances, and when collecting data for detailed NO measurements. Although both systems were employed in parallel, it was important to to set the window positions and widths on the SCAs several times because

the input impedance of the SCA changes with each position and width setting. Once the desired windows were achieved, the stability of the gain was monitored on the MCA.

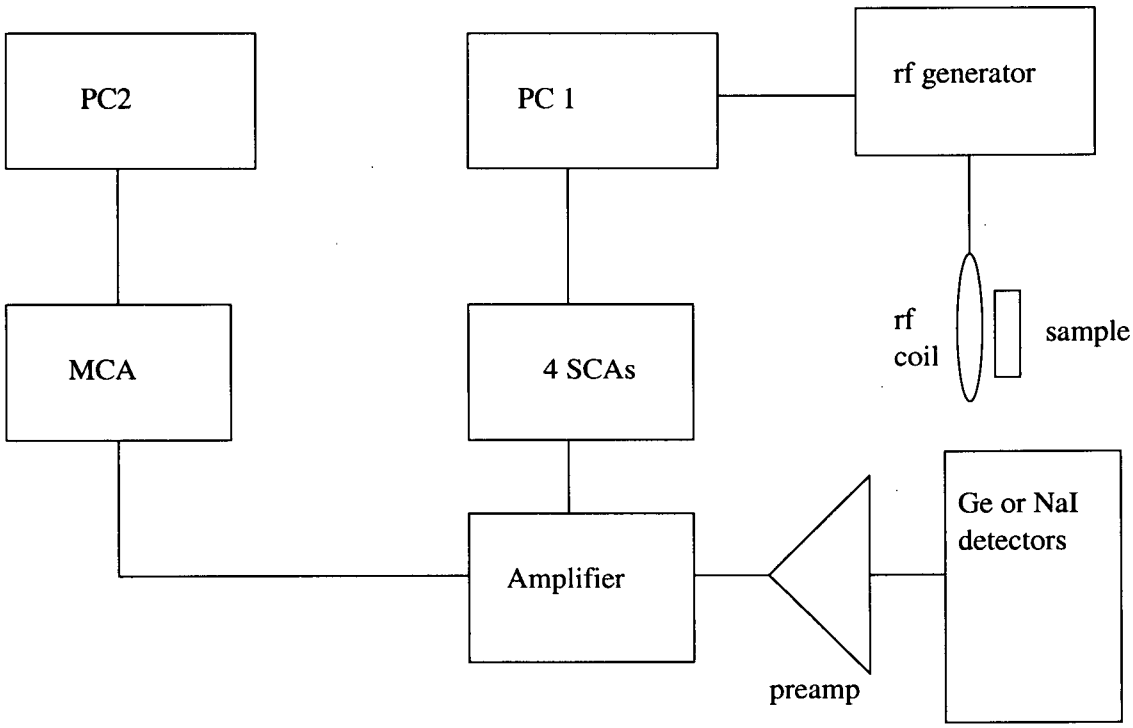

Figure 7.53: Data collection setup.

Data from the MCA was typically collected over 1000 s live time intervals. The Ortec software supplied with the MCA could output a list of peak positions and intensities. Since hundreds of spectra were collected, a programme was written to read these files, extract the necessary peak information collect it into a single file.

However, it was found that the Ortec software did not perform the best possible fitting, particularly for the low energy ^{57}Co γ-rays where background subtraction is extremely important. Therefore, software was written to analyse the spectrum data directly. The

method employed was a χ^2 fit, with an asymmetric Gaussian fitting function given by

$$y = \begin{cases} k + mx + A \exp\left[\frac{(x-p)^2}{\sigma_l^2}\right]; & x < p \\ k + mx + A \exp\left[\frac{(x-p)^2}{\sigma_r^2}\right]; & x > p \end{cases} \tag{7.166}$$

where k, m, A, p, σ_l and σ_r are parameters of the fit. The minimization of χ^2 was performed with MINUIT, and the results of several hundred spectra could be fit in less than one minute. The areas of the lines were calculated using several techniques, the results of which were then compared:

- Area $= \sqrt{\pi} A \frac{\sigma_l + \sigma_r}{2}$
- Integration over a fixed window, or integration over a fixed width window centered at p.
- Integration over a window centered at p with baseline subtraction using k and m
- Integration over a window centered at p with linear subtraction based on the average counts in fixed windows to the left and right of the line.

Although it is customary to fit Ge detector data with skewed Gaussians, it was found the fitting with asymmetric Gaussians gave comparable results while being simpler to implement numerically.

The accuracy of the results were tested by comparing the various techniques to a series of warm count spectra (typically around 100). Although the average counts found by each technique were consistent with each other, it was found that the smallest variance was obtained with a calculation based on the Gaussian fit parameters in the case of Ge detector data. In this case, k and m are strongly correlated with each other (because the background is almost constant), but very weakly correlated with the Gaussian fit parameters A, p, σ_l and σ_r because the lines are extremely narrow (σ_l and σ_r are on the

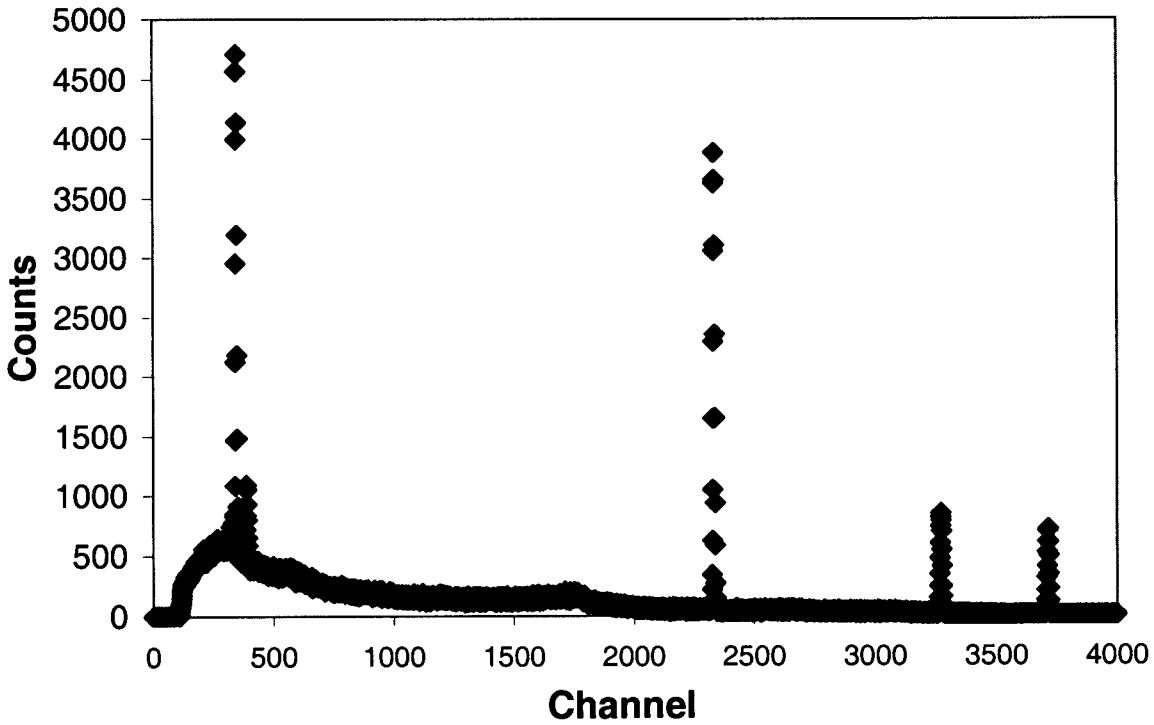

Figure 7.54: The full Ge detector spectrum for crystal C.

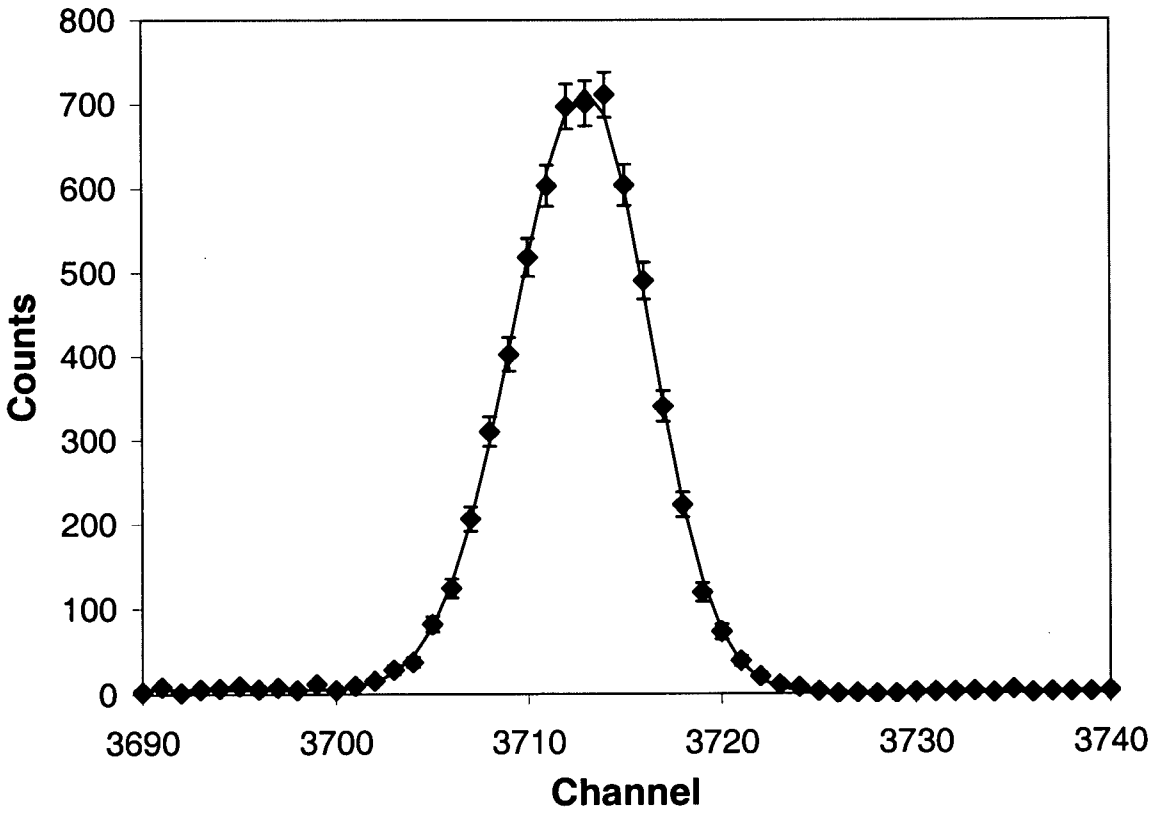

Figure 7.55: The Ge spectrum for the 1330 keV ^{60}Co line. The line is the best fit to the data.

order of 2 keV). Therefore, the area calculated from the Gaussian fit parameters gave excellent results.

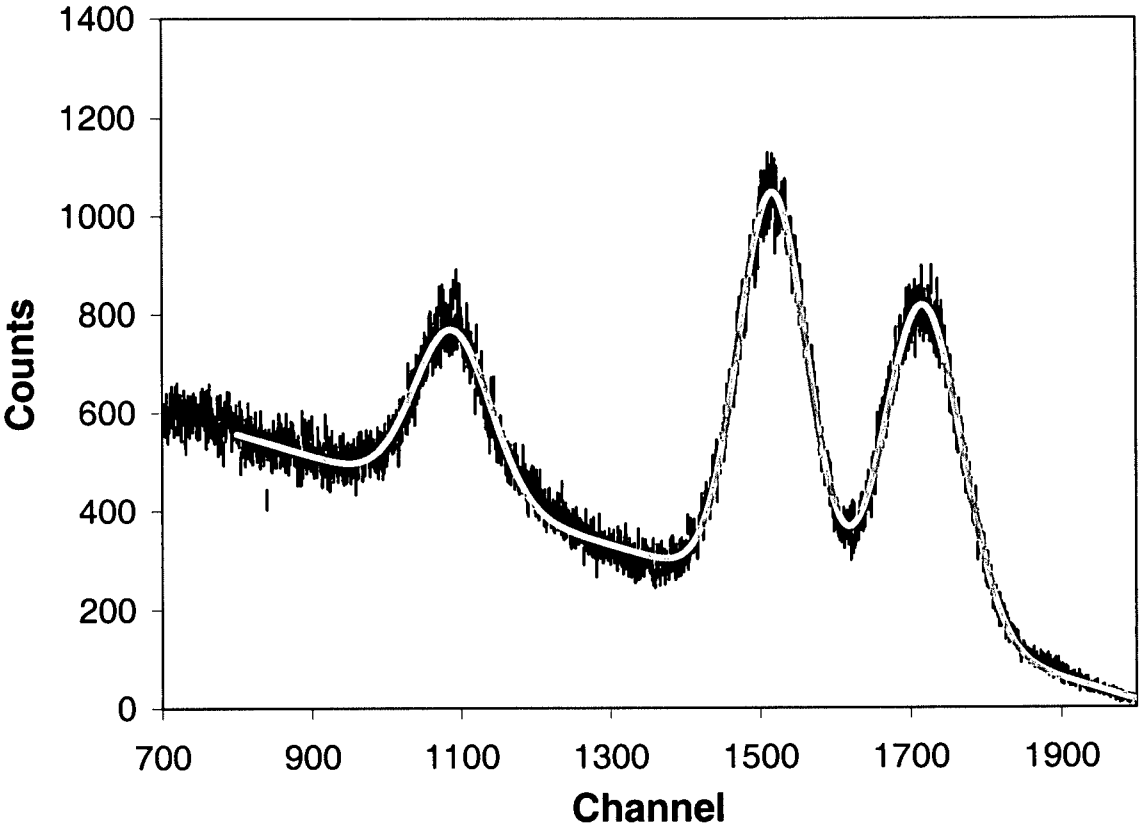

Figure 7.56: The full spectrum for the NaI detector for crystal B. The gray line is the best fit.

In the case of the NaI detectors the best results were obtained with a fixed-width window centered at p. The reason is that the NaI lines are extremely broad (on the order of 100 keV), and the parameters k, m, A and σ_l and σ_r become more strongly correlated. Using only the Gaussian parameters to calculate area then introduces more errors. Since p is, in all cases, very weakly correlated with the other parameters and has a very small uncertainty (less than 0.1 keV), the fixed window centered at p was the best choice. A fixed window alone did not give good results because of the drift in gain over time of the NaI detector setup. The baseline was not subtracted from the NaI spectra since they

were only being used in the search for NMR resonances. Background subtraction would have only folded errors in k and m into the results.

7.3 NO Results

In order to make use of the "magnon cooling" [37] effect to cool the crystals, a field of 0.72 T was applied. This is the field at which the spin-flop transition of $MnCl_2 \cdot 4H_2O$ occurs [37, 41] and T_1 is dramatically reduced. The precise field needed to induce the spin-flop transition in a given experiment depends on the exact orientation of the crystal. The initial cooling of the crystal was performed in a field $B_0 \simeq 0.7$ T, and the value of $W(0)$ as a function of time is shown in figure 7.57. The current in the superconducting magnet was then increased slowly to determine the field at which the spin flop transition occurred. The transition can be seen in figure 7.58 where $W(0)$ is plotted as a function of the current in the superconducting magnet. Currents of 6.35 A were subsequently used to provide the optimum magnetic field for cooling the crystal.

The final results of NO for the three crystals are given in table 7.5. The data were obtained from warm and cold counts in zero applied field. The counting times ranged from 27000 s to 85000 s. The data were collected on the MCA every 1000 s. Each 1000 s of data were analysed using Ortec's software and, independently by fitting with asymmetric Gaussians using MINUIT as described in section 7.2. This was necessary to ensure that that there was no change in counts for the duration of each collection period. The total counts were then the sum of the results of each of the 1000 s fits. As a final verification, all the 1000s spectra for each run were added together and fit with asymmetric Gaussians. It was found that the anisotropy calculated by each of the three methods consistently agreed within 1 σ statistical error for the ^{60}Co and ^{54}Mn lines. The comparison of the ^{57}Co did not always agree so well due to the important contributions of the background

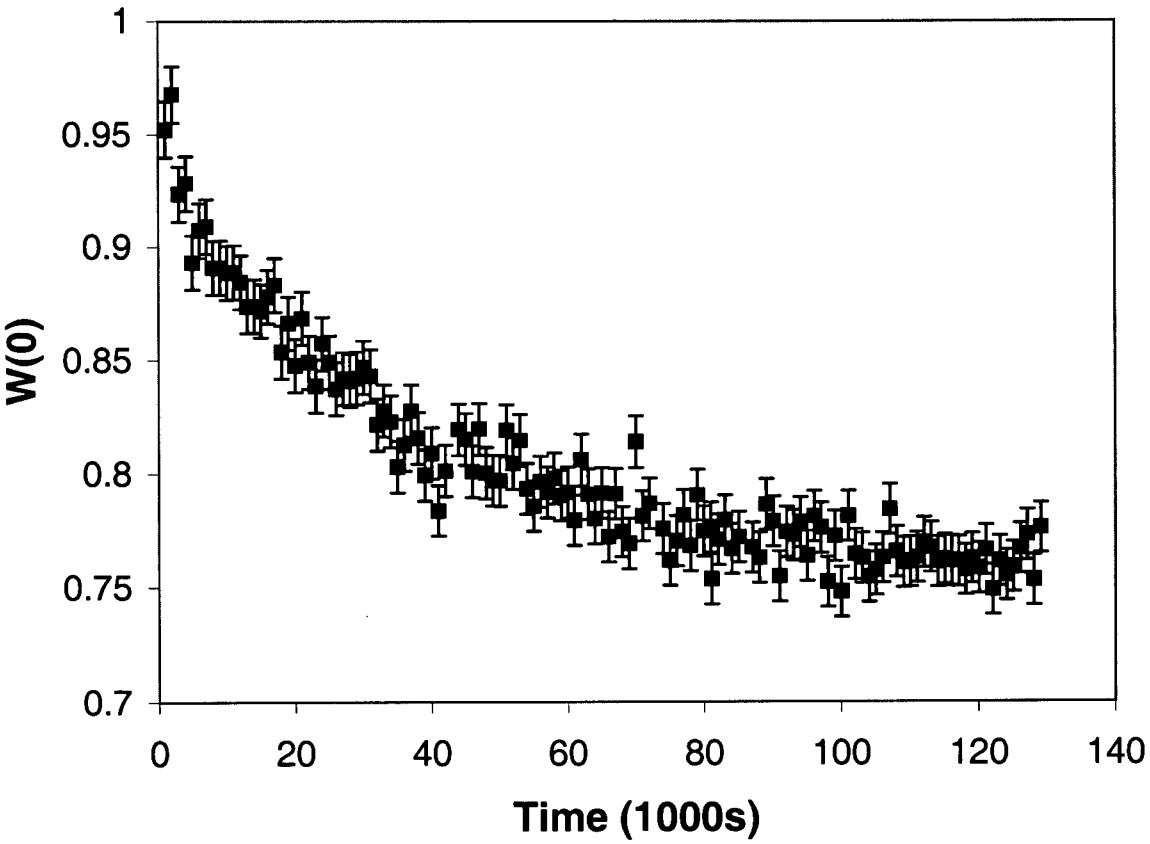

Figure 7.57: $W(0)$ as a function of time, showing the initial cooling of the entire crystal.

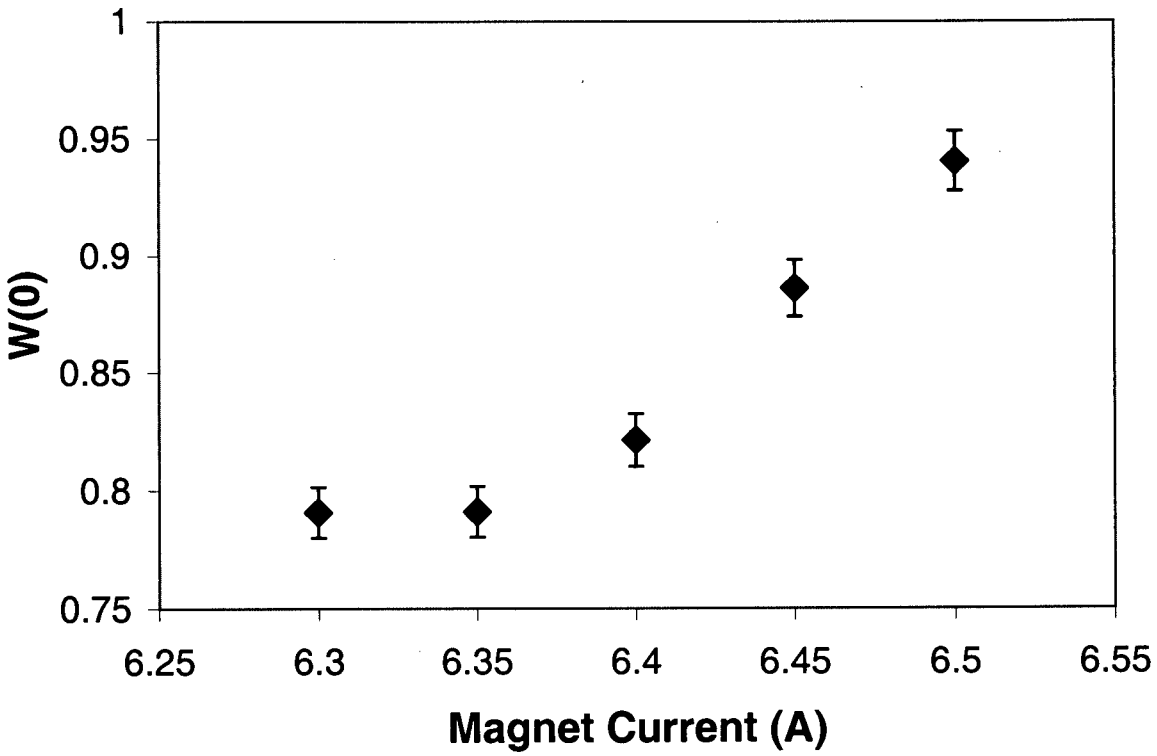

Figure 7.58: $W(0)$ as a function of the current in the superconducting magnet. The spin-flop transition begins at approximately 6.35 A. The transition is broadened by domain effects.

at low energies. The background is due to 2 sources: Compton scattering from the higher energy γ-rays, and electrical noise. The Compton background changed when the anisotropy of the higher energy γ-rays increased - particularly the ^{54}Mn contribution which displayed the largest anisotropy. This is an issue when performing NO, although it is a less important concern when performing NMR on ^{57}Co because the Compton background does not change in that case. The contribution from low energy electrical noise is essentially impossible to control and predict. It varies with the time of day, and with the activities of other experimentalists in the building. Changes in the background did affect the measured fits. Careful comparisons with the three fitting techniques, and with skewed Gaussian fits, showed that the statistical errors were larger than predicted by the errors in fitting parameters. It was found that a realistic assessment of the systematic errors on the anisotropy for the NO results was approximately 1% for both the 122 keV and 136 keV γ-rays. This 1% error is used as to calculate the errors on the hyperfine field. Unfortunately, it meant that the 122 keV γ-ray of ^{57}Co was useless for calculating a hyperfine field, since the total expected effect at the temperatures achieved was approximately +1%.

The base temperature of each crystal was calculated from the NO results of the ^{54}Mn, the hyperfine field of which is known precisely. The anisotropy of the ^{54}Mn was monitored over time throughout the measurements to ensure that this base temperature did not change. The hyperfine fields of ^{57}Co and ^{60}Co were calculated by comparing the measured anisotropy with that calculated from the NO parameters. The results of the 1170 keV and 1330 keV γ-rays were averaged to find the hyperfine field for ^{60}Co. The 136 keV γ-ray was used to determine the hyperfine field for ^{57}Co. In Crystal A, the hyperfine field is 15.5 ± 2 T for ^{57}Co. In crystal B, the hyperfine field is 29.1 ± 0.5 T for ^{60}Co. In crystal C, the hyperfine fields are 15.6 ± 2.7 T and 25.6 ± 0.4 T for ^{57}Co and ^{60}Co respectively. The base temperatures and hyperfine fields calculated for each

crystal	isotope	γ energy (keV)	$W(7°)$
A	^{57}Co	122	$0.999 \pm 0.01(0.001)$
	^{57}Co	136	$0.956 \pm 0.01(0.003)$
	^{54}Mn	835	0.743 ± 0.002
B	^{54}Mn	835	0.812 ± 0.004
	^{60}Co	1170	0.944 ± 0.002
	^{60}Co	1330	0.946 ± 0.002
C	^{57}Co	122	$1.021 \pm 0.01(0.001)$
	^{57}Co	136	$0.970 \pm 0.01(0.003)$
	^{54}Mn	835	0.811 ± 0.001
	^{60}Co	1170	0.955 ± 0.002
	^{60}Co	1330	0.958 ± 0.002

Table 7.5: The nuclear orientation results for the 3 crystals The statistical errors are given from the fit parameters except for the 122 keV and 136 keV lines in which case a systematic error of 0.01 is assumed and the statistical errors from the fit parameters are given in parentheses.

crystal	Temp. (mK)	isotope	γ energy (keV)	Hyp. field (T)	$\mu B/hI$ (MHz)
A	$36.0 \pm 0.2^{+0.7}_{-2.0}$	^{57}Co	136	$15.5 \pm 2.0^{+0.1}_{-0.3}$	$159 \pm 20^{+1}_{-3}$
B	$44.4 \pm 0.6^{+0.7}_{-2.1}$	^{60}Co	1170	$29.3 \pm 0.7^{+0.1}_{-0.3}$	$170 \pm 4^{+1}_{-2}$
		^{60}Co	1330	$28.8 \pm 0.7^{+0.1}_{-0.3}$	$167 \pm 4^{+1}_{-2}$
		^{60}Co	avg(1170+1330)	$29.1 \pm 0.5^{+0.1}_{-0.2}$	$169 \pm 3^{+1}_{-1}$
C	$44.3 \pm 0.2^{+0.7}_{-2.1}$	^{57}Co	136	$15.6 \pm 2.7^{+0.1}_{-0.1}$	$160 \pm 28^{+1}_{-1}$
		^{60}Co	1170	$26.0 \pm 0.6^{+0.1}_{-0.3}$	$151 \pm 3^{+1}_{-2}$
		^{60}Co	1330	$25.1 \pm 0.6^{+0.1}_{-0.3}$	$145 \pm 3^{+1}_{-2}$
		^{60}Co	avg(1170+1330)	$25.6 \pm 0.4^{+0.1}_{-0.2}$	$148 \pm 2^{+1}_{-1}$

Table 7.6: The base temperature and hyperfine fields for the 3 crystals. The first error given is statistical. The second is the systematic error due to possible misalignment of the crystal. A possible misalignment of 7° was used to calculate the systematic error. The error on the 136 keV line is purely systematic: the first error is from the 1% systematic error in the detectors (the statistical errors in the detector are negligible compared to the systematic error) and the second is from the misalignment of the crystal.

observed transition (except the 122 keV line) in each crystal are shown in table 7.6, as well as the frequency (in MHz) at which an NMR resonance would be expected. The first error reported is statistical. The second is systematic and is calculated based on a possible 7° misalignment of the crystal.

The discrepancy between the ^{57}Co hyperfine field and the ^{60}Co hyperfine fields is most surprising. There are several possible explanations but none are entirely satisfactory:

- It is possible that the Co impurities do not grow substitutionally into the lattice, but into a variety of lattice positions, and experience a variety of hyperfine fields. The relative occupancy of each different site could depend on the particular growth conditions. However, it is difficult to understand the results of crystal C with those of A and B, since crystal C shows different hyperfine fields for the different isotopes in the same crystal.

- It is possible, but unlikely, that the occupancy of particular sites could be strongly affected by the different mass of each isotope.

- It is possible, but unlikely, that the Co magnetization is not aligned with the Mn, and the anisotropy is being measured at some very different angle than 0°.

- If strong electric field gradients were present, a strong quadrupole interaction might explain these results. However, the relatively weak quadrupole moments involved ($Q = +0.44 \pm 0.05$ b for ^{60}Co and $Q = +0.52 \pm 0.09$ b for ^{57}Co) make this an unlikely explanation.

- Finally, it has been observed by NMR, that the same isotopes of Fr in Fe experience a different hyperfine fields [45] and these fields can vary by as much as a factor of two, but it seems highly unlikely that Co isotopes should experience similar effects.

This discrepancy is certainly worthy of further study.

7.4 NMR results

7.4.1 Determining RF power

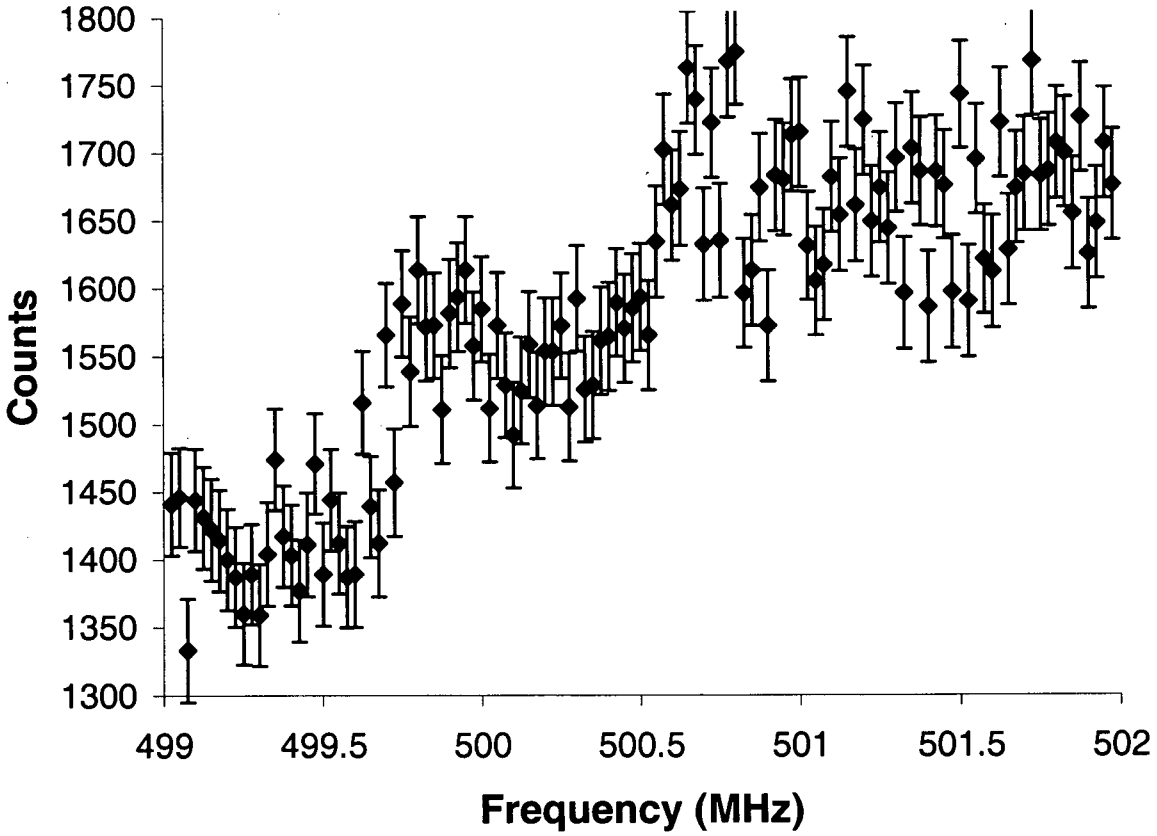

Figure 7.59: The number of counts at 0° as a function of frequency showing the ^{54}Mn resonance in an applied field of 0.2 T. The data were collected using a Ge detector and a SCA. The generator voltage is 400 mV, the step size is 25 kHz and the RF modulation is 50 kHz.

The RF system was first tested by observing the NMR resonance of the ^{54}Mn. The resonant frequency is already known for this system [35, 36, 37]. A plot of the resonance is shown in figure 7.59. The resonance is split into two subresonances because the applied field affects the two sublattices differently. The observed transitions here are from the $I^z = -3$ to $I^z = -2$ states.

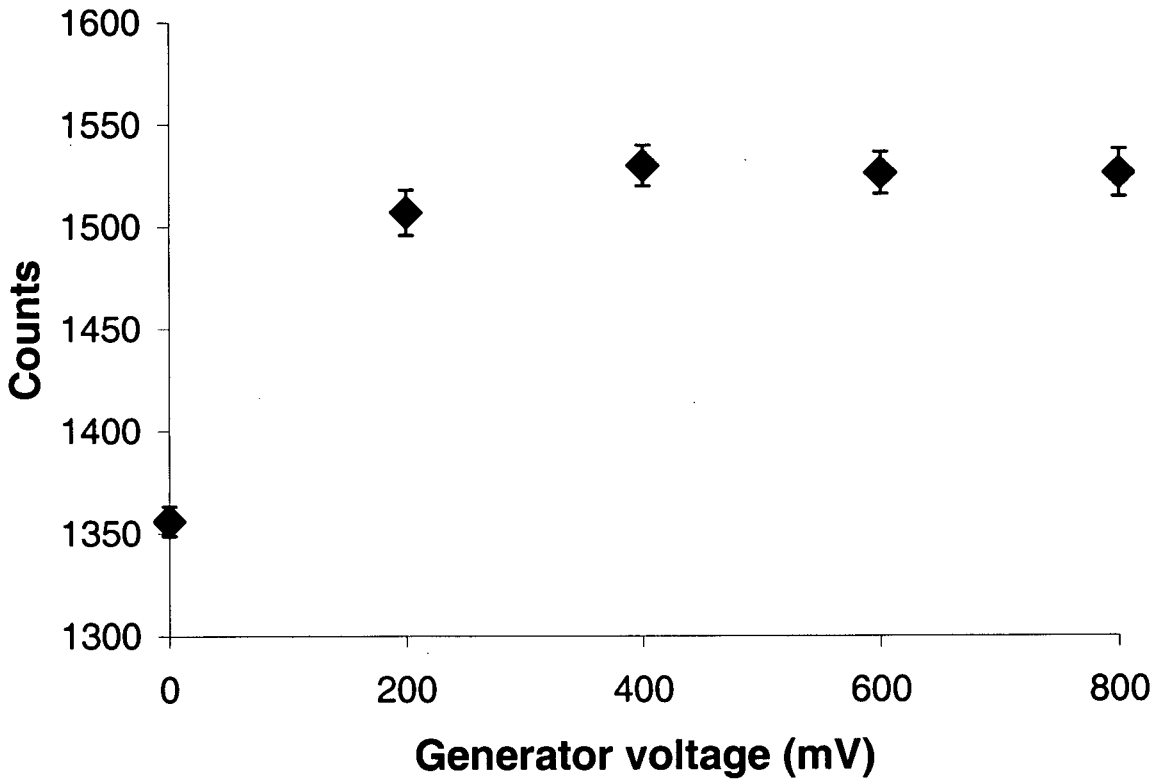

Figure 7.60: Determining the saturation point for the RF. The frequency was set to 499.7 MHz, the resonant frequency of one of the ^{54}Mn lines with a modulation of 50 kHz. The generator voltage was increased in 200 mV until the resonance was saturated. In subsequent frequency sweeps, 400 mV was used as the peak to peak generator voltage.

The optimum RF power to use without warming the fridge was then determined by increasing RF generator voltage while staying at the resonant frequency. Although the resonance appears to be nearly saturated at 200 mV, 400 mV was used for the subsequent sweeps to be certain that enough RF power was delivered to the sample at all frequencies. The anisotropy is plotted as a function of RF generator voltage in figure 7.60.

7.4.2 ^{57}Co and ^{60}Co NMR

Frequency sweeps to find the NMR resonances of ^{57}Co and ^{60}Co were performed based on the NO results of table 7.5. Since the NO results predict significantly different hyperfine fields for the two Co isotopes, it was expected that the result of an NMR resonance would resolve the issue completely.

In the case of ^{57}Co in crystal A, the frequency was swept from 120 to 240 MHz, in 25 kHz steps with a dwell time of 10 s and an RF modulation of $\pm$50 kHz. Based on the NMR of the ^{54}Mn, it was assumed that 10 s was sufficient to saturate the modulation. The spin-lattice relaxation time for ^{54}Mn in the crystal has been measured to be between 10^6 and 10^7 s at lattice temperatures below 65 mK [38]. Above 65 mK the dominant relaxation process is a Raman process while below 65 mK it is a direct process. Although the orbital contribution to the spin of ^{57}Co may make the spin-lattice relaxation shorter for the direct process, it seemed reasonable to assume that the spin-lattice relaxation time for Co satisfied $T_1^{Co} \gg 10^3$ s. A resonance should have been visible in the data, despite the short dwell time because 1000 s was sufficient to obtain approximately 6000 net counts in the MCA for the 136 keV γ-line of ^{57}Co, (statistical errors of approximately 1%). The frequency spectrum should then contain low temperature counts until the resonance frequency, and then higher counts relaxing very slowly to the low temperature counts in a time sufficiently slow to achieve good statistics. Unfortunately, no significant change in anisotropy was observed throughout the entire frequency spectrum.

Although the frequency generator used had a maximum modulation of ±100 kHz, a variety of different sweep patterns and modulations were attempted in an effort to find the NMR resonance. In particular, the frequencies 155 MHz to 205 MHz were split into 5 MHz blocks. The RF field was applied in 50 kHz steps at 100 kHz modulation with a 1 s dwell time. The entire 5 MHz block was covered every 100 s. The total dwell time for each block was 12100 s, which allowed significant statistics to be achieved for each frequency block. Resonances of a variety of widths (from 0 to more than 5 MHz) would be observable by this technique, even with relaxation times, T_1^{Co} as short as 1000 s. Careful analysis of the data, as explained in section 7.2, did not indicate the existence of a resonance because the γ-ray anisotropy did not change throughout the sweeps.

For the ^{60}Co NMR, it was possible to use the much higher efficiency NaI detectors, and it was possible to cover a greater frequency range. In this case, the frequency was swept through 1 MHz blocks, with 50 kHz steps, 5 s dwell time and a modulation of 100 kHz. Each MHz block was counted for 1000 s, giving more than 130000 counts, or a relative statistical error of approximately 0.3%. A resonance with T_1^{Co} as short as 1000 s and a width of several MHz would be visible with this technique. The total frequency range covered was 70 to 363 MHz. Again, a careful analysis of the data showed no resonance anywhere in the spectrum.

One explanation for not observing the NMR resonance is that some Co ions do not grow into the crystal lattice substitutionally. This seems quite possible because $MnCl_2 \cdot 4H_2O$ contains four water molecules while $CoCl_2 \cdot 6H_2O$ contains six. Consequently, the Co ions could be situated in a variety of interstitial lattice configurations and experience a wide range of different hyperfine fields. Resonances could also be sufficiently broadened as to be unobservable with our NMR techniques. It is also possible that $T_1^{Co} \ll 1000$ s, which would also make the resonance difficult to observe with our sweep technique. The NMR results on the spin-lattice relaxation of the ^{54}Mn show that

Co may have a short T_1, and this could also explain why the resonance was not observed.

7.4.3 NMR results on ^{54}Mn - the influence of Co impurities

The NMR data on ^{54}Mn was mainly collected on NaI detectors. The high efficiency of the detectors allowed for dwell times of 100 s. The data were fitted using a χ^2 minimization. The model is similar to that used in previous NMR studies of ^{54}Mn in $MnCl_2{\cdot}4H_2O$ [36]. The changes in level populations due to spin-lattice relaxation are governed by equation 2.44. The NMR resonance is assumed to be Gaussian in shape and inhomogeneously broadened. The RF field is assumed to be sufficiently strong to completely saturate the resonance.

If the NMR resonance involves the equalization of levels m and $m+1$ then, at a frequency ω with a modulation of $\pm\phi_0$, the change in population of the mth sublevel is given by

$$\Delta p_m = A_g \int_{-\phi_0}^{\phi_0} \exp\left(\frac{(\omega+\phi-\omega_0)^2}{\sigma^2}\right) d\phi \tag{7.167}$$

where A_g is the amplitude of the resonance. The levels must be completely equalized by integrating over the entire frequency range, therefore

$$A_g = \frac{p_{m+1} - p_m}{2\sigma\sqrt{\pi}} \tag{7.168}$$

If the system is at thermal equilibrium before the resonance, then $p_{m+1} = p_m \exp(-\Delta E/k_B T_L)$ where T_L is temperature of the lattice and ΔE is the difference in energy between the two levels and is therefore equal to the resonant frequency. However, the populations are not at equilibrium in a sweep through the pseudoquadrupole-split resonances when the sweep time is $\leq T_1$.

The change in level population are governed by $2I+1$ equations (one for each level), or $2I$ equations by using $\sum_m p_m = 1$. The change in anisotropy can be calculated using

equation 2.13, or

$$\frac{dW(\theta)}{dt} = \sum_m a_m(\theta)\frac{dp_m}{dt} \tag{7.169}$$

In the simplest case, the χ^2 fit then involves 4 parameters: σ, T_L, ω_0 and T_1 where σ is the width of the resonance, T_L is the temperature of the lattice, ω_0 is the centre frequency of the resonance and T_1 is the spin-lattice relaxation time. In reality, the data were collected using SCAs with baseline contamination from the higher energy ^{60}Co γ-rays. It was therefore difficult to determine the exact anisotropy, but only the change in counts due to the resonance. This means that the lattice temperature, T_L, which appears in the equation 2.44 cannot be determined precisely from the data. Therefore, T_L was assumed to be a constant and equal to 44.3 mK, the base temperature determined by NO data. The possible error in T_L can be estimated by the maximum change in base temperature anisotropy between the sweeps. This change is at most 1% and means that the $T_L = (44.3 \pm 2)$ mK for all the fits. Furthermore, test fits where T_L was included as a fit parameter did not significantly alter the values of the other parameters.

In order to analyse the data, two more parameters are introduced: K was is the number of counts measured in the given dwell time (typically 100 s) before resonance, and B which is the factor of proportionality between the change in counts, $dN(\theta)/dt$, and the change in anisotropy. B is given by

$$\begin{aligned}\frac{dN(\theta)}{dt} &= B\frac{dW(\theta)}{dt} \\ &= B\sum_m a_m(\theta)\frac{dp_m}{dt}\end{aligned} \tag{7.170}$$

The fits used five parameters in the simplest case: σ, ω_0, T_1, K and B.

An example of the data and fits can be seen in figures 7.61 and 7.62. The resonances do not have satellite lines, as might be expected from Mn ions with nearest neighbour impurities. However, the linewidth is much broader than the pure $MnCl_2{\cdot}4H_2O$ crystal. Kotlicki *et al.* report a HWHM of 35 kHz [36], which corresponds to $\sigma = 42$ kHz, while

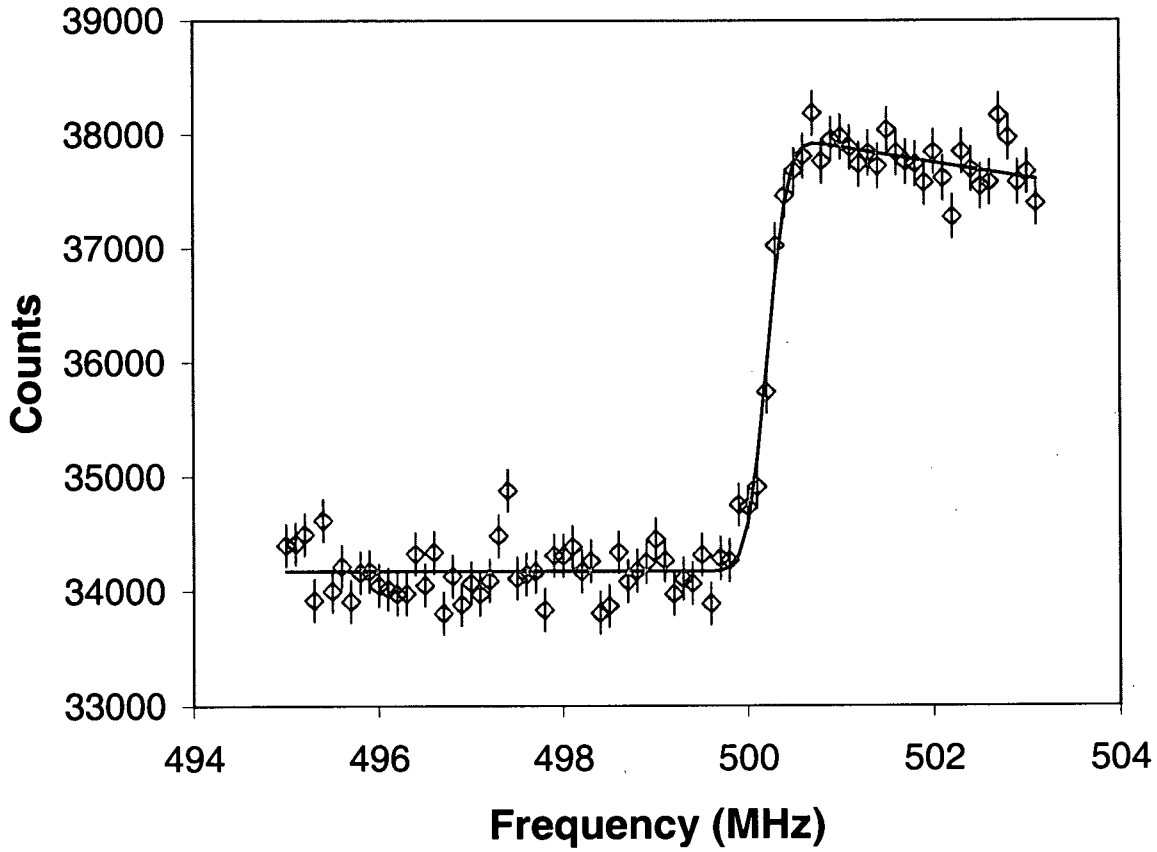

Figure 7.61: The number of counts at 0° as a function of frequency, showing the NMR resonance of ^{54}Mn in zero field. The frequency was swept upwards. The frequency step is +100 kHz, the modulation is ±100 kHz. The best fit parameters are $K = 34170 \pm 27$, $B = 257 \pm 7$, $\sigma = (254 \pm 32)$ kHz, $\omega_0 = (500.27 \pm 0.01)$ MHz and $T_1 = (176 \pm 68) \cdot 10^3$ s.

the crystal with impurities has a $\sigma > 200$ kHz. This increase in width is certainly due to the presence of impurities. The most accurate value of the spin lattice relaxation time, $T_1 = (253 \pm 18) \cdot 10^3$ s is obtained from figure 7.62 because it has the longest relaxation tail past the resonance.

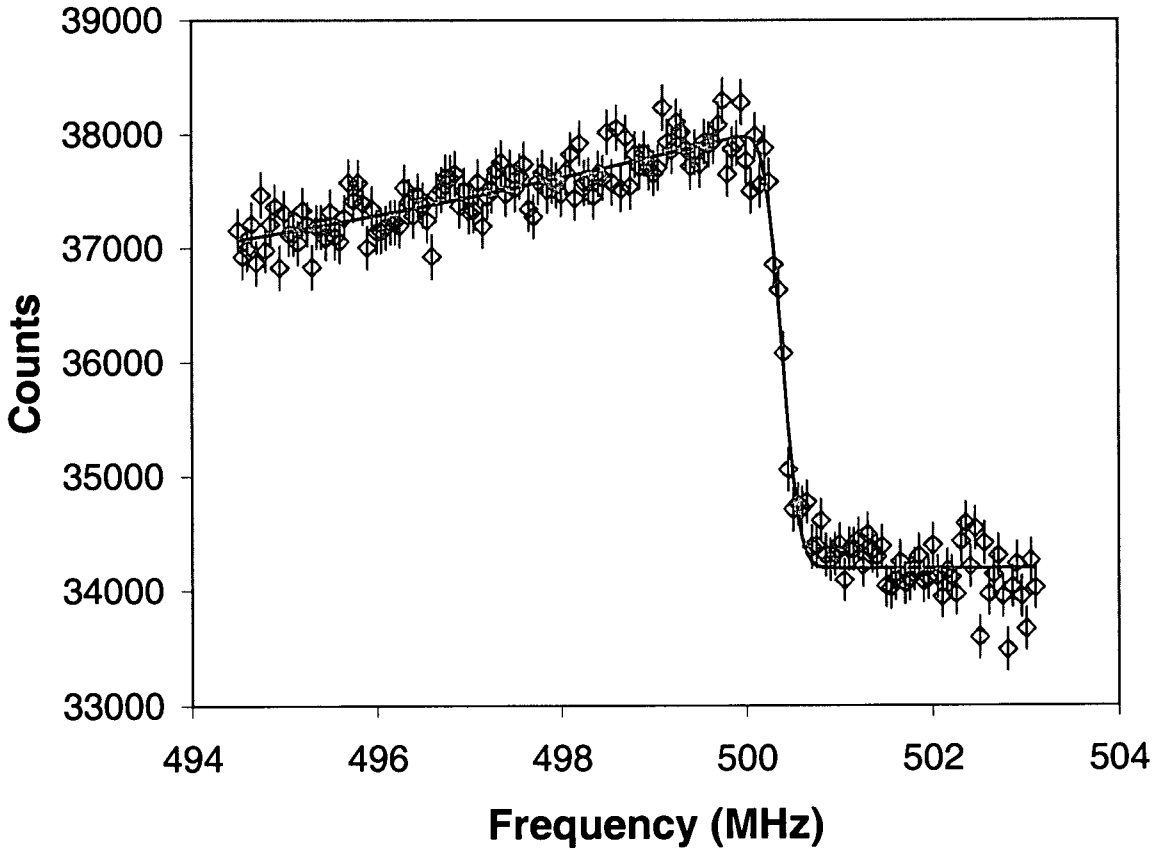

Figure 7.62: The number of counts at 0° as a function of frequency, showing the NMR resonance of ^{54}Mn in zero field. The frequency was swept downwards. The frequency step is -50 kHz, the modulation is ±50 kHz. The best fit parameters are $K = 34196 \pm 27$, $B = 260 \pm 4$, $\sigma = (205 \pm 21)$ kHz, $\omega_0 = (500.36 \pm 0.01)$ MHz and $T_1 = (253 \pm 18) \cdot 10^3$ s.

Upward and downward sweeps of the main resonance with smaller frequency steps can be seen in figures 7.63 and 7.64. The fit to the downward sweep (figure 7.64) appears reasonable, but the upward sweep (figure 7.63) is not fitted well at the start of the resonance. It seems clear that a simple Gaussian is not sufficient to fit the data.

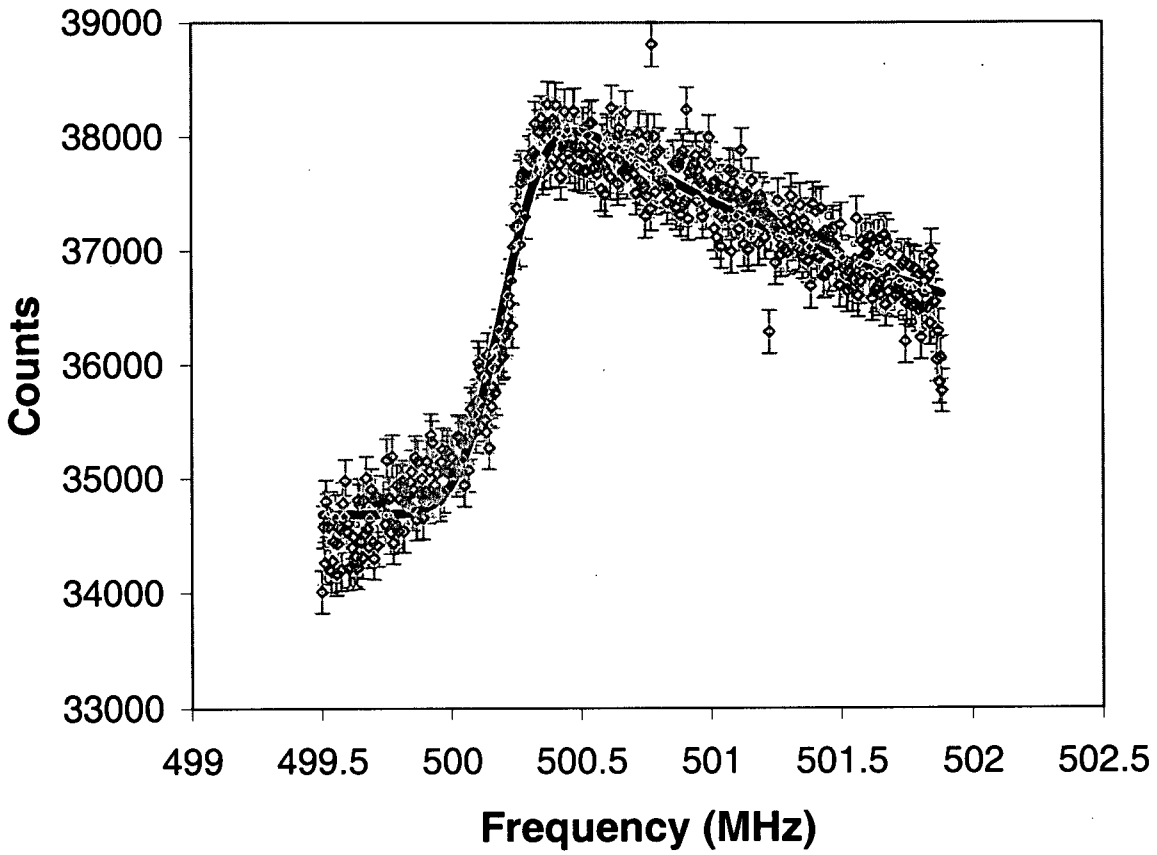

Figure 7.63: The number of counts at 0° as a function of frequency, showing the NMR resonance of ^{54}Mn in zero field. The frequency was swept upwards. The frequency step is +5 kHz, the modulation is ±5 kHz. The best fit parameters are $K = 34685 \pm 22$, $B = 266 \pm 3$, $\sigma = (196 \pm 8)$ kHz, $\omega_0 = (500.21 \pm 0.01)$ MHz and $T_1 = (288 \pm 9) \cdot 10^3$ s.

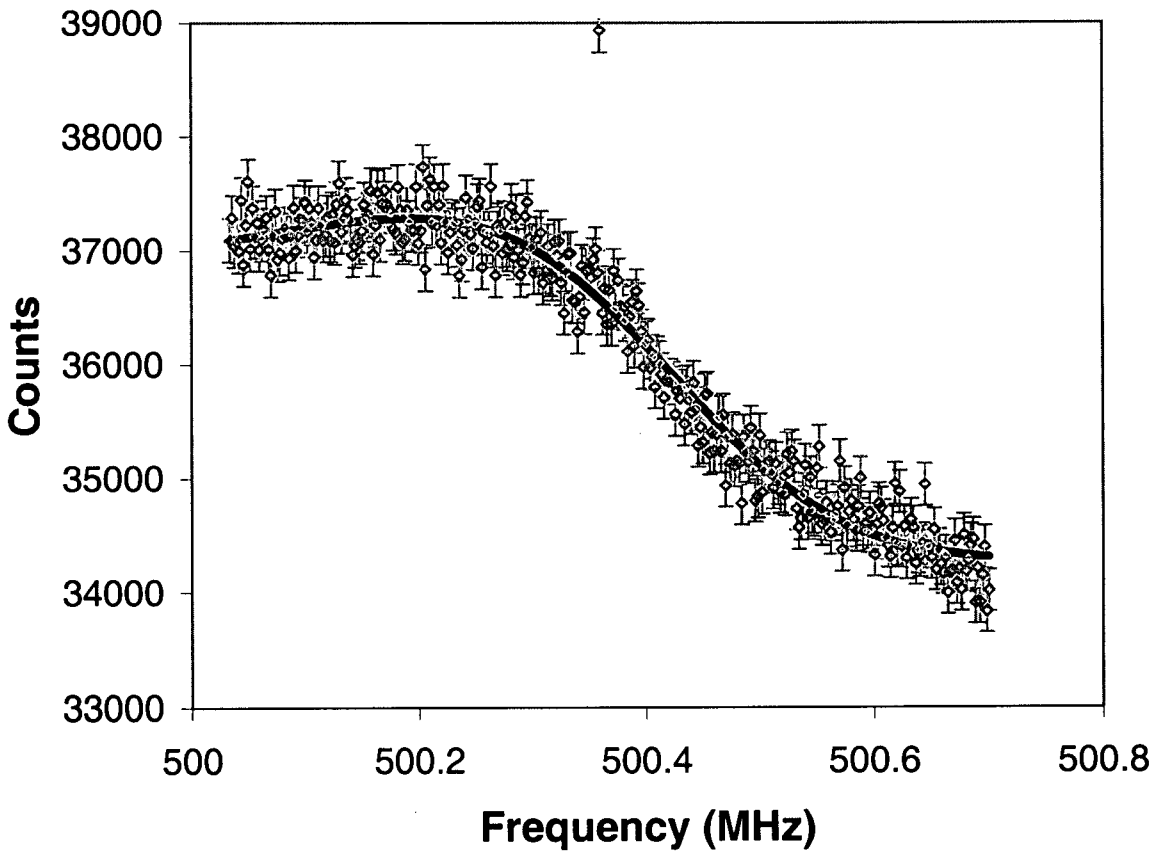

Figure 7.64: The number of counts at 0° as a function of frequency, showing the NMR resonance of ^{54}Mn in zero field. The frequency was swept downwards. The frequency step is -2 kHz, the modulation is ±5 kHz. The best fit parameters are $K = 34311 \pm 35$, $B = 241 \pm 15$, $\sigma = (168 \pm 10)$ kHz, $\omega_0 = (500.42 \pm 0.01)$ MHz and $T_1 = (488 \pm 146) \cdot 10^3$ s.

In order to fit the data more accurately, a more elaborate model was introduced. The assumption is that a fraction, r, of the Mn ions are sitting in sites perturbed by neighbouring Co impurities. These perturbed sites have a different resonant frequency and line width than the unperturbed sites. The relaxation time for the two sites was assumed to be the same.

This model introduces too many free parameters into the fit. Therefore the upward and downward sweeps (in figures 7.63 and 7.64) were fitted simultaneously and T_1 was fixed at the value of $253 \cdot 10^3$ s found from the fit to the data in figure 7.62.

It was observed that the resonance appeared to be in a different position for the upward and downward sweeps. This could result from the frequency modulation being larger than indicated by the RF generator and a modulation parameter ϕ_0 was introduced to take this effect into account. A subsequent measurement with a spectrum analyser at $\nu \sim 500$ MHz showed that the true center frequency is not the expected frequency to the precision indicated on the front panel of the generator. Furthermore, when the indicated modulation was less than 20 kHz, the spectrum had an approximately Gaussian shape with a FWHM of 20 kHz. It is therefore possible that the resonance was being excited at frequencies as much as 20 kHz from the centre frequency. However, the modulation parameter from the fits was found to be 84 ± 2 kHz, ie. four times greater. The statistical error on the resonant frequencies found from the fits are only approximately 10 kHz, but this discrepancy between upward and downward sweeps can be explained by a systematic error of ± 100 kHz in the long term frequency stability of the RF generator.

In the final analysis there were 9 free parameters used to fit the data: K_1 and K_2, the counts prior to resonance for the upward and downward sweeps respectively; σ_1 and σ_2, the linewidths of the main and secondary resonances respectively; ω_1 and ω_2, the centre frequencies of the main and secondary resonances respectively; B, as described by equation 7.170; r, the ratio of spins in perturbed sites; and ϕ_0, the modulation parameter

or frequency shift between the upward and downward sweeps.

The results of the fit can be seen in figures 7.65 and 7.66. There is definitely improvement to the fit in the initial rise of the upward swept resonance (figure 7.65). The ratio of perturbed spins is $r = 0.14 \pm 0.04$ and is consistent with the expected value of approximately 0.25 calculated for substitutional impurities with only nearest neighbour effects. This value of r is also consistent with a variety of interstitial lattice positions. Note that the effects of an impurity is to decrease the resonant frequency.

The model, however, is not entirely satisfactory. In particular, the width of the main resonance, $\sigma_1 = (155 \pm 7)$ kHz, is still much larger than the width of 42 kHz previously measured for a crystal with no impurities [36]. The assumption that an impurity affects only the spins in its immediate vicinity is not valid, and the effects must be of longer range.

The model is still useful because it shows that the resonance is not Gaussian in shape, nor even symmetric about the centre frequency. Thus the effect of the impurities is to shift the resonant frequency of the ^{54}Mn downward, although the magnitude of this shift is relatively small.

The NMR resonance in an applied field of 0.5 T can be seen in figure 7.67. The line is split into two subresonances corresponding to the spins from each of the two sublattices. The fit parameters were then K, B, σ_1, ω_1, σ_2, ω_2, T_{11} and T_{12} where the index 1 and 2 refer to the lower frequency and higher frequency lines respectively. In this case, a more complicated model using nearest neighbour effects was not attempted because it introduces too many parameters, and T_1 is not known and cannot be fixed. The fit is not entirely satisfactory, particularly in the final relaxation to the base counts. This is likely due to the assumption of Gaussian lineshape, and the fact that the modulation is larger than indicated by the generator. A larger modulation has the effect of preventing the spins from relaxing as early and the fit then overestimates the value of T_1. It is clear

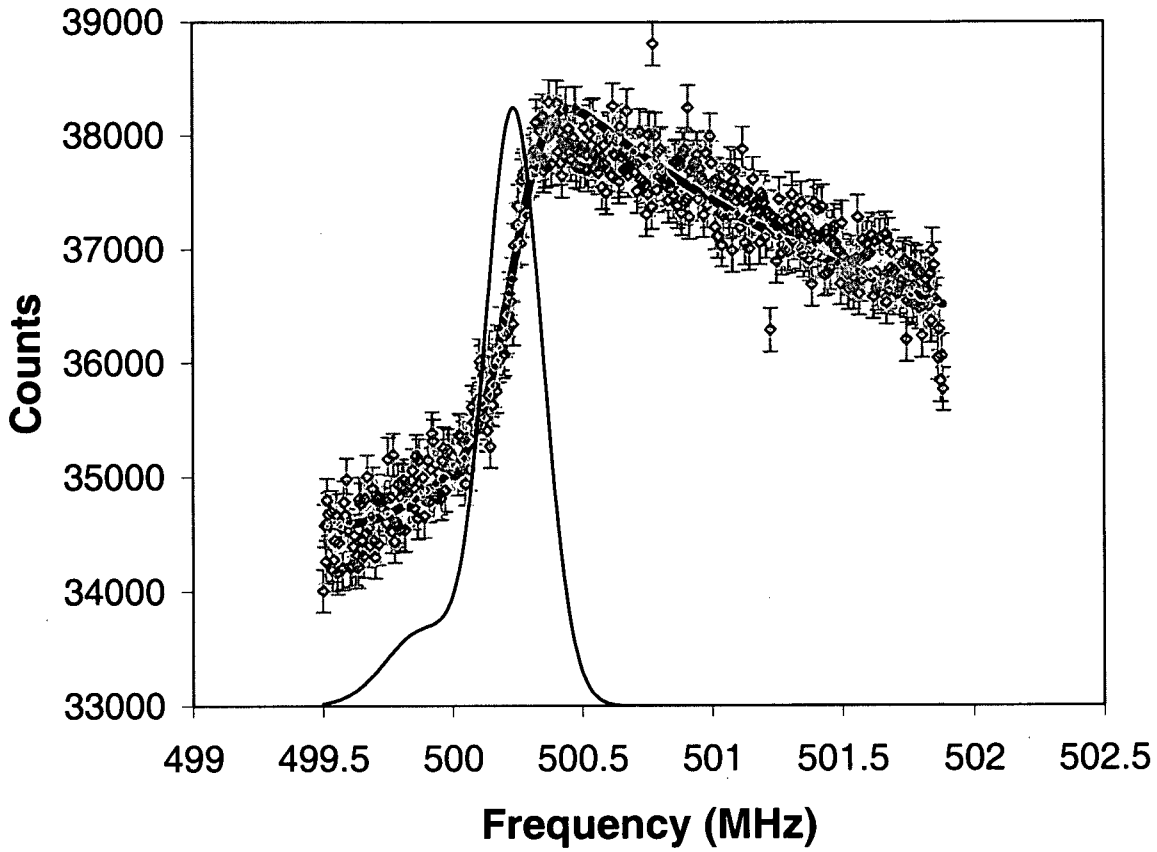

Figure 7.65: The number of counts at 0° as a function of frequency, showing the NMR resonance of ^{54}Mn in zero field. The frequency was swept upwards. The frequency step is +5 kHz and the modulation is ±5 kHz. The best fit parameters are $K_1 = 34577 \pm 31$, $K_2 = 34432 \pm 31$, $B = 287 \pm 4$, $\sigma_1 = (155 \pm 7)$ kHz, $\omega_1 = (500.32 \pm 0.01)$ MHz, $\sigma_2 = (205 \pm 58)$ kHz and $\omega_2 = (499.97 \pm 0.06)$ MHz, $r = 0.14 \pm 0.04$ and $\phi_0 = 84 \pm 2$ kHz. The thick line is the best fit. The thin line is the shape of the double Gaussian NMR resonance in arbitrary units.

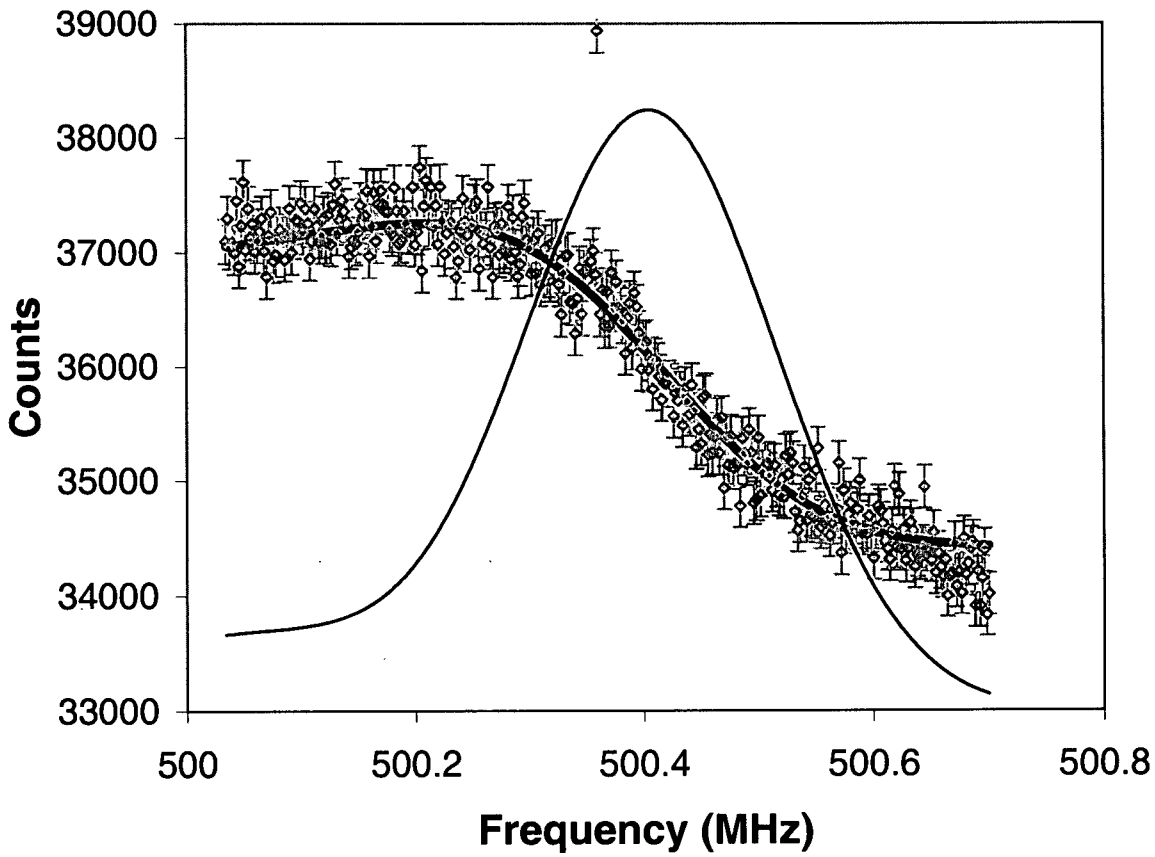

Figure 7.66: The number of counts at 0° as a function of frequency, showing the NMR resonance of ^{54}Mn in zero field. The frequency was swept downwards. The frequency step is -2 kHz and the modulation is ±5 kHz. The best fit parameters are the same as in figure 7.65 because both curves were fit simultaneously with the same parameters. The thick line is the best fit to the data. The thin line is the shape of the double Gaussian NMR resonance in arbitrary units.

though that the relaxation time for the higher frequency line, T_{12} is significantly shorter than for the lower frequency line. The sublattice corresponding to the high frequency line is more strongly coupled to the electronic magnons with the lower energy gap. This can be seen by considering the orientation of electronic and nuclear magnetic moments of the two sublattices relative to the applied field.

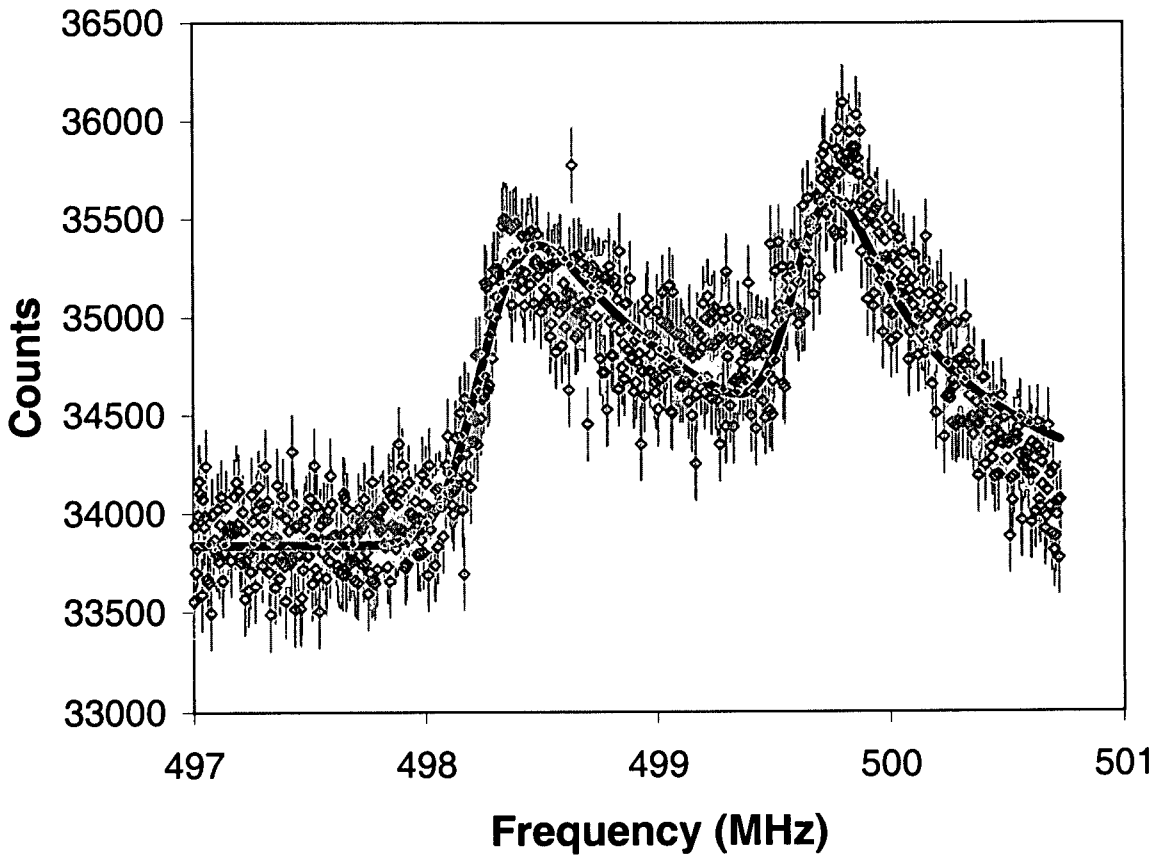

Figure 7.67: The number of counts at 0° as a function of frequency, showing the NMR resonance of ^{54}Mn in an applied field of 0.5 T. The frequency was swept upwards. The frequency step is +5 kHz and the modulation is ±5kHz. The The best fit parameters are $K = 33838 \pm 14$, $B = 288 \pm 13$, $\sigma_1 = (216 \pm 22)$ kHz, $\omega_1 = (498.25 \pm 0.01)$ MHz, $\sigma_2 = (176 \pm 13)$ kHz and $\omega_2 = (499.62 \pm 0.01)$ MHz.

An upward frequency sweep where all six transitions ($I^z \rightarrow I^z + 1$) are observed is shown in figure 7.68. The fit was based on a model with six Gaussian transitions, of

equal width σ, centered at positions $\omega_0 + MI^z$ where I^z goes from -3 to +2. There were 6 free parameters for the fit: K, B, σ, ω_0, T_1 and M. The result of the fit is excellent.

The zero field Hamiltonian for an electronic and nuclear spin in the crystal is

$$H = g\mu_B B_E S^z + D[(S^z)^2 - \frac{1}{3}S(S+1)] + A\vec{I}\cdot\vec{S} + P[(I^z)^2 - \frac{1}{3}I(I+1)] \qquad (7.171)$$

where B_E is the exchange field, D is the crystalline field anisotropy interaction strength, and P is the quadrupole interaction strength.

The energy difference between two sublevels $I^z = m$ and $I^z = m+1$ is given by [36]

$$\Delta E_{m,m+1} = -AS + P'm + P(2m+1) \qquad (7.172)$$

where $P' = \frac{A^2 S}{g\mu_B B_E - 4D}$ is the pseudoquadrupole interaction strength.

The quadrupole and pseudoquadrupolar splitting, $M = P' + 2P$ is found to be (3.130± 0.011) MHz. This agrees well with the value for a pure crystal of 3.1 MHz [36]. The value of $\omega_0 = -AS + P$ is found to be (509.68 ± 0.03) MHz, in agreement with the result for a pure crystal of 509.72 ± 0.25 MHz [36].

It is interesting that the value of the spin-lattice relaxation time measured is $T_1 = (83 \pm 4) \cdot 10^3$ s. This is significantly shorter than the value of $(253 \pm 18) \cdot 10^3$ s found in figure 7.62 where the majority of the fit involves the relaxation of the spins after a single resonance. Although the value of $K = 33794 \pm 19$ indicates that the crystal may be as much as 2 mK colder in this case, that should make the value of T_1 longer. It is unclear to what this discrepancy may be due, but the value of $T_1 = (253 \pm 18) \cdot 10^3$ s is certainly more accurate because the fit involves fewer free parameters, and the majority of the data only involves spin-lattice relaxation after a single resonance.

It is also interesting to compare the value of T_1 measured with the Co impurities to the value measured in the pure crystal [38]. In the pure crystal, the dominant relaxation process below 65 mK is found to be a direct process, with values of $T_1 \sim 3 \cdot 10^6$ s. The

presence of 3.96 % Co impurities reduces the value of T_1 by an order of magnitude at 44.3 mK! Presumably the magnon spectrum is affected by the impurities and this effect is worthy of future theoretical study.

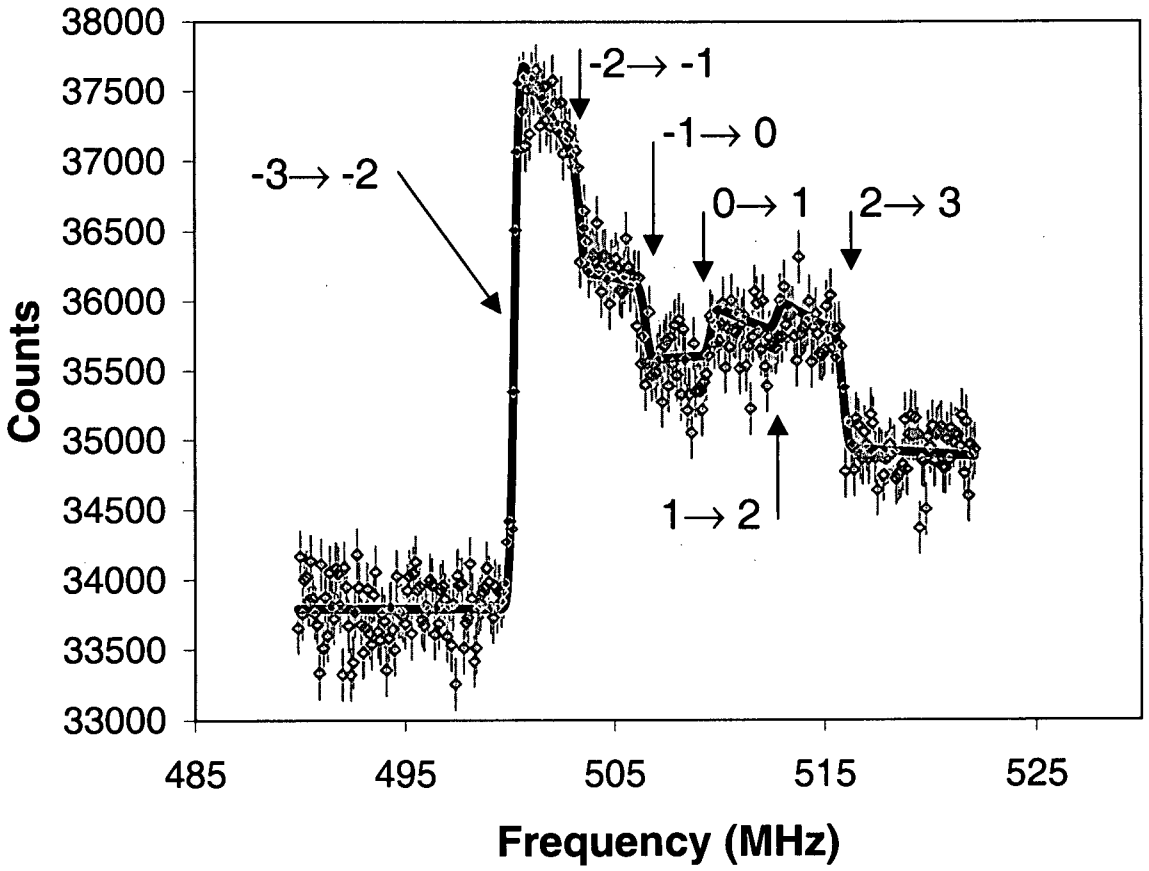

Figure 7.68: The number of counts at 0° as a function of frequency, showing all six transitions between magnetic substates in zero field. The frequency was swept upwards. The frequency step is +100 kHz and the modulation is ±100 kHz. The best fit parameters are $K = 33794 \pm 19$, $B = 264 \pm 4$, $\sigma = (269 \pm 30)$ kHz, $\omega_0 = (509.68 \pm 0.03)$ MHz, $T_1 = (83 \pm 4) \cdot 10^3$ s and $M = (3.130 \pm 0.011)$ MHz.

The changes is populations of the magnetic sublevels throughout the resonances is shown in figure 7.69. These are calculated from the data in figure 7.68. Each resonance equalizes the two levels which subsequently relax due to T_1 processes. In figure 7.70, the level populations are plotted as they would be if no T_1 processes were present.

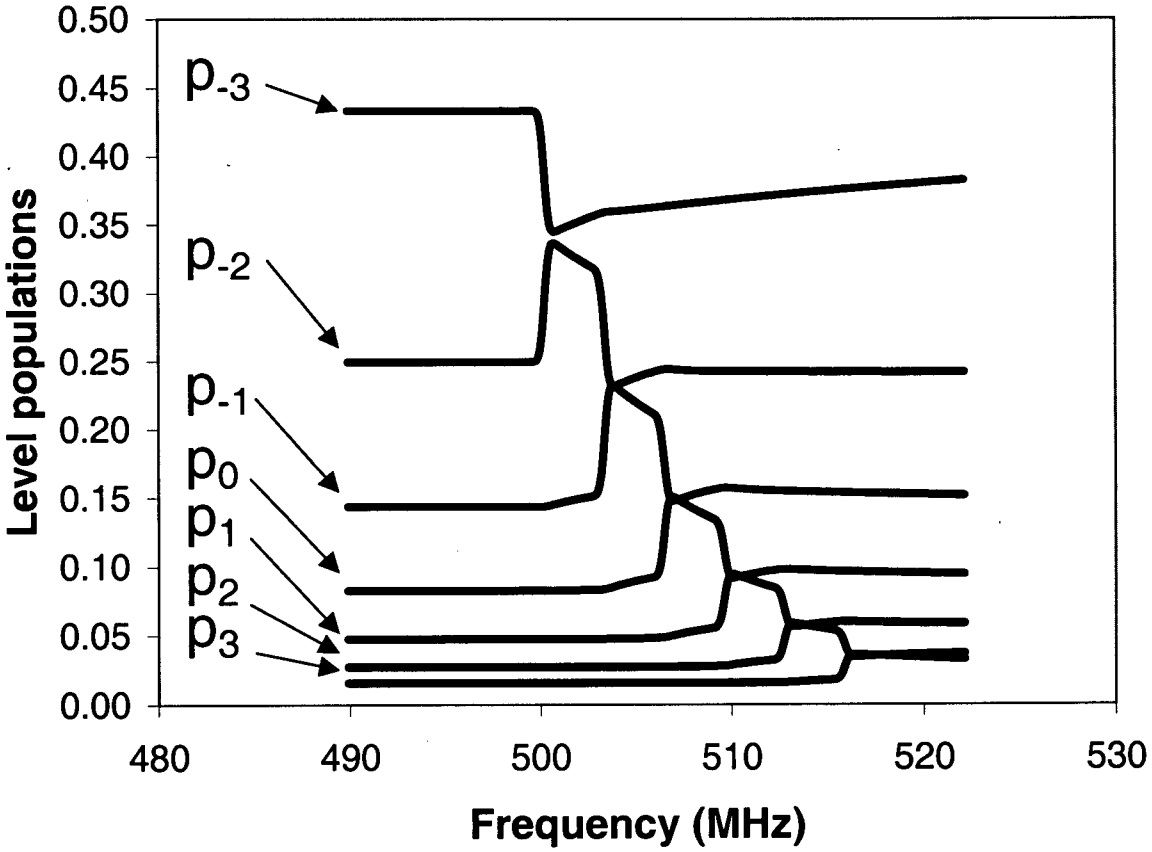

Figure 7.69: The change in level populations throughout the frequency sweep shown in figure 7.68

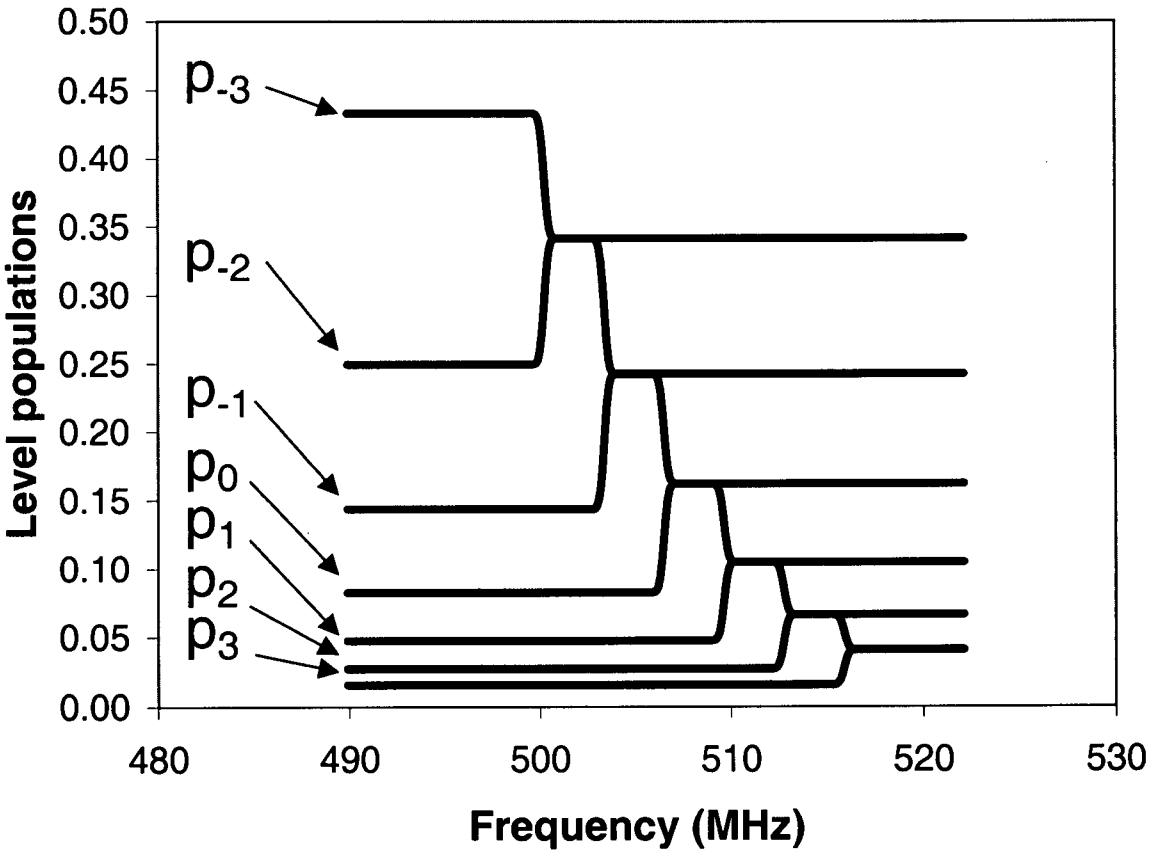

Figure 7.70: The change in level populations throughout the frequency sweep shown in figure 7.68 as they would be if no relaxation effects were present, i.e. if $T_1 = \infty$.

7.5 Conclusions

The NO results on ^{60}Co and ^{57}Co predict quite different hyperfine fields for the two isotopes. In Crystal A, the hyperfine field is 15.5 ± 2 for ^{57}Co. In crystal B, the hyperfine field is 29.1 ± 0.5 T for ^{60}Co. In crystal C, the hyperfine fields are 15.6 ± 2.7 T and 25.6 ± 0.4 T for ^{57}Co and ^{60}Co respectively. This discrepancy is extremely surprising, and we do not presently have a reasonable explanation for it. An NMR resonance, which would allow us to measure the hyperfine field very precisely was not found. This indicates that the relaxation times are much less than 1000 s, or that the resonances are more than 10 MHz in width. It seems likely that many Co ions do not sit at Mn substitutional lattice positions.

The NMR results on ^{54}Mn also indicate that the Co impurities do not enter the lattice substitutionally. If substitutional replacement occurred, we would expect to see an NMR resonance with a narrow main line due to Mn ions with no nearest neighbour impurities and a HWHM on the order of 35 kHz [36], and a satellite line of approximately 1/4 the intensity due to Mn with one nearest neighbour impurity. Instead we see a possible two line structure, but with linewidths on the order of 150 kHz. The ratio of intensities of the two lines is 1/6. Although this could be due to substitutional replacements with long range effects on the neighbouring ions, it is more likely that the replacements are not substitutional and cause important imperfections in the lattice which have long range effects.

We suspect that the different hydration of $MnCl_2 \cdot 4H_2O$ and $CoCl_2 \cdot 6H_2O$ makes substitutional replacements difficult during growth. This might indicate that the ^{54}Mn grown into $CoCl_2 \cdot 6H_2O$ as described in Chapter 6 is not substitutional. It would be unreasonable to expect that the implanted ^{56}Mn would then be substitutional. The site occupancy factor of $f = 0.53 \pm 0.10$ might indicate that several interstitial sites are

possible and some are favoured during growth, others during implantation.

The position of the resonant frequency and the pseudoquadrupole interaction for ^{54}Mn are not measurably affected by the presence of the impurities. The width of the resonance is increased significantly, and the shape is not Gaussian. The presence of the $(3.96 \pm 0.04)\%$ impurities reduces the spin-lattice relaxation time, T_1, by an order of magnitude. This reduction in T_1 can be explained if the impurities serve as scattering centers for magnons. These scatterers would reduce the magnon lifetime and broaden their spectrum. Direct processes would be greatly enhanced by a broadening of the magnon spectrum, and since we expect these to be the principle spin-lattice relaxation mechanisms at $T < 65$ mK [38], T_1 would be reduced. Interestingly, this explanation also provides some insight into our inability to find the NMR resonance for the Co isotopes. If the impurities scatter electronic magnons appreciably, these scattering processes will provide important spin-lattice relaxation mechanisms. The spin-lattice relaxation time could be much less than 1000 s, making the resonance undetectable with our search techniques. It would be necessary to use a generator with a much larger modulation (± 5 MHz would be sufficient) in order to observe the resonance.

The results of this experiment have led us to try doping ^{54}Mn into $FeCl_2 \cdot 4H_2O$. Since this crystal has the same hydration as $MnCl_2 \cdot 4H_2O$ it is hoped that substitutional replacement will occur. A 7% anisotropy has been observed, but the NMR resonance has not yet been found. This work is currently in progress.

Chapter 8

Summary and conclusions

Nuclear Orientation and its related NMR techniques can be used to study the properties of interesting magnetic systems. The NO gives information on the electronic environment of the nucleus which provides the hyperfine field. NMR can be used to measure the hyperfine field more accurately, to study quadrupole and pseudoquadrupole splittings and to probe collective nuclear excitations. The spin-lattice relaxation can also be measured in order to elucidate the coupling of the nuclear spin system to the lattice. In the magnetic insulators studied in this thesis, the pseudoquadrupole interactions, the spin-lattice relaxation and the collective nuclear interactions can be used to study the electronic magnon spectrum. When combined with an isotope implantation facility, the isotopes which can be used as suitable probes is vastly increased because it is feasible to perform experiments with shorter lived isotopes online or pseudo-online.

The collective nuclear excitations, which lead to a "frequency pulling" effect were studied in MnAc using NMR-TDNO. Feedback stabilization of the RF power is necessary for this type of experiment and a new, improved, feedback system was analysed and utilized. The MnAc system is quasi-2-dimensional, with strong anisotropy fields. It therefore provides a convenient system for studying 2-dimensional Heisenberg systems with anisotropy, and both the electronic and nuclear excitations, or spin waves, can be studied. The theory of nuclear collective excitations had previously only considered systems with $I = 1/2$ where pseudoquadrupole interactions are non-existent. This theory has been extended here to include the pseudoquadrupole interaction and non-uniaxial

anisotropy fields. The agreement between theory and experiment is good, with discrepancies being likely due to simplifying assumptions when calculating the electronic spin wave spectrum. The system is complicated by the elaborate crystal structure where lattice sites are occupied by triplets of ions, in two inequivalent sites, Mn1 and Mn2.

Future work in this area should test the theory in a system with $I > 1/2$, highly anisotropic crystalline fields, but a simpler crystal structure with a single ion per lattice site. This system could be either two or three dimensional, but would allow the predictions of the theory to be tested without the complications of complex electronic magnon excitations.

The first NO experiments with implanted isotopes into insulators were performed at Louvain-La-Neuve, using $MnCl_2 \cdot 4H_2O$ and $CoCl_2 \cdot 6H_2O$ as hosts. These targets were doped with ^{54}Mn during growth. It was found that when ^{56}Mn was implanted into $MnCl_2 \cdot 4H_2O$ the implantation fraction was consistent with unity, but in $CoCl_2 \cdot 6H_2O$ it was not. In future experiments, NMR should be performed on these sytems to determine the precise hyperfine fields. This would clarify which sites were occupied by the implanted isotopes. Once the lattice positions of implanted isotopes can be determined, a variety of condensed matter physics, experiments could be performed. In some cases, the hyperfine fields in an insulator can be larger than in an Fe host, and nuclear physics experiments could also be performed in insulators.

The studies of Co impurities in $MnCl_2 \cdot 4H_2O$ showed that the hyperfine fields for ^{57}Co and ^{60}Co are significantly different although, in one experiment, both were grown into the same crystal. The reason for this discrepancy cannot be explained simply, and should be explored further. An NMR resonance for the Co was not observed, and this is likely due to a short spin-lattice and/or a large linewidth both of which makes the observation of a resonance difficult.

The NMR of ^{54}Mn was measured in a crystal with $\sim 4\%$ Co in order to determine the

effects of impurities. The line was found to be broadened and non-Gaussian in shape. The spin-lattice relaxation time was found to be an order of magnitude shorter than in the pure crystal. At the temperatures utilized in the experiment, the nuclear spin-lattice relaxation proceeds via a direct process. A possible reason for the reduction in T_1 is that the impurities act as scattering centres for the electronic magnons thereby broadening the magnon spectrum and enhancing this direct process. This indicates that the impurities act as scattering centres for electronic magnons and that spin-lattice relaxation time of the impurities is short, thereby making the observation of an NMR resonance for the impurities difficult. Finally, it seems likely that the impurities grow into interstitial lattice positions.

Further experiments should include a study of a system with the same hydration as the impurity. This is currently underway with a study of ^{54}Mn in $FeCl_2 \cdot 4H_2O$. Although 7% anisotropy has been observed, the NMR resonance has not yet been observed. It would also be of interest to study the effects of stable Fe in $MnCl_2 \cdot 4H_2O$ and to compare to the effects of the Co. Furthermore, several measurements with different amounts of impurities should be performed to determine the spin-lattice relaxation time as a function of impurity concentration. If the spin-lattice relaxation time could be controlled by including impurities during growth, some systems with long T_1 could be studied more easily. Finally, if the impurity concentration were high enough, it should be possible to make X-ray diffraction measurements to find the positions of the impurities in the lattice.

Bibliography

[1] A. Kotlicki and B. Turrell, Phys. Rev. Lett. **56**, 773 (1986).

[2] P. De Gennes, P. Pincus, F. Hartmann-Boutron, and J. Winter, Phys. Rev. **129**, 1105 (1963).

[3] E. Turov and M. Petrov, *Nuclear Magnetic Resonance in ferro and antiferromagnets* (John Wiley & Sons, New York, 1972), see chap. 2.

[4] P. Pincus, Phys. Rev. **131**, 1530 (1963).

[5] See e.g. K.S. Krane in *Low Temperature Nuclear Orientation*, ed. N.J. Stone and H. Postma (North Holland 1986) Ch. 2.

[6] See e.g. R. B. Firestone, *Table of Isotopes*, 8th Edition, ed. V.S. Shirley (John Wiley 1996).

[7] C. Cohen-Tannoudji, B. Diu, and F. Laloë, *Quantum Mechanics* (John Wiley & Sons, New York, 1977), see page 1340.

[8] R. Kubo and K. Tomita, J. Phys. Soc. Japan **9**, 888 (1954).

[9] T. Moriya, Prog. Theor. Phys. **16**, 23 (1956).

[10] F. Grover, *Inductance Calculations* (Dover publications, New York, 1973).

[11] See, e.g.: D. Landau and M. Krech, J. Phys.: Condens. Matter **11**, R179 (1999); T. Nagao and J. Igarashi, J. Phys. Soc. Japan **67**, 1029 (1998).

[12] See, e.g.: G. Seewald, E. Hagn, and E. Zech, Phys. Rev. Lett. **79**, 2550 (1997); G. Seewald, E. Hagn, and E. Zech, Phys. Rev. Lett. **78**, 5002 (1997); W.D. Hutchinson, M.J. Prandolini, S.J. Harker, D.H. Chaplin, G.J. Bowden and B. Bleaney, Hyp. Interact. **20/21**, 215 (1999).

[13] H. Suhl, Phys. Rev. **109**, 606 (1958).

[14] T. Nakamura, Prog. Theor. Phys. **20**, 542 (1958).

[15] M. Le Gros, A. Kotlicki, and B. G. Turrell, Hyp. Interact. **108**, 443 (1997).

[16] P. Burlet, Solid State Commun. **14**, 665 (1974).

[17] P. Beauvillain and J. Renard, Physica **86-88B**, 667 (1977).

[18] Y. Okuda, M. Matsuura, and T. Haseda, J. Phys. Soc. Japan **44**, 371 (1978).

[19] R. Flippen and S. Friedberg, Phys. Rev. **121**, 1591 (1961).

[20] J. Cowen, G. Johnston, and H. V. Till, J. Chem. Phys. **45**, 644 (1966).

[21] H. Abe and H. Morigaki, Proc. 1st Int. Conf. on Paramagnetic Resonance, Jerusalem 567 (1963).

[22] V. Schmidt and S. Friedberg, Phys. Rev. **188**, 809 (1969).

[23] A. Abragam and M. Pryce, Proc. Roy. Soc. **A205**, 135 (1951).

[24] P. Groth, *Chemische Krystallographie* (W. Engelmann, Leipzeg, 1910), Vol. 3, p. 69.

[25] J.-P. Blaizot and G. Ripka, *Quantum theory of finite systems* (MIT Press, Cambridge, Massachusetts, 1986), see chap. 3.

[26] N. Ashcroft and N. Mermin, *Solid State Physics* (Saunders College Pulishing, New York, 1976), see chap. 33.

[27] M. Fisher, Repts. Prog. Phys. **30**, 615 (1967).

[28] S. Vonsovskii, *Ferromagnetic Resonance* (Israel Program for Scientific Translations, Jerusalem, 1964), see chap. 3.

[29] J. V. Vleck, Phys. Rev. **74**, 1168 (1948).

[30] See e.g. A. Perez, G. Marest, B.D. Sawicka, J.A. Sawicki and T. Tyliszczak, Phys. Rev. **B28** (1983) 1227; L. Niesen, Hyperfine Interactions **13** (1983) 65; G. Langouche, Hyperfine Interactions 84 (1994) 279.

[31] See e.g. J.C. Soares, Nucl. Instr. Meth. Phys. Res. **B64** (1992) 215.

[32] Y. Kawase, S. Uehara, and S. Nasu, Nucl. Instr. Meth. Phys. Res. **B64**, 329 (1994).

[33] A. Zalkin, J. Forrester, and D. Templeton, Inorganic Chemistry **3**, 529 (1964).

[34] R. Altman, S. Spooner, D. Landau, and J. Rives, Phys. Rev. B **11**, 458 (1975).

[35] A. Kotlicki and B. Turrell, Hyperfine Interactions **11**, 197 (1981).

[36] A. Kotlicki, B. McLeod, M. Shott, and B. Turrell, Phys. Rev. B **29**, 26 (1984).

[37] A. Allsop, M. de Aráujo, G. Bowden, R. Clark, and N. Stone, J. Phys. C: Solid State Phys. **17**, 915 (1984).

[38] M. Le Gros, A. Kotlicki, and B. G. Turrell, Hyp. Interact. **77**, 203 (1993).

[39] J. Mizuno and K. Ukei, J. Phys. Soc. Japan **14**, 383 (1959).

[40] J. McElearney, J. Forstat, and P. Bailey, Physical Review **181**, 887 (1969).

[41] B. Turrell, P. Johnston, and N. Stone, J. Phys. **C5**, L197 (1972).

[42] D. Vandeplassche, L. Vanneste, H. Pattyn, J. Geenen, C. Nuytten, and E. van Walle, Nucl. Instr. Meth. **186**, 211 (1981).

[43] O. Lounasmaa, *Experimental Principles and Methods Below 1K* (Academic Press, London, 1974).

[44] I. Lowe and D. Whitson, Phys. Rev. **B6**, 3262 (1972).

[45] B. Will, P. Herzog, R. Paulsen, J. Camps, P. D. Moor, P. Schuurmans, N. Severijns, A. V. Geert, L. Vanneste, I. Berkes, M. D. Jesus, M. Lindroos, and P. V. Duppen, Phys. Rev. B **57**, 11527 (1998).